Doctoral Dissertation

# Studies on Single-Molecule Analysis and Visualization of Biological Phenomena Using Fluorescence Probes

Sooyeon Kim

January 2015

Graduate School of Engineering,
Osaka University

# Preface

The studies presented in this thesis were carried out under the direction of Professor Tetsuro Majima, the Institute of Scientific and Industrial Research (SANKEN), Osaka University during April 2010 to March 2015.

The object of this thesis is fluorescence detection methods to monitor biological phenomena occurring ex vivo and in a living cell. The aim of this research is to improve current understanding of biomolecules and intracellular metabolism by using single-molecule fluorescence spectroscopy or developing effective fluorescence probes. The author hopes that the results and conclusion presented in this thesis contributes to the further improvement of the current time and space limit of fluorescence detection of living matters, which will deepen our understanding of the life.

Sooyeon Kim

Department of Applied Chemistry
Graduate School of Engineering
Osaka University
2015

# Contents

# General Introduction

The smallest unit of the life is generally defined as a cell if one defines living matter should produce energy by itself. In a single cell, numerous biomolecules are densely populated and encapsulated by the plasma membrane. Furthermore, most biomolecules are biopolymer composed of various organic building blocks. Interestingly, essentially all kinds of metabolism to generate energy and remove waste, and pathological pathways that finally bring about a whole stop of metabolism of human beings are all caused by a single chemical reaction. Thus, the author believes in-depth understanding of biological phenomena starts from understanding a single intermolecular reaction inside of a cell.

Concerning that the interiors of the cell and human body are highly heterogeneous, spatial resolution of the detection emerges as a critical issue in order to investigate biological events at the molecular level. In this sense, fluorescence detection is an effective method since aduqately designed fluororescence probes are emissive in visible to near-IR regions where native biomolecules exhibit negligible photon absorption and emission. Because fluorescence is one way of radiative relaxations of the electronically excited molecule,[1] in principal, its temporal and spatial detection limits depend on its lifetime and light diffraction, respectively. For common fluorescence dyes, fluorescence lifetime ($\tau_{fl}$) is approximately a few ns, while the spatial resolution is 200−400 nm according to a diffraction limit described as ($\lambda_{ex}/2n\sin\theta$) where $\lambda_{ex}$ and $n\sin\theta$ are the excitation wavelength (nm) and numerical aperture (NA), which is in a range of 1.4−1.6 in modern optics, respectively.[2]

In practice, however, achieving both high resolutions of time (~ns) and space (sub-μm) is extremely challenging, similar to the basics of camera. In general, long exposure time enables to obtain the details of a zoomed target, while a wide view of a target under good illumination can be taken with a short exposure time. Also, if you assume to take a snapshot of a child at 1 μs, shutter speed faster than 1 μs and keeping a child still during 1 μs will be critical to produce a clear snapshot. Those aspects can be directly applied to the high-resolution fluorescence imaging: the excitation of fluorophore should be carried out with the pulse width shorter than the desirable temporal resolution, the fluorophore-labeled biomolecules should not diffuse or wander around

faster than the exposure time, and the fluorophore itself should be bright and photo-stable to emit enough photons for providing a clear signal as compared to the background. Apart from the detector performance (without a doubt, a state-of-the-art camera is essential for a good snapshot), from chemist's point of view, a smart design of fluorescence probes, which is sufficiently bright (fluorescence quantum yield, $\Phi_{fl}$, > 0.3), photo-stable, and highly selective and sensitive towards the target, can overcome the current limitation of temporal and spatial resolution of fluorescence imaging. Furthermore, development of analytical methods with currently available optical set-up has further improved the spatial resolution of fluorescence detection up to a few tens of nanometer, which is sub-diffraction limit, so-called super-resolution imaging technique.[2,3] In short, simultaneous developments of fluorescence probes and analytical methods are important to improve the resolution of the fluorescence detection.

So far, fluorescence imaging in biological and medical studies has been mostly exploited to monitor the exact location, formation, and disappearance of a certain target. Furthermore, fluorescence detection provides information about not only the localization, but also conformational changes in biomolecules and structural fluctuation occurring on the sub-μs time scale depending on the probe designs. To do so, throughout this study, fluorescence resonance energy transfer (FRET) and photoinduced electron transfer (PET) have been exploited.[1]

FRET is induced by the interaction between transition dipole moment of the donor to the absorption dipole moment of the acceptor, resulting in non-radiative relaxation of the donor accompanied with energy transfer to the acceptor molecules. The FRET efficiency ($E_{FRET}$) can be described as $E_{FRET} = 1/(1 + (r/R_0)^6) \approx I_A/(I_D + I_A)$ where $R_0$ is the Förster distance of the FRET dye pair. $I_D$ and $I_A$ represent fluorescence intensities from donor and acceptor molecules, respectively. Assuming the surrounding environments are constant during the measurement and donor and acceptor molecules can freely rotate, $r$ is the most important factor in $E_{FRET}$, which makes FRET called as a 'molecular ruler'. This approach is useful when donor and acceptor fluorophores are apart each other in a range between 0.5 and 1.5 nm.

On the other hand, provided that there is an appropriate redox potential difference and two chromophores are placed in the van der Waals contact distance, PET occurs from electron donor to electron acceptor molecules, generating a charge-separated state. Because PET occurs at sub-ps to ps time scale, it deactivates a fluorophore in the excited state $10^3$–$10^4$ times faster than fluorescence. In other words, PET induces efficient fluorescence quenching. This phenomenon is

often exploited to design a fluorescence probe that gives fluorescence turn-on upon sensing a target molecule.

The author aimed to investigate biological phenomena by using fluorescence probes based on either FRET or PET. The context of this thesis consists of two parts: (1) monitoring heterogeneous conformations of non-B DNA studied by single-molecule fluorescence spectroscopic techniques (Chapters 1 and 2), and (2) monitoring intracellular singlet oxygen ($^1O_2$) generation produced during photodynamic therapy (Chapters 3-5). For target molecules, non-B DNA and singlet oxygen ($^1O_2$) have been chosen as ex vivo and intracellular targets, respectively.

Introduction of each chapter is shown as below.

In Chapter 1, the folding mechanism and dynamics of the pH-induced conformational change of cytosine-rich DNA oligomer were studied using the combination of FRET and fluorescence correlation spectroscopy (FCS) in the bulk phases and at the single-molecule level.

In Chapter 2, the conformational changes of adenine-rich DNA oligomer induced by pH, intercalator, and dilution were studied using the combination of FRET and FCS in the bulk phases and at the single-molecule level.

In Chapter 3, prior to intracellular $^1O_2$ detection using a fluorescence probe, the author studied photochemistry of Singlet Oxygen Sensor Green, the most widely used commercialized fluorescence probe of $^1O_2$ using various time-resolved spectroscopic techniques.

In Chapter 4, silicon-containing rhodamine (Si-rhodamine) and phenylanthracene dyad was synthesized as a new far-red $^1O_2$ fluorescence probe, and its unprecedented J-aggregate formation was investigated using femtosecond transient absorption measurements and X-ray crystal structural analysis.

In Chapter 5, Si-rhodamine and 9,10-dimethylanthracene dyad was synthesized as a new far-red intracellular $^1O_2$ fluorescence probe, and the visualization of $^1O_2$ formation during photoirradiation of intracellular photosensitizer is presented.

(1) *Principles of Fluorescence Spectroscopy*; Lakowicz, J. R.; Third Edition.; Springer Science, LLC,: Boston, MA, 2006.
(2) Hedde, P.; Nienhaus, G., *Biophys. Rev.* **2010,** *2*, 147.
(3) Gahlmann, A.; Moerner, W. E., *Nat. Rev. Micro.* **2014,** *12*, 9.

# Part 1: Conformational Changes of Non-B DNA Studied by Single-Molecule Fluorescence Microscopy

## Background

### Non-B DNA

DNA, the abbreviation of 'DeoxyriboNucleic Acid', is the basic cellular component that is in charge of the storage of genetic information. DNA is a kind of biopolymer composed of two helical strands of polynucleotides. As revealed by James D. Watson and Francis Crick in 1953, two strands of DNA form a right-handed double stranded helical structure through hydrogen bonding between nucleosides, adenine (A)-thymine (T) and guanine (G)-cytosine (C). If the chain of DNA is assumed to be a polymer, nucleosides and phosphate linker are pendant groups and a backbone of the polymer chain, respectively. Since phosphate is anionic, DNA is often regarded as anionic biopolymer with hydrophilic backbone exposed on its surface and hydrophobic base-pairs inside. This right-handed double helix is generally called B-DNA.

In contrast, DNA strand with repetitive sequences may fold into uncanonical DNA structures such as triplex, tetraplex, left-handed Z-DNA, etc. under a specific condition or by the addition of the external molecules. Those unusual conformations are called non-B DNA. During DNA metabolism (i.e. replication and transcription), the DNA double helix is partially unwound into a single-strand sequence, and this is the moment that the formation of non-B DNA may disrupt normal DNA metabolism and cell differentiation. Thus, the non-B DNA-forming sequences induce the genetic instability and consequently can cause human diseases. On the other hand, deliberate induction of such a non-B DNA can be applied to cancer therapy. Furthermore, non-B DNA is considered to be the fascinating nanomaterial because it does produce any toxic byproducts and are robust during the repetitive working cycles. Taken together, an understanding on the mechanism and dynamics of the structural changes of non-B DNA is undoubtedly important. In Part 1, the author focused on i-motif and A-motif DNA, which are made by C-rich and A-rich DNA oligomers, respectively.

# Chapter 1. pH-Induced Intramolecular Folding of i-Motif DNA

## Introduction

DNA, which acts as the carrier of the genetic information, has a right-handed double helical structure under ordinary physiological conditions. In contrast, repetitive DNA sequences under certain conditions may fold into non-B structures, such as hairpin, triplex, cruciform, left-handed Z-form, tetraplex, etc.[1-3] Since these non-B structure-forming sequences induce the genetic instability and consequently may cause human diseases, the molecular mechanism for their genetic instability has been extensively investigated.[1,2] Especially, it is known that tetraplex DNA-forming sequences are observed frequently in the promoter region of oncogene and human telomeric DNA. Thus, tetraplex DNA, such as intermolecular and/or intramolecular G-quadruplex and i-motif structures, have been an emerging topic in nucleic acids research because they can act as a signpost and a controller for the oncogene expression at the transcription level.[4-10] Furthermore, tetraplex DNA with a higher order structure is regarded as a fascinating material for the nanomachine application[11-15] as well as drug delivery system.[16,17] For instance, Shieh et al. reported that G-quadruplex-porphyrin complex destroys cancer cells selectively under 435 nm irradiation. This means that G-quadruplex can be used as a drug carrier for photodynamic therapy for cancer cells.[16] In addition, Modi et al. developed an i-motif-based nanomachine to map the spatial and temporal pH changes associated with endosome maturation.[14] These studies suggest the great potential of DNA scaffolds responsive to complex triggers in sensing, diagnostics, and targeted therapies in a living cell.

Most studies performed on non-B DNA sequences in oncogene promoter regions have focused on the G-quadruplex due to its inherent structural stability even at neutral pH. Indeed, G-quadruplex-forming sequences have been enormously investigated in terms of their folding topologies and the interactions between organic molecules or DNA-binding proteins and G-quadruplex motifs.[9,18,19] In contrast, relatively few studies have been done on i-motif structures. The conformational change from the cytosine (C)-rich single-stranded DNA to i-motif takes place at slightly acidic pH (≈ pH 6.0).[20] The i-motif structure formed at slightly acidic pH consists of two parallel-stranded C:C+ hemiprotonated base-paired duplexes that are intercalated

in an antiparallel manner, and its pH-dependent structure is significantly affected by the number of cytosine bases,[21] loop length,[22] environmental condition,[23-25] and attached or interacting material with the DNA strands.[26-28] It is known that C-rich sequences are present in or near the regulatory regions of >40% of all genes, including known oncogenes.[29] Recently, Rajendran et al. reported that the transition pH of i-motif structure can be increased by the molecular crowding even up to slightly basic pH (pH 6.6 to 7.4).[25] This being the case, an understanding on the mechanism and dynamics of the structural change of C-rich single-stranded DNA is important. Nonetheless, its biological function and detailed conformation dynamics have not been clearly revealed yet.

In this work, the author comprehensively investigated the mechanism and dynamics of the pH-induced structural change of i-motif using the combination of FRET and FCS in the bulk phases and at the single-molecule level. Compared to the conventional techniques, such as CD and UV-vis spectroscopy, single-molecule FRET and FCS methods are very useful tools to investigate the structure and the dynamics of a protein or DNA. FRET that is called as a molecular ruler is a unique technique to provide valuable information on the structure of biomolecules, such as a protein and DNA.[30] Furthermore, FCS is a very valuable tool to observe the translational diffusion of a biomolecule as well as the sub-μs relaxation, such as the intrachain contact formation.[31,32] Using the FRET technique in the bulk phases and at the single-molecule level, the author clearly show that the partially folded species as well as the single-stranded structure coexist at neutral pH. Furthermore, by measuring the FCS curves of i-motif, the gradual decrease of the diffusion coefficient (*D*) of i-motif with increasing pH was clearly detected, indicating the increase of the molecular size of i-motif.

## Experimental Section

**Materials.** Alexa Fluor 488 C5-maleimide (Alexa 488) and Alexa Fluor 594 C5-maleimide (Alexa 594) were purchased from Invitrogen. In order to prepare Alexa488-C6-3'-$(CCCAAT)_3$CCC-5'-C11-Alexa594 (**D-I-A**), Alexa 594 was labeled to Alexa 488-labeled DNA sequence Alexa488-C6-3'-$(CCCAAT)_3$CCC-5'-C6-SH (**D-I-SH**) obtained from Japan Bio Service. For dye labeling, Alexa 594 was dissolved in 100 mM Na2HPO4/citric acid buffer (pH

7.0). The 10-fold molar excess of Alexa 594 was added to a tube containing **D-I-SH** dissolved in 100 mM $Na_2HPO_4$/citric acid buffer (pH 7.0). The reaction was carried out in dark for 1-2 hour at room temperature. Dye labeling was confirmed by using absorption and fluorescence spectroscopy. The obtained **D-I-A** was dissolved in various pH buffer solutions prepared by the alternate addition of 0.2 M of $Na_2HPO_4$ and 0.1 M of citric acid.

**Steady-State Measurements.** The steady-state UV-Visible absorption, fluorescence and CD spectra were measured using a Shimadzu UV-3100, Horiba FluoroMax-4 and JASCO CD-J720, respectively. The thermal denaturation profile was recorded on a JASCO V-530 spectrometer equipped with a Peltier temperature controller (ETC-505T).

**Fluorescence Lifetime ($\tau_{fl}$) and FCS Measurements.** The $\tau_{fl}$s and FCS experiments of **D-I-A** and Alexa 488 with various pH solutions were measured with a time-resolved fluorescence microscope using confocal optics (MicroTime 200; PicoQuant, Berlin-Adlershof, Germany). In order to measure the $\tau_{fl}$ of freely diffusing **D-I-A**, 50 μl of **D-I-A** solution was loaded into the micro-chamber made by a 1-inch glass cover slip and Secure-Seal (S24733, Invitrogen). The samples were excited through an oil objective (Olympus, UAPON 150XOTIRF; 1.45 NA, 150x) with a 485-nm pulsed laser (PicoQuant, full width at half-maximum 120 ps) controlled by a PDL-800B driver (PicoQuant). The excitation power of ~ 0.15 mW was used. The emission was collected with the same objective and detected by a single photon avalanche photodiode (Micro Photon Devices, PDM 50CT and 100CT) through a dichroic beam splitter (Olympus, DM570), bandpass filter (Olympus, BA510-550), and 50-mm pinhole for spatial filtering to reject out-of-focus signals. The data collected using the PicoHarp 300 TCSPC module (PicoQuant) were stored in the time-tagged time-resolved mode (TTTR), recording every detected photon with its individual timing, which were used for the single-molecule analysis.

In the FCS experiments, the concentration of **D-I-A** was 10 nM. The excitation power of about 45 mW was used and photons were collected into 1 ms bins for 3-4 hours. All of the experimental data were obtained at room temperature.

**Single-Molecule FRET Measurements.** In order to measure the FRET efficiency ($E_{FRET}$) of freely diffusing **D-I-A** in the single-molecule level, 1 nM **D-I-A** solutions containing 10 vol% $\beta$-

mercaptoethanol and 1 mM Trolox were prepared in the respective pH buffers. $\beta$-mercaptoethanol and Trolox are well-known triplet quenchers that decrease blinking events. Single-molecule FRET was carried out with the confocal optics (MicroTime 200; PicoQuant, Berlin-Adlershof, Germany) and two single photon avalanche photodiodes (Micro Photon Devices, PDM 50CT and 100CT) for the simultaneous detection of the FRET donor and acceptor. All samples were excited through an oil objective (Olympus, UPlanSApo, 1.40 NA, 100×) with a 485 nm pulsed laser (PicoQuant, full width at half-maximum 120 ps) controlled by a PDL-800B driver (PicoQuant). The excitation power of about 65 μW was used. Each FIT was taken for one minute with a binning time of 1 ms.

For the $E_{FRET}$ calculation, donor leak intensity to acceptor channel and acceptor detector efficiency against donor detector were determined as 0.04 and 0.88, respectively. In order to create $E_{FRET}$ histogram, the $E_{FRET}$ was calculated as follows:

$$E_{FRET} = \frac{I_A - (\frac{x}{1-x})I_D}{I_A + I_D}$$

where $x$ is donor leak intensity, and $I_D$ and $I_A$ are the intensities of donor and acceptor molecule, respectively. Using Origin (OriginLab) and Microsoft Excel (Microsoft) program, histograms were fitted with Gaussian functions.

## Results and Discussions

**Fluorescence and CD Measurements in the Bulk Phase.** In this study, 21-mer single-stranded DNA, of which both end-sides (5' and 3') were substituted by donor (Alexa 488) and acceptor (Alexa 594) dyes (Alexa 594-C11-5'-CCC-$(TAACCC)_3$-3'-C6-Alexa 488, **D-I-A**, see Figure 1-1a), was used. First of all, the author conducted the measurement of the melting temperature ($T_m$) to elucidate whether the DNA structure is affected by the covalent attachment of the dyes. The $T_m$s of **D-I-A** and **D-I-NH2** in pH 4.8 buffer solutions are determined to be 55.8 ± 0.4 and 55.9 ± 0.4°C, respectively. These $T_m$ values are in accordance with that ($T_m$ = 50.2°C) of 5'-CCC$(TAACCC)_3$-3' at pH 5.0 reported by Shin et al.[26] within an experimental error. These results indicate that the DNA structure remains almost intact after labeling with the dyes. Figure 1-1b shows CD spectra of **D-I-A** as a function of pH. Upon decreasing pH, the positive band

near 270 nm and the negative band near 250 nm, which are due to base stacking and polynucleotide helicity of unstructured single-stranded DNA (open form),[34] respectively, are red-shifted to 285 and 260 nm with the increase of the ellipticity, respectively. These two distinct peaks at 285 and 260 nm are known as characteristic CD bands of i-motif structure.[25,35] This result indicates that the pH-induced conformational change occurs from the open form to i-motif as pH decreases. As described in Figure 1-1c, the transition curves monitored by CD intensities show the sigmoidal feature, implying the conformational change of i-motif takes place via a two-state folding mechanism without any detectable intermediate. From the fitting results of the transition curves for **D-I-A**, the transition midpoint ($x_0$) is determined to be pH = 5.9.

On the other hand, the fluorescence intensities ($I_f$) of the donor (Alexa 488) attached to **D-I-A** is significantly quenched with decreasing pH (Figure 1-2a), whereas the fluorescence intensity of pristine Alexa 488 is independent in the range of pH 4-10. Thus, the changes of the fluorescence intensities of **D-I-A** with decreasing pH are closely related to the conformational change of **D-I-A**. That is, upon decreasing pH, the open structure is folded into i-motif structure, resulting in the efficient FRET from donor to acceptor. From the ratio of the fluorescence intensities of acceptor to total emission ($I_A/(I_A + I_D)$) of **D-I-A** as a function of pH, $x_0$ is determined to be pH = 6.0 (Figure 1-2b). Here, it is noteworthy that the value of $x_0$ is consistent with that determined from the CD intensity within an experimental error, while the transition region of the transition curve is wider than that obtained from the CD intensity (Figure 1-2b). This disagreements between two transition region depending on the measurement methods implies that the conformational change of i-motif could not be interpreted by simple two-state mechanism.

**$\tau_{fl}$ Measurements of D-I-A.** In order to further examine the folding of **D-I-A** from open form (single-strand structure) to i-motif, the $\tau_{fl}$s of **D-I-A** and **D-I-NH$_2$** were measured as a function of pH. Figure 1-3a shows all fluorescence decay profiles of the donor dye (Alexa 488) of **D-I-A** measured in various pH solutions. As a preliminary test, the author confirmed the fluorescence decay profiles of **D-I-NH$_2$** and **D-I-SH**, two control strands without acceptor fluorophore, can be fitted by a single exponential function with a relaxation time of 4.0 ± 0.1 ns. In contrast, all decay profiles of donor fluorescence of **D-I-A**, as shown in Figure 1-3a, were expressed by a biexponential function. By a simple analysis of all the fluorescence decay profiles, it was found that at least three components with different $\tau_{fl}$s are involved in the pH-induced conformational

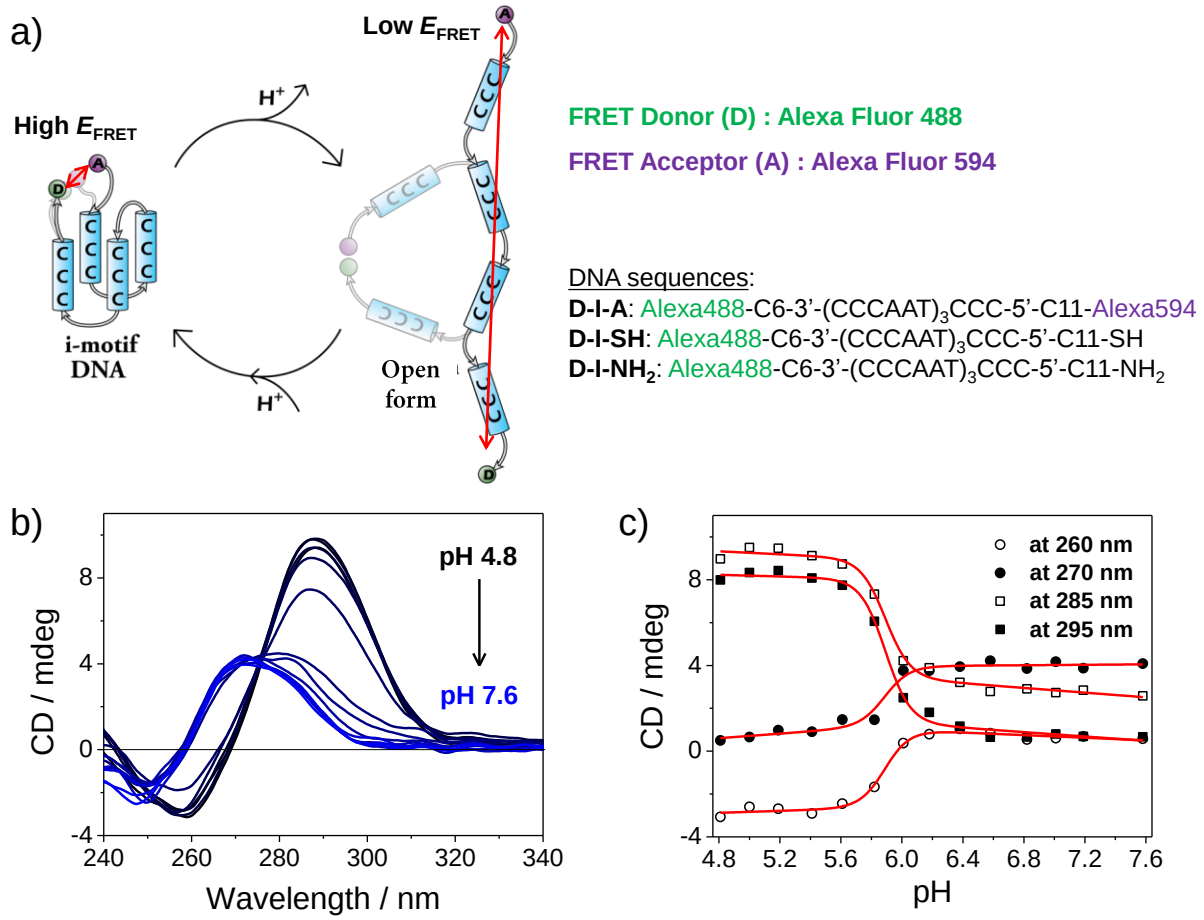


**Figure 1-1.** The pH-induced conformational change of i-motif and CD spectra. **(a)** Schematic illustration of the reversible pH-induced conformational change of i-motif and DNA sequences used in this study. C6 and C11 are alkyl linkers to connect DNA 21-mer and dyes or functional groups. **(b)** CD spectra of **D-I-A** in various pH solutions. **(c)** Variation of CD intensity of **D-I-A** probed at different wavelength as a function of pH. Theoretical fits obtained from the fitting analysis are shown in red.

dynamics of **D-I-A**. Thus, all the decay profiles of **D-I-A** were fitted with a triexponential function. A global fitting analysis of all decay profiles revealed three relaxation times of 0.4, 1.0, and 2.8 ns in the pH-induced conformational change of **D-I-A**. As shown in Figure 1-3b, the fastest component ($\tau_1$ = 0.4 ns) is the major component at acidic solutions, whereas two components ($\tau_2$ = 1.0 and $\tau_3$ = 2.8 ns) with relatively slower decay times are dominantly observed

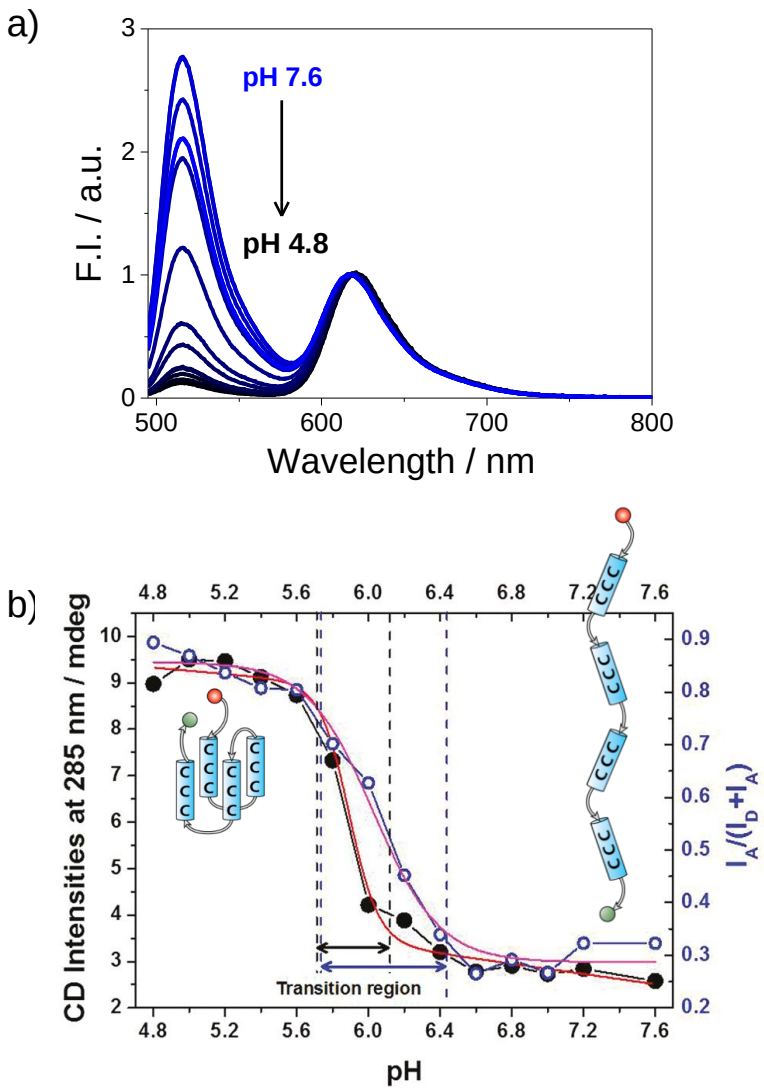


**Figure 1-2. (a)** Fluorescence spectra of **D-I-A** in various pH solutions. The fluorescence spectra were normalized at 618 nm. **(b)** Changes in the ratio of the fluorescence intensities of acceptor to total emission ($I_A/(I_A + I_D)$) (open circles) and CD intensities of **D-I-A** probed at 285 nm (closed circles), respectively, as a function of pH. Theoretical fits obtained from the fitting analysis are shown in red and pink for CD intensity and ($I_A/(I_A + I_D)$), respectively.

at neutral pH solutions. Considering the two-state conformational change between i-motif and the open form, only two decay components should be observed. As shown in Figure 1-3b, however, three different $\tau_{fl}$s were observed during pH increase from 4.8 to 7.6, indicating that

there are at least three species involved in the pH-induced conformational change of i-motif.

This result is in contrast with the result obtained by CD spectroscopy, showing the typical two-state transition. Recently, Trent groups reported that the CD spectra could not distinguish the different species with similar physical properties,[36] indicating that the CD signal is not a highly sensitive tool to observe conformational changes of DNA, such as G-quadruplex and i-motif. Interestingly, the decay times of two fast components ($\tau_1$ = 0.4 and $\tau_2$ = 1.0 ns) measured from donor in acidic and neutral pH solutions, respectively, were also observed in the acceptor's fluorescence decay profiles as rise components.

Considering the pH-induced conformational change of i-motif, it is assumed that the fast-decay component of 0.4 ns observed at acidic pH is attributed to i-motif, whereas the component of 1.0 ns may be attributed to a partially folded form, which can induce the energy transfer. Dhakal et al. found the coexistence of the partially folded form and i-motif in the C-rich human insulin linked polymorphism region (ILPR) oligonucleotides using the laser tweezers technique.[37] They also suggested that the formation of i-motif is decreased by increasing pH, while the partially folded structure with a small fraction is pH-independent (pH 5.5-7.0: 6.1%). Moreover, using experimental and theoretical methods, Dettler et al. reported that the classical i-motif structure is predominant at slightly acidic pH (pH 4.2-5.2), whereas i-motif-like is the most significant species at neutral pH.[38] These results agree with the obtained results that the fast-decay component of 0.4 ns represents i-motif, while 1.0 ns comes from the partially folded form. On the other hand, it is suggested that although the $\tau_{fl}$ (2.8 ± 0.1 ns) of the slow-decay component observed from **D-I-A** is shorter than those (4.0 ± 0.1 and 3.9 ± 0.2 ns) of **D-I-NH$_2$** and **D-I-SH**, the slow decay component of 2.8 ns observed at neutral pH is attributed to the open form. The reason for the decrease of the $\tau_{fl}$ of donor molecule from 4.0 to 2.8 ns is probably due to a transient interaction between two dyes by the intrachain contact formation because there is no change in the $\tau_{fl}$ when DNA is singly labeled with a donor dye.

**Single-Molecule FRET Measurements of D-I-A.** Generally, the FRET efficiency ($E_{FRET}$), which relates to the donor's $\tau_{fl}$, has been used as an indicator on donor-acceptor distance:

$$E_{FRET} = 1 - \frac{\tau_{DA}}{\tau_D} = \frac{1}{1 + (\frac{r}{R_0})^6} \quad (1)$$

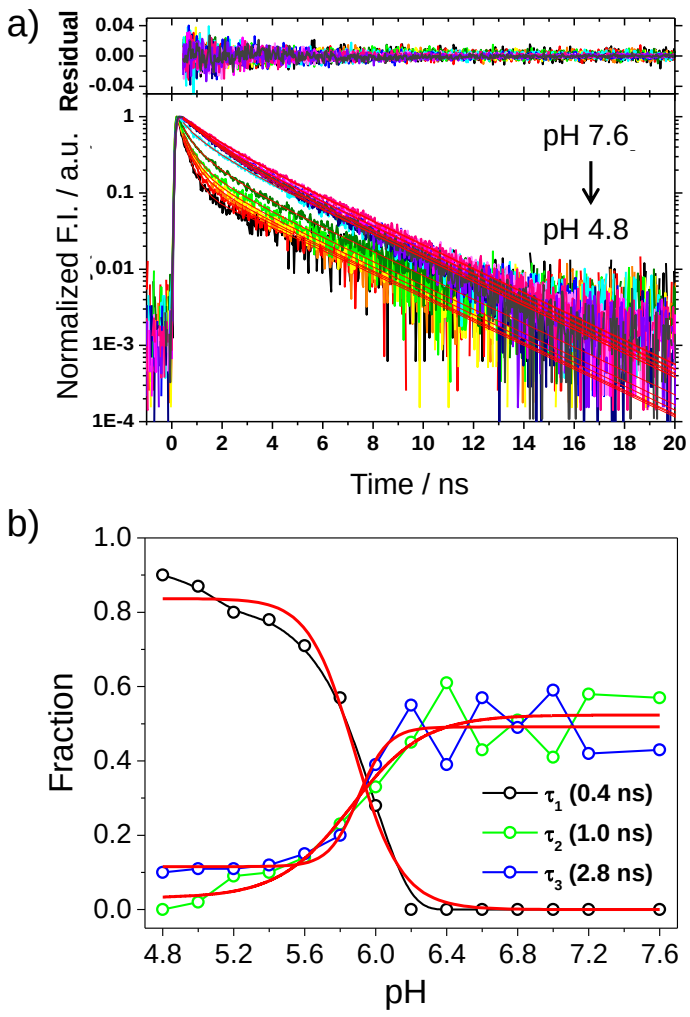


**Figure 1-3.** Fluorescence decay profiles and the fraction of the relevant decay components. **(a)** Global fitting results of fluorescence decay profiles of the donor attached to **D-I-A** as a function of pH. The theoretical fits obtained from the global fitting analysis are shown in red. **(b)** Changes in the fraction of the relevant decay components as a function of the pH.

where $\tau_{DA}$ and $\tau_D$ are the donor's $\tau_{fl}$s in the presence and absence of an acceptor, respectively, $r$ is the interdye distance, and $R_0$ is the Förster radius at which $E_{FRET}$ = 0.5 ($R_0$ for the Alexa 488 (donor)-Alexa 594 (acceptor) system is 60 Å[39] and $\tau_D$ = 4.0 ns). Using $\tau_{fl}$ determined at each pH, $\tau_{fl}$ for i-motif and the partially folded form are calculated to be 0.90 and 0.75, respectively. Using eq 1, $r$ for i-motif and the partially folded form are calculated to be 4.2 and 5.0 nm, respectively.

The $r$ (4.2 nm) determined for i-motif is close to the maximum dimension of completely folded FDH (fullerene ($C_{60}$) attached to both end sides of 5'-CCC(TAACCC)$_3$-3') reported by Shin et al (4.1 nm),[26] whereas the $r$ (5.0 nm) for the partially folded form is greatly shorter than the maximum dimension of fully expanded FDH (7.8 nm), supporting that the fast-decay component of 1.0 ns has a partially folded form as explained above.

To confirm the coexistence of a partially folded form observed in the time-resolved fluorescence experiments, the author investigated the pH-induced conformation change of i-motif using single-molecule fluorescence spectroscopy. Single-molecule fluorescence spectroscopy provides an insight into the behavior of each individual molecule and consequently allows a detailed observation of subpopulations in structures or dynamics hidden under ensemble-averaged results.[40-42] Figure 1-4 displays the $E_{FRET}$ distributions determined from the fluorescence intensity trajectories (FITs) of single-molecule **D-I-A** in solution at pH 4.8, 5.8, and 7.2. As depicted in Figure 1-4, the $E_{FRET}$ histogram observed at pH 4.8 shows a single $E_{FRET}$ peak centered at 0.86, whereas the $E_{FRET}$ distributions of **D-I-A** at higher pH (pH 5.8 and 7.2) show three distinct peaks (0.32, 0.59, and 0.86; the peak with $E_{FRET} \sim 0.05$ is probably attributed to the DNA singly labeled with a donor dye). Interestingly, the peak at $E_{FRET} \sim 0.86$ observed at pH 4.8 is close to that observed from the $\tau_{fl}$ of i-motif form within an experimental error ($E_{FRET} \sim 0.90$, Figure 1-3b). In addition, with increasing pH, the population of the component with $E_{FRET} \sim 0.86$ is disappeared, and then the peaks at $E_{FRET} \sim 0.32$ and $\sim 0.59$ are observed as main components at a higher pH. Considering the pH-induced conformational change of i-motif, it is suggest that the component with $E_{FRET} \sim 0.86$ is attributed to i-motif. Using eq 1, the $r$ for the structural species with $E_{FRET} \sim 0.32$ and 0.59 are calculated to be 6.8 and 5.6 nm, respectively. These values are close to those of fully expanded FDH (7.8 nm)[26] and the partially folded form ($\tau_2$ = 1.0 ns, 5.0 nm) observed in the time-resolved fluorescence experiment within an experimental error, indicating that two low $E_{FRET}$ of 0.32 and 0.59 come from the open form and the partially folded form, respectively. These results support that the partially folded species, which could not be observed by the CD spectra, coexists with the single-stranded structure at neutral pH. Here, it is noteworthy that the partially folded form reported in this study is not observed at acidic pH, whereas that proposed by Dhakal et al. is pH independent (pH 5.5-7.0: 6.1%).[37] This implies that the partially folded forms proposed by this study and by Dhakal et al. may have different structures.

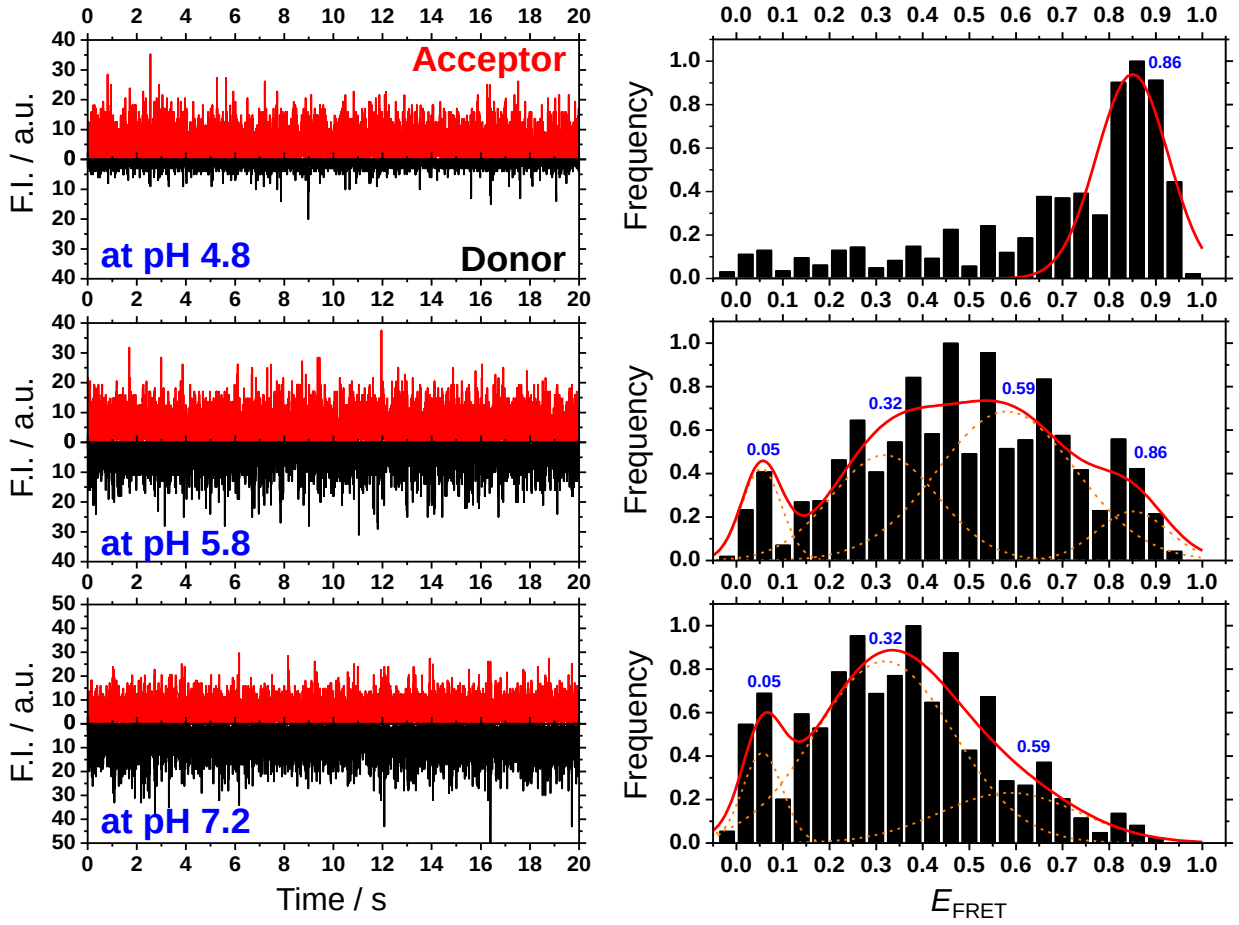


**Figure 1-4.** Single-molecule fluorescence FITs (left) and $E_{FRET}$ distributions (right) of single-molecule **D-I-A** at pH 4.8 (top), 5.8 (middle), and 7.2 (bottom) (binning time: 1 ms). The red solid lines denote the Gaussian fitting curves.

In addition, although i-motif forming sequences are considered to be present in the promoter regions of various well-known oncogenes[5] and telomeric DNA,[6] the structure of i-motif in vivo has not been directly observed. One of the reasons might be the neutral environment of cellular interior, whereas i-motif is dominantly formed by hemi-protonation of cytosine base at acidic condition. However, as mentioned previously, C-rich single-stranded DNA can form i-motif structures not only at acidic pH but also at neutral pH under molecular crowding condition, which is similar to the intracellular environment.[25] Considering those previous studies, therefore, the formation of i-motif in vivo is theoretically possible. Thus, it is extremely crucial to confirm

the existence of i-motif (or the partially folded form and i-motif-like form) at neutral pH. In this respect, the result presented here implies that the partially folded species may exist in vivo and play an important role in a biological function, such as replication, regulation, and transcription in physiological conditions.

**FCS Measurements of D-I-A.** In order to further elucidate the conformational dynamics of i-motif, the molecular diffusion time of **D-I-A** was measured at various pHs. The molecular diffusion time reflects not only the global structural change of a biomolecule occurring in a protein or DNA folding/unfolding process but also the intermolecular interaction between a biomolecule and solvent molecules.[43-45] Thus, the molecular diffusion time can provide the information on the change in molecular size associated with the conformational change of a biomolecule. In this respect, FCS is a very useful tool to observe the translational diffusion of a biomolecule as well as the sub-μs relaxation corresponding to the intrachain contact formation.[31,32,46] To elucidate the translational diffusion of i-motif, the FCS curves of **D-I-A** were measured at various pHs. In the presence of a dynamic process, such as conformational relaxation resulting in a change of the fluorescence intensity, the autocorrelation function can be expressed by

$$G(\tau) = \frac{1}{N}(1+\frac{\tau}{\tau_{\text{diff}}})^{-1}[1+K^{c}_{\text{obsd}}\exp\left(\frac{\tau}{\tau^{c}_{\text{obsd}}}\right)] \quad (2)$$

where $N$ is the average number of molecules in the observed volume, $\tau_{\text{diff}}$ is the molecular diffusion time, $K^{c}_{\text{obsd}}$ is the observed amplitude of the intrachain contact formation kinetics due to changes of the donor-acceptor distance, and $\tau^{c}_{\text{obsd}}$ is the observed time of intrachain contact formation. Figure 1-5a shows the representative FCS data of Alexa 488 at pH of 7.0 and **D-I-A** recorded at pH 7.6 and 4.8. From the molecular diffusion times obtained by the FCS analysis using eq 2 and the diffusion coefficient ($D$ = 4.5 × $10^{10}$ $m^2$ $s^{-1}$) of Alexa 488 at neutral pH,[47] it was found that the diffusion coefficient of **D-I-A** gradually decreased upon increasing pH (Figure 1-5b). Since the diffusion coefficient is inversely proportional to the hydrodynamic radius ($R_h$) of a molecule, the decrease of $D$s with increasing pH indicates that the hydrodynamic radius of the open form is 1.6 times larger than that of i-motif ($R_h$ _open/$R_h$ _i-motif ≈ 1.6). In addition, it is notable that the molecular size of i-motif is gradually increasing with pH.

There are several factors that govern the diffusion process of molecules in solution: the size,

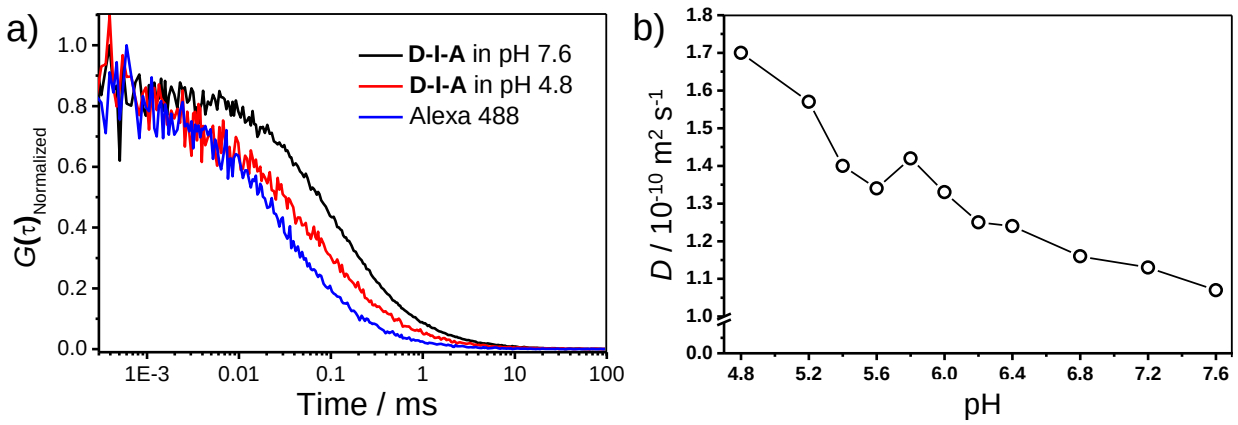


**Figure 1-5. (a)** Representative FCS curves of **D-I-A** at pH 7.6 (black) and 4.8 (red) and Alexa488 at pH 7.0 (blue). **(b)** Plot of the variation of the molecular diffusion coefficients (*D*) of **D-I-A** determined in various pH solutions.

shape of the molecule, and intermolecular interaction between the solvent and the diffusing molecule. To investigate the origin of the deccelerated diffusion of the open form, the effect of the molecular shape on *D* was examined. According to the Stokes equation, the frictional coefficient ($f_0$) for a spherical molecule is expressed as follows:

$$f_0 = 6\pi\eta R_0$$

where $\eta$ is the viscosity of the solvent, and $R_0$ is the radius of a spherical molecule. Generally, the frictional coefficient ($f$) of the molecule in solution depends on its size and shape. When the shape is deformed from the spherical symmetry, the friction should be different from eq 3. Although it is unknown the exact shapes of the partially folded and the open form, some previous studies have suggested that the partially folded form has a triplex structure, which is similar to the tetraplex structure of i-motif.[33,45] Thus, it is assumed that i-motif and the partially folded form have a spherical shape. In contrast, the open form may have a rod-like shape because duplex DNA generally behaves like a rigid rod, and **D-I-A** consists of the short 21-mer DNA sequence, which has a helical structure.[26,49] If the molecule possesses a rod-like shape, $f/f_0$ is given by[48]

$$\frac{f}{f_0} = \frac{(2/3)^{\frac{1}{3}}(a/b)^{2/3}}{ln2\left(\frac{a}{b}\right) - 0.3} \quad (4)$$

where *a* is the half-length, and *b* is the radius. In the case of a single-stranded **D-I-A**, the *a* and *b* are calculated to be roughly 3.8 and 0.3 nm, respectively. Using eq 4, $f/f_0$ value of the single-stranded **D-I-A** is calculated to be 1.62, which is close to the experimentally observed value ($R_h$ _open/$R_h$ _i-motif = $f/f_0 \approx 1.6$). This agreement indicates that the change of the shape of i-motif plays an important role in its diffusion process. However, the shape of the open form at neutral pH should be near to a random coil rather than a rigid rod because of its flexibility to access various conformations. Furthermore, the gradual decrease of *D* associated with the conformational change of i-motif cannot be explained only by the effect of the molecular shape on *D*. As mentioned above, the molecular diffusion process is greatly affected by the intermolecular interaction between a biomolecule and solvent molecules. At neutral pH, the single-stranded DNA has a random coil structure, and consequently its solvent exposed surface area increases, indicating the increase in the binding site of water molecules and DNA. Hence, it is assumed that the conformational change of i-motif is initiated by the deprotonation of cytosine in two parallel-stranded C:C+ base-paired duplex, leading to the increase of the interaction between the i-motif and water molecules. Thus, DNA molecule at neutral pH is subjected to a more frictional constraint in the solvents than at an acidic pH.

It is well-known that the stability of G-quadruplex structure and the B-form of duplex DNA are regulated by hydration,[24,50,51] for instance, the thermodynamic stability of G-quadruplex increases as the water activity is reduced (dehydration), and the surface area accessible to water is minimized. In addition, Sherman et al. showed that the denaturant-induced unfolding reaction of protein L leads to the gradual expansion of the radius of gyration due to the interaction between solvent molecules and a protein, and the solvation energy associated with the denaturation of a protein is linearly increased.[52] These results indicate that the hydration has a vital role in the stabilization of biomolecular structure (or protein). From this point of view, the gradual decrease of *D* associated with the conformational change of i-motif is not only due to the continuous change in the intermolecular interaction between i-motif and solvent accompanied by the increase of pH but also to the change in its shape.

Additionally, the partially folded form at neutral pH was observed using $\tau_{fl}$ and single-molecule $E_{FRET}$ measurements. Recently, Dhakal et al. and Dettler et al. found the coexistence of

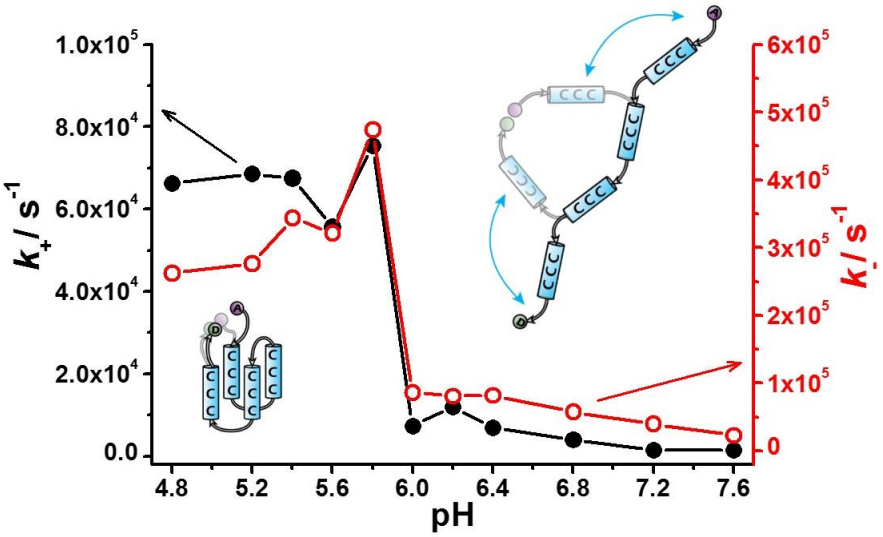


**Figure 1-6.** Rates of the intrachain contact formation ($k_+$, closed circles) and dissociation ($k_-$, open circles) of **D-I-A** determined from the FCS experiments as a function of pH. Responsive fluctuational motions occurred at i-motif and open form are illustrated representatively in left and right sides, respectively.

the partially folded form and i-motif at neutral pH.[37,38] Furthermore, it has been suggested that C-rich DNA can form multiple i-motif structures.[53,54] In light of the previous reports and the results of this study, the possibility that the gradual change in the molecular size shown in Figure 1-5b is due to the existence of spectrally silent multiple species cannot be excluded.

On the other hand, FCS can observe the sub-μs relaxation corresponding to intrachain contact formation or initial folding events of a biomolecule as mentioned previously.[31,32,46] Since the intrachain contact formation is recognized as an early stage interaction in the folding process of a biomolecule, an elucidation of the intrachain contact formation is important for understanding the mechanism and dynamics of the conformational change of i-motif. Figure 1-6 shows the rate constants of intrachain contact formation calculated from the observed amplitude and the observed time constant. As given in Figure 1-6, rate constants of the intrachain contact formation ($k_+$) and dissociation ($k_-$) show the sigmoidal feature. The averaged $\langle k_+ \rangle$ of **D-I-A** at acidic and neutral pH is determined to be $(6.7 \pm 0.7) \times 10^4$ and $(5.5 \pm 4.1) \times 10^3$ $s^{-1}$, respectively, whereas

the averaged $\langle k_- \rangle$ was calculated to be (3.4 ± 0.8) × $10^5$ and (6.2 ± 2.6) × $10^4$ $s^{-1}$, respectively. Considering the main species of each pH, the $\langle k_+ \rangle$ and $\langle k_- \rangle$ observed at acidic and neutral pH may correspond to rate constants of end-to-end contact formation and dissociation of i-motif and the open form, respectively. Especially, the $\langle k_+ \rangle$ and $\langle k_- \rangle$ observed at neutral pH are close to those for 21-mer DNA hairpin, $(dT)_{21}$ and $(dA)_{21}$, reported by Bonnet et al.[32] within an experimental error, supporting the rates observed in this study are due to the intrachain contact formation and dissociation of DNA. Here, it is noteworthy that the $k_+$ and $k_-$ for i-motif are 510 times faster than those for the open form. Although i-motif has a compact tetraplex structure compared to the open form, there are intrinsic conformational changes at the fluorescent site, including the motion of the alkyl chain connecting the labeled dye to DNA. These fluctuational movements, such as the intrachain contact formation and dissociation, bring about a change of the fluorescence intensity. In contrast, as explained previously, the open structure suffers from a frictional constraint in the solvents than i-motif because of the increased hydration and its restrained dynamic flexibility. Conversely, the dynamic flexibility of i-motif at acidic pH is increased by the dehydration. Moreover, the distance between two dyes in the open form is farther than in i-motif structure. Accordingly, the intrachain contact formation for the open form should be much slower compared to that for i-motif. In addition, the slower intrachain contact formation observed from the open form may be attributed to an early stage interaction in the folding process of the unstructured open form.

**Conclusion**

The author thoroughly investigated the pH-induced conformational dynamics of i-motif using the combination of FRET and FCS techniques. It is known that i-motif can be formed at not only acidic pH but also at neutral pH under molecular crowding conditions, which is similar to the intracellular environment.[25] In addition, C-rich sequences are known to be present in or near the regulatory regions of >40% of all genes (including known oncogenes).[29] In light of those previous studies, the formation of i-motif in vivo is theoretically possible, and an understanding on the mechanism and dynamics of the structural change of C-rich single-stranded DNA is extremely important. In addition, despite numerous studies on i-motif, its detailed conformational dynamics have been rarely reported. Using the FRET technique in the bulk

phases and at the single-molecule level, it was clearly shown that the partially folded species, which could not be observed by the CD spectra, coexist with the single-stranded structure at neutral pH, supporting that the partially folded species may exist substantially in vivo and play an important role in a process of gene expression. Furthermore, the dynamics due to the intrachain contact formation and dissociation as well as the changes of the diffusion coefficient of i-motif with increasing pH were investigated. From the quantitative analysis of FCS curves, it was found that the gradual decrease of the diffusion coefficient (*D*) of i-motif with increasing pH can be interpreted in terms of the continuous change in the intermolecular interaction between i-motif and solvent accompanied by the increase of pH and the change of the shape of the DNA. Moreover, FCS analysis showed that the intrachain contact formation and dissociation for i-motif are 510 times faster than that for the open form. This faster dynamics of i-motif with a compact tetraplex is due to the intrinsic conformational changes at the fluorescent site, including the motion of alkyl chain connecting the dye to DNA, whereas the slower intrachain contact formation observed from the open form is due to the DNA motion, corresponding to an early stage interaction in the folding process of the unstructured open form. The obtained results will certainly contribute to further progress on in-depth biological studies of i-motif DNA and the range of its application.

**References**


(1) Bacolla, A.; Wells, R. D. *Mol. Carcinog.* **2009**, *48*, 273.
(2) Wang, G.; Vasquez, K. M. *Mutat. Res.* **2006**, *598*, 103.
(3) Phan, A. T.; Kuryavyi, V.; Patel, D. J. *Curr. Opin. Struct. Biol.* **2006**, *16*, 288.
(4) Rankin, S.; Reszka, A. P.; Huppert, J.; Zloh, M.; Parkinson, G. N.; Todd, A. K.; Ladame, S.; Balasubramanian, S.; Neidle, S. *J. Am. Chem. Soc.* **2005**, *127*, 10584.
(5) Brooks, T. A.; Kendrick, S.; Hurley, L. *FEBS J.* **2010**, *277*, 3459.
(6) Phan, A. T.; Mergny, J. L. *Nucleic Acids Res.* **2002**, *30*, 4618.
(7) Ahmed, S.; Kintanar, A.;Henderson, E. *Nat. Struct. Biol.* **1994**, *1*, 83.
(8) Brooks, T. A.; Hurley, L. H. *Nat. Rev. Cancer* **2009**, *9*, 849.
(9) Wu, Y.; Brosh, R. M., Jr. *FEBS J.* **2010**, *277*, 3470.
(10) Balasubramanian, S.; Neidle, S. *Curr. Opin. Chem. Biol.* **2009**, *13*, 345.
(11) Xu, Y.; Hirao, Y.; Nishimura, Y.; Sugiyama, H. *Bioorg. Med. Chem.* **2007**, *15*, 1275.
(12) Wang, C.; Huang, Z.; Lin, Y.; Ren, J.; Qu, X. *Adv. Mater.* **2010**, *22*, 2792.
(13) Yang, Y.; Liu, G.; Liu, H.; Li, D.; Fan, C.; Liu, D. *Nano Lett.* **2010**, *10*, 1393.

(14) Modi, S.; M, G. S.; Goswami, D.; Gupta, G. D.; Mayor, S.; Krishnan, Y. *Nat. Nanotechnol.* **2009**, *4*, 325.
(15) Krishnan, Y.; Simmel, F. C. *Angew Chem. Int. Ed.* **2011**, *50*, 3124.
(16) Shieh, Y. A.; Yang, S. J.; Wei, M. F.; Shieh, M. J. *ACS Nano* **2010**, *4*, 1433.
(17) Neidle, S. *Curr. Opin. Struct. Biol.* **2009**, *19*, 239.
(18) Huppert, J. L. *FEBS J.* **2010**, *277*, 3452.
(19) Bardin, C.; Leroy, J. L. *Nucleic Acids Res.* **2008**, *36*, 477.
(20) Gehring, K.; Leroy, J. L.; Gueron, M. *Nature* **1993**, *363*, 561.
(21) Mergny, J.-L.; Lacroix, L.; Han, X.; Leroy, J.-L.; Helene, C. *J. Am. Chem. Soc.* **1995**, *117*, 8887.
(22) Kendrick, S.; Akiyama, Y.; Hecht, S. M.; Hurley, L. H. *J. Am. Chem. Soc.* **2009**, *131*, 17667.
(23) Zhou, J.; Wei, C.; Jia, G.; Wang, X.; Feng, Z.; Li, C. *Mol. Biosyst.* **2010**, *6*, 580.
(24) Miyoshi, D.; Karimata, H.; Sugimoto, N. *J. Am. Chem. Soc.* **2006**, *128*, 7957.
(25) Rajendran, A.; Nakano, S.; Sugimoto, N. *Chem. Commun.* **2010**, *46*, 1299.
(26) Shin, S. R.; Jin, K. S.; Lee, C. K.; Kim, S. I.; Spinks, G. M.; So, I.; Jeon, J.-H.; Kang, T. M.; Mun, J. Y.; Han, S.-S.; Ree, M.; Kim, S. J. *Adv. Mater.* **2009**, *21*, 1907.
(27) Li, X.; Peng, Y.; Ren, J.; Qu, X. *Proc. Natl. Acad. Sci. U.S.A.* **2006**, *103*, 19658.
(28) Fedoroff, O. Y.; Rangan, A.; Chemeris, V. V.; Hurley, L. H. *Biochemistry* **2000**, *39*, 15083.
(29) Huppert, J. L.; Balasubramanian, S. *Nucleic Acids Res.* **2007**, *35*, 406.
(30) Lakowicz, J. R. *Principles of fluorescence spectroscopy*; 3rd ed.; Springer: New York, 2006.
(31) Choi, J.; Kim, S.; Tachikawa, T.; Fujitsuka, M.; Majima, T. *Phys. Chem. Chem. Phys.* **2011**, *13*, 5651.
(32) Bonnet, G.; Krichevsky, O.; Libchaber, A. *Proc. Natl. Acad. Sci. U.S.A.* **1998**, *95*, 8602.
(33) McIlvaine, T. C. *J. Biol. Chem.* **1921**, *49*, 183.
(34) Rajendran, A.; Nair, B. U. *Biochim. Biophys. Acta* **2006**, *1760*, 1794.
(35) Guo, K.; Gokhale, V.; Hurley, L. H.; Sun, D. *Nucleic Acids Res.* **2008**, *36*, 4598.
(36) Dailey, M. M.; Miller, M. C.; Bates, P. J.; Lane, A. N.; Trent, J. O. *Nucleic Acids Res.* **2010**, *38*, 4877.
(37) Dhakal, S.; Schonhoft, J. D.; Koirala, D.; Yu, Z.; Basu, S.; Mao, H. *J. Am. Chem. Soc.* **2010**, *132*, 8991.
(38) Dettler, J. M.; Buscaglia, R.; Cui, J.; Cashman, D.; Blynn, M.; Lewis, E. A. *Biophys. J.* **2010**, *99*, 561.
(39) Rothwell, P. J.; Mitaksov, V.; Waksman, G. *Mol. Cell.* **2005**, *19*, 345.
(40) Roy, R.; Hohng, S.; Ha, T. *Nat. Methods* **2008**, *5*, 507.
(41) Liu, R.; Hu, D.; Tan, X.; Lu, H. P. *J. Am. Chem. Soc.* **2006**, *128*, 10034.
(42) Tan, X.; Nalbant, P.; Toutchkine, A.; Hu, D. H.; Vorpagel, E. R.; Hahn, K. M.; Lu, H. P. *J. Phys. Chem. B* **2004**, *108*, 737.
(43) Terazima, M. *Phys. Chem. Chem. Phys.* **2006**, *8*, 545.
(44) Choi, J.; Terazima, M. *J. Phys. Chem. B* **2002**, *106*, 6587.
(45) Choi, J.; Yang, C.; Kim, J.; Ihee, H. *J. Phys. Chem. B* **2011**, *115*, 3127.

(46) Neuweiler, H.; Johnson, C. M.; Fersht, A. R. *Proc. Natl. Acad. Sci. U.S.A.* **2009**, *106*, 18569.
(47) Nitsche, J. M.; Chang, H. C.; Weber, P. A.; Nicholson, B. J. *Biophys. J.* **2004**, *86*, 2058.
(48) Van Holde, K. E.; Johnson, W. C.; Ho, P. S. *Principles of physical biochemistry*; 2nd ed.; Pearson/Prentice Hall: Upper Saddle River, N.J., 2006.
(49) Jin, K. S.; Shin, S. R.; Ahn, B.; Rho, Y.; Kim, S. J.; Ree, M. *J. Phys. Chem. B* **2009**, *113*, 1852.
(50) Miller, M. C.; Buscaglia, R.; Chaires, J. B.; Lane, A. N.; Trent, J. O. *J. Am. Chem. Soc.* **2010**, *132*, 17105.
(51) Miyoshi, D.; Nakamura, K.; Tateishi-Karimata, H.; Ohmichi, T.; Sugimoto, N. *J. Am. Chem. Soc.* **2009**, *131*, 3522.
(52) Sherman, E.; Haran, G. *Proc. Natl. Acad. Sci. U.S.A.* **2006**, *103*, 11539.
(53) Dai, J.; Hatzakis, E.; Hurley, L. H.; Yang, D. *PLoS One* **2010**, *5*, e11647.
(54) Dai, J.; Ambrus, A.; Hurley, L. H.; Yang, D. *J. Am. Chem. Soc.* **2009**, *131*, 6102.

# Chapter 2. Self-Assembly of A-motif DNA

## Introduction

In contrast to B-DNA that has a canonical right-handed double helical structure with Watson-Crick base pairing under the ordinary physiological conditions, repetitive DNA sequences under certain conditions may fold into non-B structure such as hairpin, triplex, cruciform, left-handed Z-form, tetraplex, etc.[1-3] Because these non-B structure-forming sequences induce the genetic instability and consequently may cause human diseases, the molecular mechanism for their genetic instability has been extensively investigated.[2] Furthermore, nanotechnology using non-B DNAs is an emerging field because non-B DNAs are robust and do not produce any toxic byproducts during a repetitive working cycle.[4-8] Among repetitive DNA sequences, single-stranded adenine-rich nucleic acids such as polydeoxyadenylic acid (poly(dA)) or polyadenylic acid (poly(A)) have attracted considerable aion because of their unique structure at acidic pH[9,10] and selective binding ability to organic molecules.[11-15] Because poly(A) is a tail component of mRNA in all eukaryotic cells and plays a key role in the stability of mRNA and translation initiation by its elongation and shortening,[16] the structure and the self-assembly of poly(A) have been intensively studied for several decades. Poly(A) is present as a right-handed helical single strand stabilized by the π-π stacking of adenine bases at alkaline and neutral pH, whereas poly(A) at acidic pH forms a right-handed helical duplex with parallel-mannered chains and tilted protonated bases.[9] Rich et al. proposed that the parallel duplex is stabilized by two factors: the hydrogen bonds between two protonated adenine bases and electrostatic attraction between the positively charged protons at the N(1) atoms of the adenines and the negatively charged phosphate groups (Figure 2-1a).[10] In addition, it was known that there are three different acidic conformations of poly(A): A-form, B-form, and frozen form.[17-21] On the other hand, small crescent-shaped alkaloids such as coralyne[11,13,22,23] and sanguinarine[14,24,25] can bind to poly(A) and induce a stable antiparallel duplex. The self-assembly of poly(A) formed by protonation or molecular binding is so-called "A-motif". Furthermore, A-motif is widely used for the nanotechnology because of its unique structure at acidic pH and selective binding ability to organic molecules.[6,26-28]

Although poly(A) is of higher significance than poly(dA) in terms of biological relevance, poly(dA) may have more potential than poly(A) for further application in nanotechnology as a building block or sensory material because of the superior stability of DNA structure as compared to RNA structure. This being the case, an understanding on the self-assembly of poly(dA) is also undoubtedly important. However, there have been very few studies that compare and characterize two distinct structures of poly(dA) duplex induced by pH and intercalator binding.

Here, using the FRET technique, the self-assemblies of adenine oligomer induced by pH and coralyne binding were investigated at the single-molecule level. For this study, two different oligonucleotides, **A-motif 1** (Alexa488-5'-$(dA)_{20}$-3'-Cy5-5'-$(dA)_{20}$-3'-Alexa488) and **A-motif 2** (Alexa488-5'-$(dA)_{20}$-3'-Cy5-3'-$(dA)_{20}$-5'-Alexa488), were used. The strand polarities of the two oligonucleotides at the center are different as shown in Figure 2-1b. Both end-sides were substituted by donor molecules (Alexa488), and the center of the oligonucleotide was substituted by acceptor molecule (Cy5). In addition, coralyne, one of the anti-leukemic drugs, is used as an intercalator to induce antiparallel duplex. Results presented here show that **A-motif 1** forms the wire-type duplex at acidic pH, whereas the same conformation of **A-motif 2** is induced by binding of coralyne at neutral pH. These results indicate that poly(dA) at acidic pH forms a right-handed helical duplex with parallel-mannered chains, whereas the coralyne poly(dA) binding induces a stable antiparallel duplex. Furthermore, from dilution experiments, the author found that the parallel duplex formed at acidic pH is converted to S-form, which has the single-stranded structure with an intramolecular double-stranded region formed by intramolecular A:A base pairing, while the A-motif-coralyne assembly is dissociated into single strands under a certain concentration. Although the single-stranded structure with intramolecular double-stranded region in poly(A) sequences has been proposed continuously, there was no report that experimentally evidenced the existence of intramolecular duplex in A-motif. For the first time, the author successfully observed the existence of intramolecular double-stranded region in A-motif using various spectroscopic methods, including FCS and single-molecule spectroscopy. The result presented here suggests that there is a possibility of the existence of intramolecular duplex region in poly(A) tail in vivo, and this duplex region may affect the biological function of poly(A) tail.

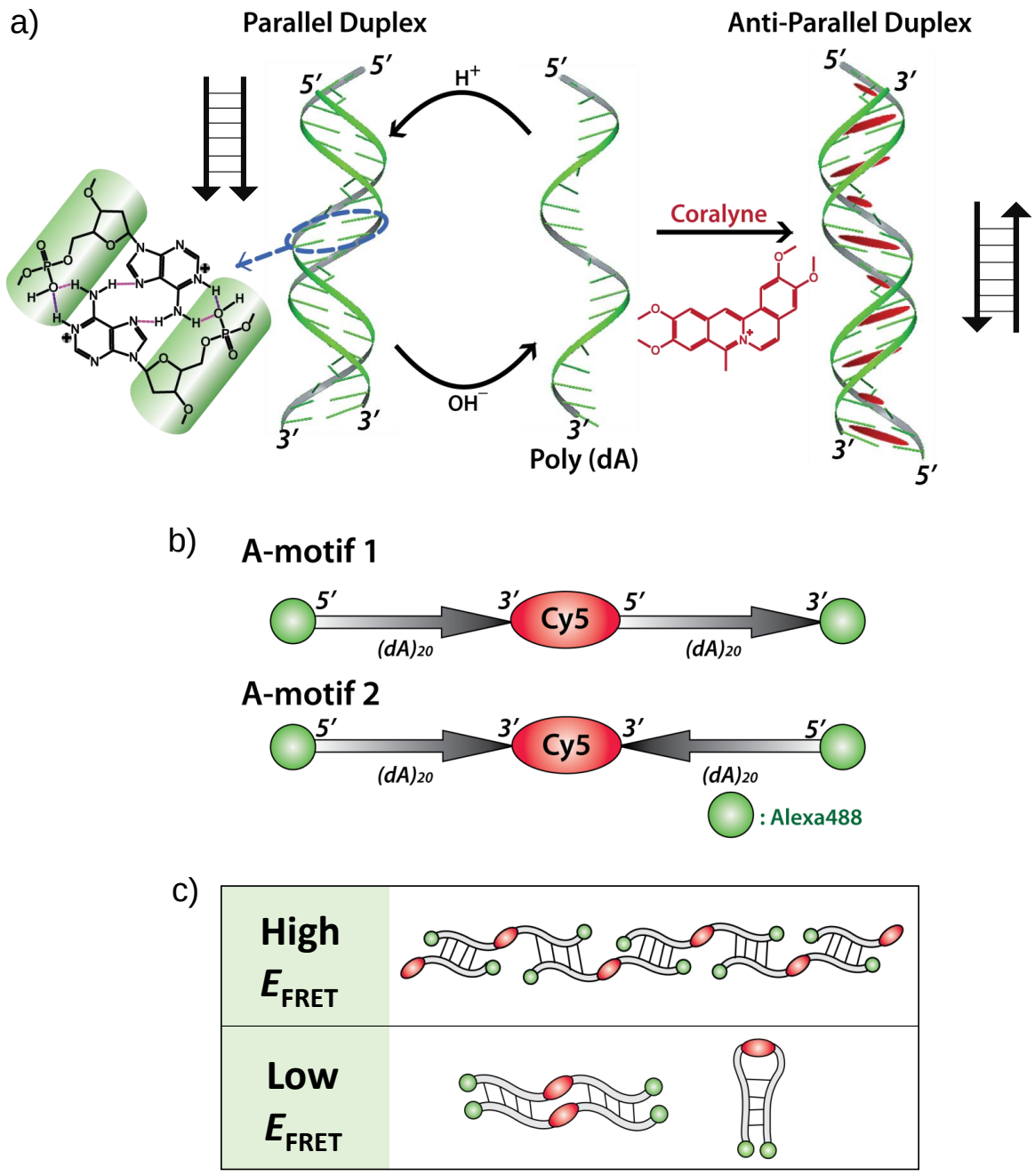


**Figure 2-1. (a)** Illustration of duplex formation of poly(dA) at acidic pH (left) and in the presence of coralyne molecule (right); and **(b)** schematic structures of **A-motif 1** and **2**. **(c)** Wire type, duplex type, and hairpin type of A-motif self-assemblies categorized by the expected $E_{FRET}$.

## Experimental Section

**Materials. A-motif 1** (Alexa488-5'-$(dA)_{20}$-3'-Cy5-5'-$(dA)_{20}$-3'-Alexa488) and **A-motif 2** (Alexa488-5'-$(dA)_{20}$-3'-Cy5-3'-$(dA)_{20}$-5'-Alexa488) were obtained from Japan Bio Service. The concentration of A-motif strand was determined by UV absorbance of Cy5 ($\varepsilon_{650}$ = 2.5 × $10^5$ $M^{-1}$ $cm^{-1}$).[29] Coralyne chloride was purchased from Sigma-Aldrich and used without further purification. The concentration of coralyne was determined by UV absorbance of coralyne ($\varepsilon_{420}$ = 14.5 × $10^3$ $M^{-1}$ $cm^{-1}$).[22] To prepare buffer solutions with a wide range of pH, 100 mM of $Na_2HPO_4$ and $NaH_2PO_4$ were used for pH 4.6-7.0, whereas $H_3PO_4$ and $NaH_2PO_4$ were used for pH 3.6-4.4. Fluorescence of Alexa488 and Cy5 is relatively pH-insensitive in the range of pH 3-8.[30,31]

**Steady-State Measurements.** The fluorescence and CD spectra were measured using a Horiba FluoroMax-4 and JASCO CD-J720, respectively.

**Atomic Force Microscopy (AFM).** AFM images were acquired with an atomic force microscope (SPA400-DFM, Seiko Instruments Inc.) in the dynamic force mode. A-motif 1 and 2 was dissolved in the pH 7.6 buffer solution containing 20 mM Tris, 20 mM NaCl, and 50 μM spermidine. The sample was placed on a freshly cleaved mica plate pre-treated with the pH 7.6 buffer solution containing 20 mM Tris, 20 mM NaCl, and 50 μM spermidine, and adsorbed for 5 min at room temperature. The plate was dried by air blowing.

**Single-Molecule Fluorescence Spectroscopy.** FCS experiments with various pH solutions were measured with a time-resolved fluorescence microscope using confocal optics (MicroTime 200; PicoQuant, Berlin-Adlershof, Germany). In the single-molecule FRET experiment, 1 nM A-motif solutions containing 10% $\beta$-Mercaptoethanol by volume and 1 mM Trolox were prepared. Trolox and $\beta$-mercaptoethanol are used to reduce photoblinking and photobleaching.[32] To observe fluorescence intensity trajectories (FITs) of freely diffusing single molecules, 60 μL of each sample was loaded into the microchamber made by a 1 in. glass coverslip and Secure-Seal (S24733, Invitrogen). FITs were measured with the same confocal optics (MicroTime 200; PicoQuant, Berlin-Adlershof, Germany) and two single photon avalanche photodiodes (Micro

Photon Devices, PDM 50CT and 100CT) for the simultaneous detection of the FRET donor and acceptor. All samples were excited through an oil objective (Olympus, UPlanSApo, 1.40 NA, 100×) with a 485 nm pulsed laser (Pico Quant, full width at half-maximum 120 ps) controlled by a PDL-800B driver (PicoQuant). The excitation power of about 65 μW was used. Bandpass filters (Olympus, BA510-550 and 690/70), and 75 μm pinhole were used for spatial filtering to reject out-of-focus signals. The data collected using the PicoHarp 300 TCSPC module (PicoQuant) were stored in the time-tagged time-resolved mode (TTTR), recording every detected photon with its individual timing, which were used for the singlemolecule analysis. Each FIT was taken for 1 min with a binning time of 1 ms. All of the experimental data were obtained at room temperature.

**Results and Discussions**

**pH Effect on A-Motif Formation.** Figure 2-2 shows the fluorescence spectra of **A-motif 1** and **2** as a function of pH. As shown in Figure 2-2, the fluorescence intensities of Alexa488 attached to **A-motif 1** and **2** are decreased by lowering pH. Especially, the fluorescence quenching of **A-motif 1** is much more dramatic than that of **A-motif 2**. Because the fluorescence intensity of Alexa488 is independent in the range of pH 4.0-10.0, the changes in the fluorescence intensities of A-motif with decreasing pH are closely related to the conformational change of A-motif. Interestingly, as shown in Figure 2-2c, **A-motif 1** shows an abrupt transition of apparent FRET efficiency ($E_{FRET} = I_A/(I_A + I_D)$) at about pH 4.0, whereas that of **A-motif 2** shows a constant value (~0.1). This discrepancy is probably due to the different conformation of the pH-induced self-assembly of **A-motif 1** and **2**, resulting in the distinct $E_{FRET}$. As mentioned above, poly(A) at acidic pH forms a right-handed helical duplex with parallel-mannered chains and tilted protonated bases. Considering the sequence of **A-motif 1** and **2**, which have different directions of phosphate backbone, **A-motif 1** at acidic pH can form the dimeric duplex or wire-type duplex, whereas **A-motif 2** can form the dimeric duplex or hairpin-type duplex. Among these structures, only wire-type duplex can induce a high $E_{FRET}$ ($\geq$ 0.3) due to the FRET from the donor to the acceptor because of close proximity. In light of these results, it is assumed that **A-motif 1** at acidic pH dominantly forms the wire-type duplex leading to a high $E_{FRET}$, whereas **A-motif 2**

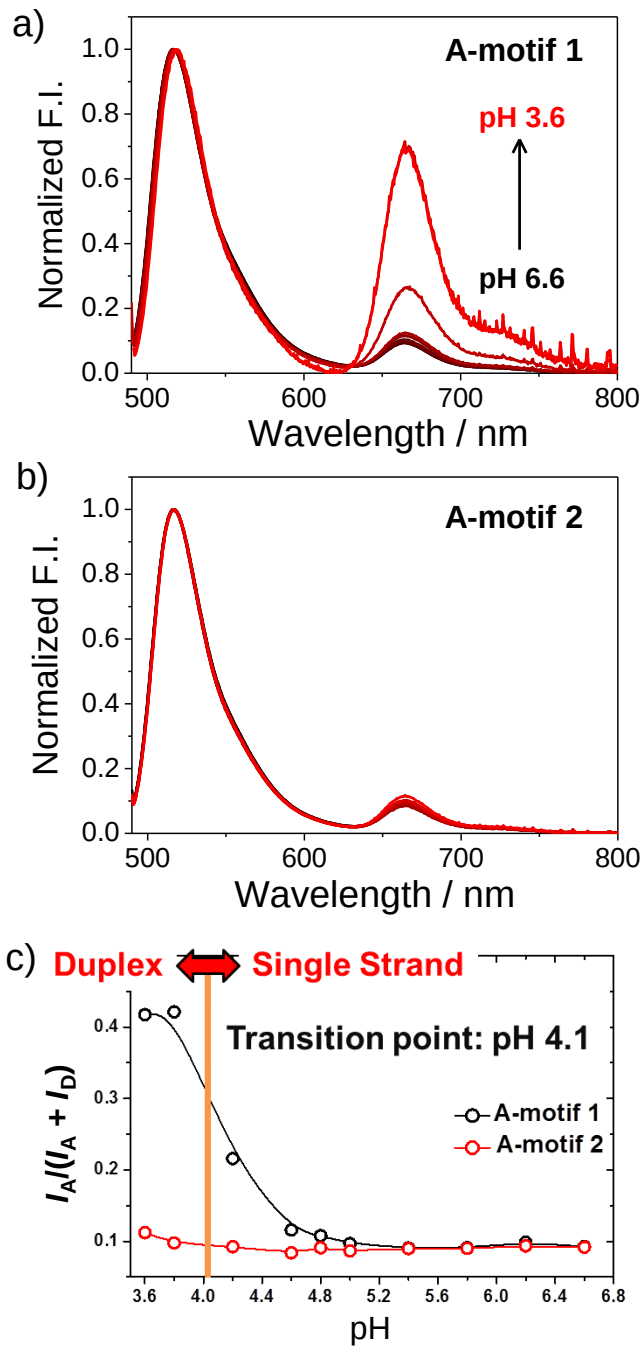


**Figure 2-2.** Fluorescence spectra of **(a) A-motif 1** and **(b) A-motif 2** in various pH solutions normalized at 518 nm. [ssDNA] = 100 nM, $\lambda_{ex}$ = 485 nm. **(c)** The ratio of the fluorescence intensities of acceptor to total emission ($I_A/(I_A + I_D)$) of **A-motif 1** (black) and **A-motif 2** (red) in various pH solutions.

forms the dimeric duplex or hairpin-type duplex. Here, it is noteworthy that the apparent $E_{FRET}$ of **A-motif 2** was not affected by DNA duplex formation even if the fluorescence intensities of the donor and acceptor of **A-motif 2** slightly decrease due to the π-π interaction between two dyes by the formation of a dimeric or hairpin-type duplex (Figures 2-2b and 2-2c). This means that the change of the apparent $E_{FRET}$ shown in this study is mainly attributed to changes of inter-dye distances.

**Intercalator Effect on A-Motif Formation.** The author also investigated the self-assembly of A-motif induced by coralyne binding at neutral pH (Figure 2-3). In contrast to the A-motif duplex induced by pH, the $E_{FRET}$ of **A-motif 2** was increased considerably by adding coralyne, whereas that of **A-motif 1** was decreased. As explained earlier, coralyne induces antiparallel duplex of poly(A) or poly(dA) by the intercalation into four adenine bases.[11,33] Considering the sequence of each nucleotide, **A-motif 2**-coralyne assembly at neutral pH has only a wire-type duplex resulting in a high $E_{FRET}$, whereas **A-motif 1** forms several structures such as a dimeric duplex or hairpin-type duplex. Therefore, the increase of the $E_{FRET}$ observed for **A-motif 2** indicates that **A-motif 2**-coralyne assembly at neutral pH has only a wire-type duplex structure. By contrast, **A-motif 1** forms a dimeric or hairpin-type duplex with coralyne. Additionally, using an AFM, the wire-type structures of **A-motif 1** and **2** induced by the acidic condition and coralyne molecule, respectively, could be observed (Figure 2-4). This result further supports that poly(dA) at acidic pH forms a right-handed helical duplex with parallel-mannered chains, whereas the binding of coralyne induces an antiparallel duplex.

Here, it is noteworthy that the parallel dimeric duplex formed at acidic pH does not affect the $E_{FRET}$ (**A-motif 2** in Figure 2-2c), whereas the antiparallel dimeric duplex formed with coralyne leads to the decrease of the $E_{FRET}$ from 0.1 to 0.03 (**A-motif 1** in Figure 2-3a). This result indicates that the intercalation of coralyne into the four adenine bases results in the elongation of the helical structure of poly(dA)-coralyne assembly (~1 nm). This result well agrees with the theoretical result of Joung et al. that the antiparallel duplex formed by coralyne binding has a rather extended and less twisted structure as compared to canonical B-DNA.[34]

**Concentration Effect on A-Motif Formation.** Concentration of the poly(A) is an important factor in the self-assembly of poly(dA) or poly(A). According to the previous study on the

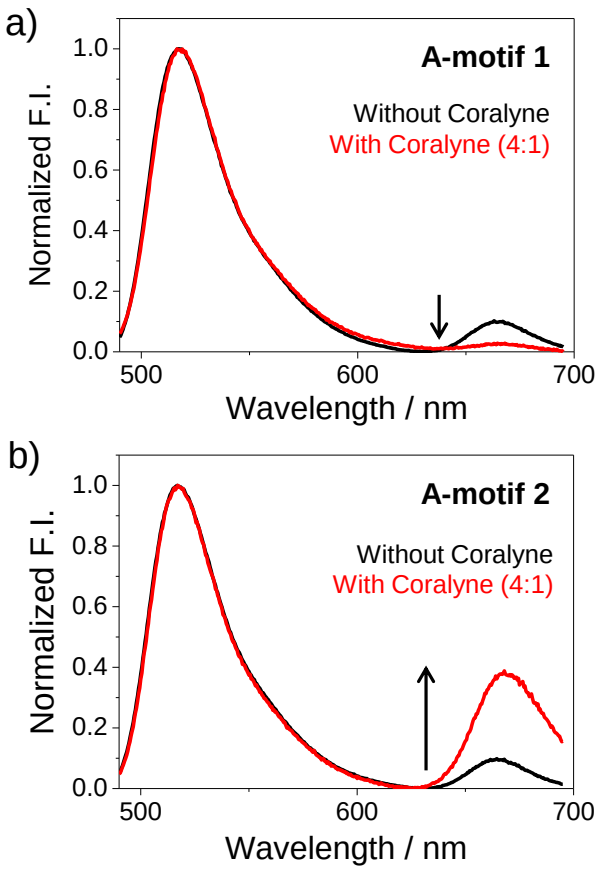


**Figure 2-3.** Fluorescence spectra of **(a) A-motif 1** and **(b) A-motif 2** in the absence (black) and presence (red) of coralyne normalized at 518 nm. [ssDNA] = 100 nM ([adenine] = 4 μM), [coralyne] = 1 μM, and $\lambda_{ex}$ = 485 nm. The direction of arrows represents the change in normalized fluorescence intensity of Cy5 upon adding coralyne.

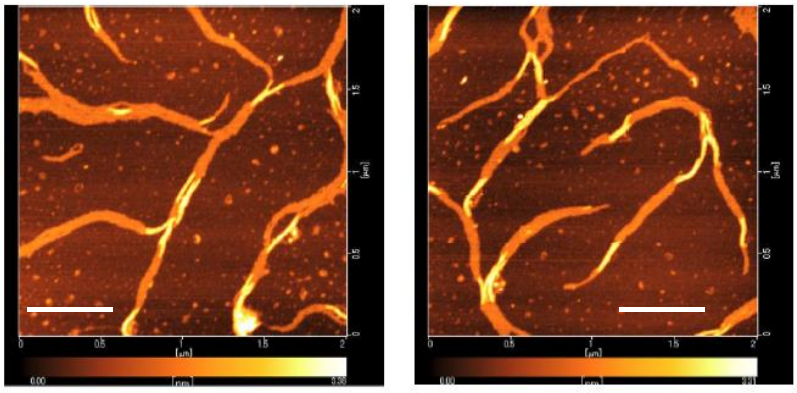

**Figure 2-4.** Representative AFM images of self-assembly of **A-motif 2** in the presence of coralyne at neutral pH. Scale bar: 500 nm.

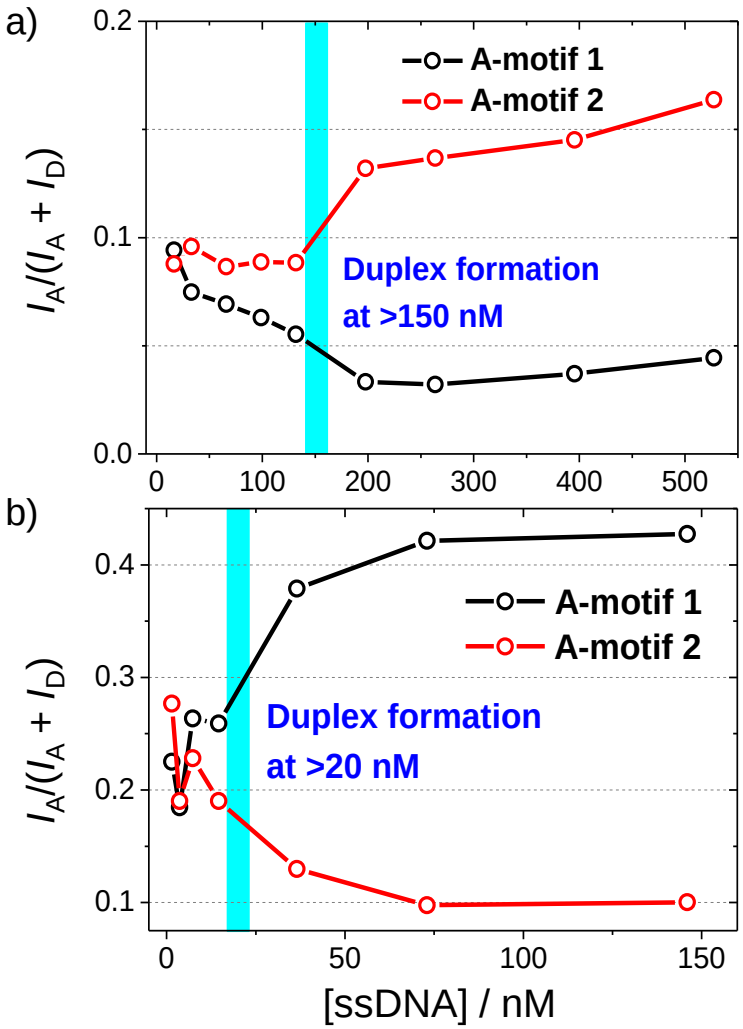


**Figure 2-5.** Changes in the ratio of the fluorescence intensities of acceptor to total emission ($I_A/(I_A + I_D)$) accompanied by the conformational changes of A-motif **(a)** in the presence of coralyne and **(b)** at pH 3.8 by the dilution. ssDNA stands for a single strand of 40-mer A-motif DNA. The molar ratio of [ssDNA] to [coralyne] in all samples is adjusted to be 4:1. Approximate transition regions are colored in blue.

dissociation of poly(A) duplex,[33] the poly(A)-coralyne assembly undergoes a sharp transition toward a single strand as a function of poly(A) and ligand concentration. In other words, the poly(A)-coralyne assembly begins to be dissociated into single strands under a certain critical concentration. Here, using the change in the $E_{FRET}$ accompanied by the dilution, the

concentration effect on the self-assembly of poly(dA) induced by pH and coralyne binding was further investigated. As shown in Figure 2-5a, the $E_{FRET}$ of **A-motif 2** (red), which forms a wire-type duplex in the presence of coralyne at neutral pH, is decreased from 0.17 to 0.1 as the sample is diluted from [ssDNA] = 527.4 to 16.5 nM, whereas that of **A-motif 1** (black) is increased from 0.03 to 0.1. In contrast to the result of A-motif-coralyne assembly, the $E_{FRET}$ of **A-motif 1**, which forms a wire-type duplex at acidic pH, is decreased from 0.45 to 0.2 as the sample is diluted from [ssDNA] = 146.0 to 1.5 nM, whereas that of **A-motif 2** is increased from 0.1 to 0.2 (Figure 2-5b). These results indicate that the self-assembly of poly(dA) formed by pH and coralyne binding is dissociated by the dilution. Furthermore, the parallel duplex formed at acidic pH begins to be dissociated at about [ssDNA] = 20 nM, whereas the antiparallel A-motif duplex formed with coralyne at neutral pH begins to be dissociated at about [ssDNA] = 150 nM. These results mean that the parallel duplex of A-motif formed at acidic pH is more stable than another induced by coralyne intercalation. The different transition concentrations (or critical concentration) can be explained by the distinct duplex structure. In the case of A-motif-coralyne assembly, the two single-stranded poly(dA)s and coralyne molecules with the ratio of one coralyne to four adenine molecules are incorporated in the duplex formation, depending on the concentration of single-stranded poly(dA) as well as coralyne. However, because the parallel duplex at acidic pH without coralyne is formed by A:A base-pairing due to the hydrogen bonds between two protonated adenine bases, the parallel duplex formation depends on the concentration of only single-stranded poly(dA). Thus, the parallel duplex formed at acidic pH is relatively less affected by the concentration of DNA.

Interestingly, **A-motif 1** and **2** at very low concentration (< 20 nM) and acidic pH showed the $E_{FRET}$ of 0.2, while **A-motif 1** and **2** in the presence of coralyne at the similar concentration and neutral pH showed the $E_{FRET}$ of 0.1. The $E_{FRET}$ of 0.1 observed in the presence of coralyne at nM concentration and neutral pH is close to those of single-stranded **A-motif 1** and **2** observed at neutral pH (Figure 2-2c). Thus, the observation of $E_{FRET}$ of 0.1 in the presence of coralyne under the dilueted condition implies that the A-motif-coralyne assembly is dissociated into the single-stranded structure by the dilution. This result is consistent with that reported by Hud and co-workers.[33] However, the $E_{FRET}$ of 0.2 observed at the similar concentrations and acidic pH is 2 times larger than those of single-stranded **A-motif 1** and **2** observed at neutral pH, indicating that

the parallel duplex formed at acidic pH and low concentration to induce complex dissociation was converted to a more compact conformation rather than an extended single-stranded structure.

**Shrunken Form of A-Motif Discovered by Single-Molecule FRET Measurements.** To confirm the existence of the alternative acidic conformation at extremely low concentration (< 20 nM), single-molecule FRET experiment was carried out. Single-molecule fluorescence spectroscopy provides an insight into the behavior of each individual molecule and consequently allows a detailed observation of subpopulations in structures and dynamics hidden under ensemble-averaged results.[35-38] Figure 2-6a displays the $E_{FRET}$ distributions determined from the FITs of single-molecule **A-motif 1** and **2** in the pH 3.8 solution. As depicted in Figure 2-6a, the $E_{FRET}$ distributions of **A-motif 1** and **2** at pH 3.8 show two distinct peaks (0.07 and 0.20), whereas the $E_{FRET}$ histogram observed at pH 7.0 shows a single $E_{FRET}$ peak centered at almost zero (~0.03). Considering the experimental error, $E_{FRET} \approx 0.03$ and 0.07 determined at pH 3.8 and 7.0 may be attributed to the same structural species. Because **A-motif 1** and **2** have a single-stranded structure at neural pH as shown in Figure 2-2c, the lower $E_{FRET}$ observed at pH 3.8 and 7.0 ($E_{FRET} \approx 0.07$) comes from the single-stranded structures of **A-motif 1** and **2**. On the other hand, the $E_{FRET}$ of ~0.2 observed at pH 3.8 was close to those ($E_{FRET} \approx 0.20$) of **A-motif 1** and **2** determined from the dilution experiments. This result supports that the parallel duplex formed at acidic pH was converted to the alternative acidic conformation rather than an extended single-stranded structure. The $r$ (inter-dye distance) for the structural species with $E_{FRET} \approx 0.2$ are calculated to be 6.6 nm. This value is shorter than that of single-stranded **A-motif 1** and **2** ($r \approx$ 7.4 nm), indicating that the structural species with $E_{FRET} \approx 0.2$ at nM concentration has a more compact conformation as compared to the single-stranded structure. Here, the new species observed at this concentration and acidic pH was named "S-form" because this species exhibits a shrunken structure as compared to the extended single-stranded structure of poly(dA).

Moreover, the author anticipates the individual conformations of the S-form of **A-motif 1** and **2** observed at nM concentration and acidic pH. Several studies on the pH dependent conformational transition of poly(A) proposed that there are three different acidic conformations of poly(A) depending on the extent of protonation of the molecule: A-form, B-form, and frozen form.[17-21] As pH is lowered from neutral pH, B-form appears at the pH just below the pKa of N(1) atom of adenine and is stabilized by the partial protonation of adenine bases. When pH is

further decreased, A-form is formed, which is tightly packed with fully protonated A:A bases. Another acidic form is a frozen form, which is observed only below about pH 4.0. The conformation of frozen form can be described as a grid-like aggregate consisting of alternating, variably sized, single-stranded regions linked with a double-stranded region. Thus, S-form, observed at pH 3.8 in this study, may be compared to frozen form, which has a disordered grid-like aggregated structure below pH 3.8. However, because frozen form (i.e. a kind of poly(A) aggregate with a gridlike structure) exists only at high concentration and its formation is prevented by the dialysis, the S-form, which is observed only at extremely low concentration (< 20 nM) in this study, is not a kind of assembly such as a duplex or aggregate. In other words, this means that the S-form observed in this study is not a frozen form, which is made of many poly(A) molecules. In light of these results, the author proposes that S-form observed at acidic pH and nM concentration may have a partial intramolecular double-stranded region. As the concentration of A-motif at acidic pH is lowered, the molar ratio of proton against A-motif is significantly increased. Therefore, the single-stranded DNA formed by dilution greatly interacts with proton, leading to the double-stranded regions formed by intramolecular A:A base pairing.

**Characterization of S-Form by FCS Measurements.** If the structure of A-motif at acidic pH and nM concentration has an intramolecular double-stranded region, its hydrodynamic radius should be shorter than that of the single-stranded structure. To further confirm the existence of intramolecular double-stranded regions in A-motif, the change in the hydrodynamic radius of **A-motif 1** and **2** was measured by FCS. FCS is a very valuable tool to observe the hydrodynamic radius from the translational diffusion of a biomolecule.[30,38,39] In FCS, autocorrelation function ($G(\tau)$) for diffusion in three dimensions can be expressed by

$$G(\tau) = \frac{1}{N}\left(1 + \frac{\tau}{\tau_{\text{diff}}}\right)^{-1}\left(1 + \left(\frac{s}{u}\right)^2 \frac{\tau}{\tau_{\text{diff}}}\right)^{-1/2} \qquad (1)$$

where $N$ is the average number of molecules in the observed volume, $\tau_{\text{diff}}$ is the molecular diffusion time, $s$ is the radius of the measurement area, and $u$ is one-half of its axial length. Figure 2-6b shows FCS curves of **A-motif 1** and **2** recorded at pH 3.8 and 7.0. From the quantitative analysis of FCS curves with eq 1, $\tau_{\text{diff}}$ of **A-motif 1** and **2** at pH 7.0 are determined to be 2.28 ± 0.18 and 2.35 ± 0.18 ms, respectively. This result means that the conformation of **A-motif 1** is very similar to that of **A-motif 2** at neutral pH. However, $\tau_{\text{diff}}$ of **A-motif 1** and **2** at pH

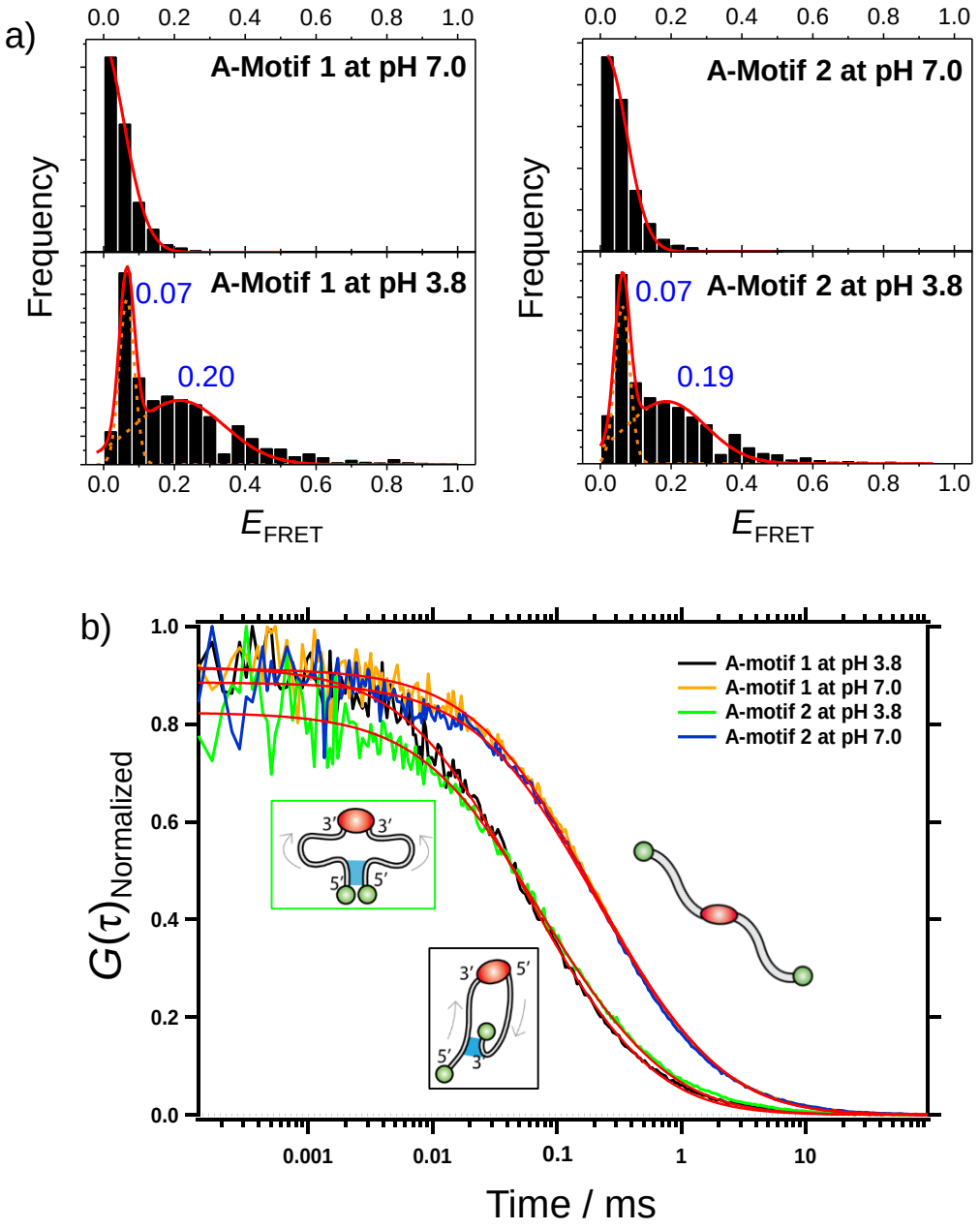


**Figure 2-6. (a)** $E_{FRET}$ distribution of **A-motif 1** and **2** at pH 7.0 and 3.8 obtained by single-molecule FRET measurements. **(b)** FCS curves of A-motif at pH 3.8 (black, **A-motif 1**; green, **A-motif 2**) and 7.0 (yellow, **A-motif 1**; blue, **A-motif 2**) and their fitting results (red). Expected structures of S-form of A-motif 1 and 2 are illustrated in a black and green box, respectively.

3.8 are 0.63 ± 0.05 and 0.86 ± 0.07 ms, respectively, which are 34 times faster than those determined at pH 7.0. Because the $\tau_{diff}$ is propotional to the hydrodynamic radius of a molecule, the faster $\tau_{diff}$ indicate that the hydrodynamic radii of the conformations of **A-motif 1** and **2** observed at pH 3.8 are 34 times smaller than that of the single-stranded structure at neutral pH. This result supports that S-form of **A-motif 1** and **2** at acidic pH and nM concentration may have the single-stranded structure with partial intramolecular double-stranded regions formed by intramolecular A:A base pairing rather than the extended single-stranded structure. In addition, concerning the directions of phosphate backbone of **A-motif 1** and **2**, they may have different hypothetic single-stranded structures as depicted in Figure 2-7.

**Conclusion**

In this study, the two different adenine oligomers labeled with FRET donor and acceptor dye (Figure 2-1b) were designed and comprehensively investigated the duplex formation by pH change and coralyne binding. Results presented here show that **A-motif 1** forms the wire-type duplex at acidic pH, whereas **A-motif 2** becomes the wire-type duplex by the binding of coralyne at neutral pH, supporting that poly(dA) at acidic pH forms a right-handed helical duplex with parallel-mannered chains, whereas the intercalation of coralyne into poly(dA) induces a stable antiparallel duplex. Furthermore, the author experimentally proved that the antiparallel duplex formed by coralyne binding has a rather extended and less twisted structure as compared to parallel duplex formed at acidic pH.

Upon decreasing the concentration of poly(dA), the parallel duplex formed at acidic pH is converted to S-form, which has the single-stranded structure with intramolecular double-stranded regions formed by A:A base pairing, while the A-motif coralyne assembly begins to be dissociated into the single-stranded structure. Although the existence of intramolecular double-stranded regions in poly(A) sequence has been proposed,[20,40] there has been no report that experimentally evidenced the presence of such structures. Here, the author successfully proved the existence of intramolecular double-stranded regions in A-motif using various spectroscopic methods, including FCS and single-molecule FRET technique. The result presented here suggests that there is a possibility of the existence of intramolecular duplex region in poly(A) tail in vivo, and this duplex region may affect the biological function of poly(A) tail as suggested by

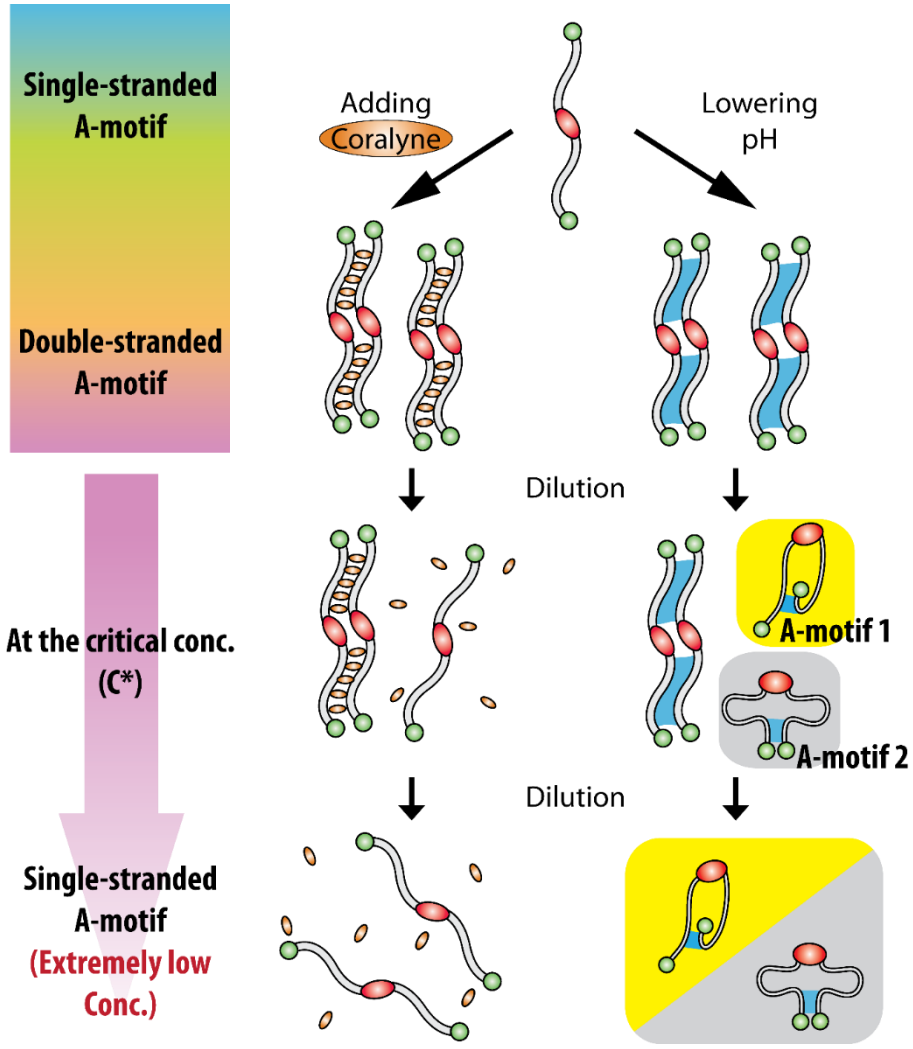


**Figure 2-7.** Representative formation and dissociation processes of A-motif induced by coralyne molecule (orange) and acidic pH (< pH 4.0). Sky blue region represents A:A base pairing region under an acidic condition. Two distinct conformations of **A-motif 1** and **2** at nM concentration under an acidic condition are depicted in yellow and gray boxes, respectively.

Zarudnaya et al.[20] In addition, this finding is extremely valuable for the nanotechnology that exploits poly(A) or poly(dA) as building blocks because the formation of S-form suggested in this study may affect an overall structure and working efficiency in nanomachine or DNA architecture.

## References


(1) Bacolla, A.; Wells, R. D. *Mol. Carcinog.* **2009**, *48*, 273.
(2) Wang, G.; Vasquez, K. M. *Mutat. Res.* **2006**, *598*, 103.
(3) Choi, J.; Majima, T. *Chem. Soc. Rev.* **2011**, *40*, 5893.
(4) Wang, C.; Huang, Z.; Lin, Y.; Ren, J.; Qu, X. *Adv. Mater.* **2010**, *22*, 2792.
(5) Modi, S.; M, G. S.; Goswami, D.; Gupta, G. D.; Mayor, S.; Krishnan, Y. *Nat. Nanotechnol.* **2009**, *4*, 325.
(6) Saha, S.; Bhatia, D.; Krishnan, Y. *Small* **2010**, *6*, 1288.
(7) Bhatia, D.; Sharma, S.; Krishnan, Y. *Curr. Opin. Biotechnol.* **2011**, *22*, 475.
(8) Fahlman, R. P.; Hsing, M.; Sporer-Tuhten, C. S.; Sen, D. *Nano Lett.* **2003**, *3*, 1073.
(9) Chakraborty, S.; Sharma, S.; Maiti, P. K.; Krishnan, Y. *Nucleic Acids Res.* **2009**, *37*, 2810.
(10) Rich, A.; Davies, D. R.; Crick, F. H.; Watson, J. D. *J. Mol. Biol.* **1961**, *3*, 71.
(11) Persil, O.; Santai, C. T.; Jain, S. S.; Hud, N. V. *J. Am. Chem. Soc.* **2004**, *126*, 8644.
(12) Chowdhury, S. R.; Islam, M. M.; Kumar, G. S. *Mol. BioSyst.* **2010**, *6*, 1265.
(13) Song, G.; Ren, J. *Chem. Commun.* **2010**, *46*, 7283.
(14) Giri, P.; Suresh Kumar, G. *Mol. BioSyst.* **2010**, *6*, 81.
(15) Xi, H.; Gray, D.; Kumar, S.; Arya, D. P. *FEBS Lett.* **2009**, *583*, 2269.
(16) Alberts, B. *Molecular Biology of the Cell*, 5th ed.; Garland Science: New York, 2008.
(17) Janik, B.; Sommer, R. G.; Bobst, A. M. *Biochim. Biophys. Acta* **1972**, *281*, 152.
(18) Petrovic, A. G.; Polavarapu, P. L. *J. Phys. Chem. B* **2005**, *109*, 23698.
(19) Finch, J. T.; Klug, A. *J. Mol. Biol.* **1969**, *46*, 597.
(20) Zarudnaya, M. I.; Hovorun, D. M. *IUBMB Life* **1999**, *48*, 581.
(21) Maggini, R.; Secco; Venturini, M.; Diebler, H. *J. Chem. Soc., Faraday Trans.* **1994**, *90*, 2359.
(22) Xing, F.; Song, G.; Ren, J.; Chaires, J. B.; Qu, X. *FEBS Lett.* **2005**, *579*, 5035.
(23) Gough, A. N.; Jones, R. L.; Wilson, W. D. *J. Med. Chem.* **1979**, *22*, 1551.
(24) Maiti, M.; Kumar, G. S. *J. Nucleic Acids* **2010**, *2010*, 593408.
(25) Bhadra, K.; Kumar, G. S. *Biochim. Biophys. Acta* **2011**, *1810*, 485.
(26) Lv, Z.; Wei, H.; Li, B.; Wang, E. *Analyst* **2009**, *134*, 1647.
(27) Xu, X.; Wang, J.; Yang, F.; Jiao, K.; Yang, X. *Small* **2009**, *5*, 2669.
(28) Zhao, C.; Peng, Y.; Song, Y.; Ren, J.; Qu, X. *Small* **2008**, *4*, 656.
(29) Mansoor, S. E.; DeWitt, M. A.; Farrens, D. L. *Biochemistry* **2010**, *49*, 9722.
(30) Choi, J.; Kim, S.; Tachikawa, T.; Fujitsuka, M.; Majima, T. *J. Am. Chem. Soc.* **2011**, *133*, 16146.
(31) Tumpane, J.; Kumar, R.; Lundberg, E. P.; Sandin, P.; Gale, N.; Nandhakumar, I. S.; Albinsson, B.; Lincoln, P.; Wilhelmsson, L. M.; Brown, T.; Norden, B. *Nano Lett.* **2007**, *7*, 3832.
(32) Rasnik, I.; McKinney, S. A.; Ha, T. *Nat. Methods* **2006**, *3*, 891.
(33) Cetinkol, O. P.; Hud, N. V. *Nucleic Acids Res.* **2009**, *37*, 611.
(34) Joung, I. S.; Persil Cetinkol, O.; Hud, N. V.; Cheatham, T. E., III. *Nucleic Acids Res.* **2009**, *37*, 7715.

(35) Roy, R.; Hohng, S.; Ha, T. *Nat. Methods* **2008**, *5*, 507.
(36) Liu, R.; Hu, D.; Tan, X.; Lu, H. P. *J. Am. Chem. Soc.* **2006**, *128*, 10034.
(37) Tan, X.; Nalbant, P.; Toutchkine, A.; Hu, D. H.; Vorpagel, E. R.; Hahn, K. M.; Lu, H. P. *J. Phys. Chem. B* **2004**, *108*, 737.
(38) Choi, J.; Kim, S.; Tachikawa, T.; Fujitsuka, M.; Majima, T. *Phys. Chem. Chem. Phys.* **2011**, *13*, 5651.
(39) Neuweiler, H.; Johnson, C. M.; Fersht, A. R. *Proc. Natl. Acad. Sci. U.S.A.* **2009**, *106*, 18569.
(40) Smith, B. L.; Gallie, D. R.; Le, H.; Hansma, P. K. *J. Struct. Biol.* **1997**, *119*, 109.

# Part 2: Singlet Oxygen Detection Ex Vivo and in Living Cell using Fluorescence Probes

## Background

### Singlet Oxygen and Photodynamic Therapy

Among various reactive oxygen species, singlet oxygen ($^1O_2$) has been in a particular interest due to its distinct photo-physical properties and cytotoxic effect. Under photoirradiation of photosensitizer (Sens), nearby molecular oxygen can quench Sens in the excited state through electron transfer or energy transfer. The former results in the formation of oxygen radical species, for example, superoxide anion ($O_2^{\bullet -}$), whereas the latter produces $^1O_2$ through triplet-triplet intermolecular energy transfer. $^1O_2$ deactivates back to molecular oxygen in the triplet state with phosphorescence at 1275 nm. In the presence of adjacent molecules to oxidize, $^1O_2$ can participate various oxidation reactions such as Diels-Alder cycloaddition reaction to the center ring of anthracene.

One representative example to exploit the oxidative power of $^1O_2$ is photodynamic therapy (PDT). PDT can be defined as the administration of a nontoxic drug or Sens to a patient bearing a lesion, followed by photoirradiation of the lesion with visible light in the presence of oxygen.[1] There have been several PDT drugs proven by FDA, such as Photofrin for cancer treatment and Levulan Kerastick (i.e. aminolevulinic acid HCl) for precancerous skin lesions.[1] In this method, adequately populated Sens in tumor tissue destroys nearby cells under photoirradiation through complex cytotoxic pathways, for example, shutdown of microvessels, induction of cancer cell necrosis and apoptosis, and inflammation response. From chemist's point of view, all of these complex cell-killing mechanisms are triggered by the initial oxidative reaction of $^1O_2$. In order to improve the efficiency of PDT, therefore, understanding the intracellular dynamics of $^1O_2$ is undoubtedly crucial.

(1) *Advances in Photodynamic Therapy: Basic, Translational, and Clinical*; Hamblin, M. R., Mróz, P., Eds.; Artech House Engineering in Medicine & Biology Series; Artech House: Boston, 2008.

# Chapter 3. Photochemistry of Single Oxygen Sensor Green

## Introduction

Singlet oxygen ($^1O_2$), one of the reactive oxygen species (ROS), has gained substantial attention in biology, medicine, material, and chemistry.[1−4] It can be produced by cellular metabolism, redox reactions, photosensitization, etc. Since $^1O_2$ acts as a strong oxidation reagent, there are various intracellular enzymes and antioxidant mechanisms to deactivate $^1O_2$.[3,4] Thus, in normal cells, the naturally produced $^1O_2$ as well as other ROS do not cause significant damage for the intracellular organelles. At the same time, $^1O_2$ is a key component in photodynamic therapy (PDT), which is one of the emerging anticancer therapies.[5−7] Specifically, photosensitizers (Sens) used in PDT have high intersystem crossing quantum yields ($\Phi_{ISC}$; $\Phi_{ISC}$ of protoporphyrin IX is higher than 0.54), and Sens in the triplet excited state ($^3$Sens*) produces $^1O_2$ via the triplet−triplet energy transfer to molecular oxygen in the ground state (triplet oxygen, $^3O_2$). $^1O_2$ oxidizes nearby intracellular organelles and causes dysfunction of various intracellular cycles and cell death.[8]

Concerning the biological and medical importance of $^1O_2$, the development of the detection method and sensor materials for $^1O_2$ is undoubtedly an urgent and crucial subject.[2,5−7,9−13] The simplest and most direct method to monitor $^1O_2$ is the measurement of its phosphorescence in the near-IR region.[1,6,7] However, this method requires specialized instruments, since $^1O_2$ phosphorescence is observed with the lower quantum yield in the near IR region. Several indirect methods for $^1O_2$ detection have been developed, for example, fluorescence fluctuation of carbon nanotube,[10] the formation of endoperoxide (EP) inside of the chromophore,[9,13] bond breakage by the reaction with $^1O_2$,[12,14] etc.

Among them, Tanaka et al. developed the fluorescein (Fl)-based dyads as the $^1O_2$ probe molecules involving intramolecular photoinduced electron transfer (PET).[11] The dyads are composed of electron donor (anthracene derivative) and acceptor (Fl derivative) moieties, and Fl is covalently linked to the anthracene moiety (An), as shown in Figure 3-1. Since the highest occupied molecular orbital (HOMO) energy of Fl is lower than that of An (Table 3-1), intramolecular PET quenching of Fl in the singlet excited state ($^1$Fl*) by An occurs to give the

charge separated state involving one-electron reduced Fl (**R**) and An radical cation ($An^{\bullet+}$). In their subsequent study, the intramolecular PET of the dyads was further proved by the Rehm−Weller equation.[15] In the presence of $^1O_2$, however, An readily reacts with $^1O_2$ to form EP of the center ring of An. Since EP has a lower HOMO energy than that of Fl (Table 3-1), the intramolecular PET quenching of $^1Fl^*$ by EP does not occur at all. Then, $^1Fl^*$ deactivates with fluorescence (Figure 3-1).

In 2004, Invitrogen/Molecular Probes introduced a commercially available fluorescent sensor for $^1O_2$, named Singlet Oxygen Sensor Green (SOSG), and it has been actively exploited in a variety of fields such as material science, biochemistry, and medical application.[16−22] Concerning its absorption and fluorescence spectra and the previous reports on SOSG,[23,24] it is almost certain that SOSG is composed of Fl and An, which is similar to the structure proposed by Tanaka et al. (Figure 3-1).[11] Even though SOSG has been widely and frequently used due to its sensitivity and selectivity to $^1O_2$, good turn on/off contrast, and water solubility, only little is known for the photodynamic properties with the quantitative characterization. Moreover, a couple of recent studies have reported that SOSG can generate $^1O_2$ by irradiation of ultraviolet (UV) and visible light.[23,24] This is indeed a critical issue as a fluorescent sensor material because it produces the target molecule by itself during the irradiation. Nonetheless, there has been no discussion of the detailed mechanism for the formation of $^1O_2$. Which moiety and which excited state of SOSG indeed play a role in the formation of $^1O_2$?

In this report, the author have fully characterized the excitation wavelength ($\lambda_{ex}$) dependent photochemical properties of SOSG in the ground and excited states and furthermore elucidated the mechanism of $^1O_2$ generation caused by SOSG under irradiation of UV and visible light. Briefly, the irradiation of visible light (at 500 or 532 nm), which is often selected as an excitation wavelength in practice, allowed the intramolecular PET, followed by charge recombination, resulting in efficient fluorescence quenching. Moreover, the intersystem crossing of $^1Fl^*$ to form Fl in the triplet excited state generates $^1O_2$ from the triplet−triplet energy transfer. Subsequently, the 355 nm excitation with high intensity (>10 mJ $cm^{-2}$) induced the long-lived one-electron oxidized Fl (**X**) (i.e., a few ms) via two-photon ionization. In Chapter 3, SOSG with and without EP are denoted as Fl-EP and Fl-An, respectively.

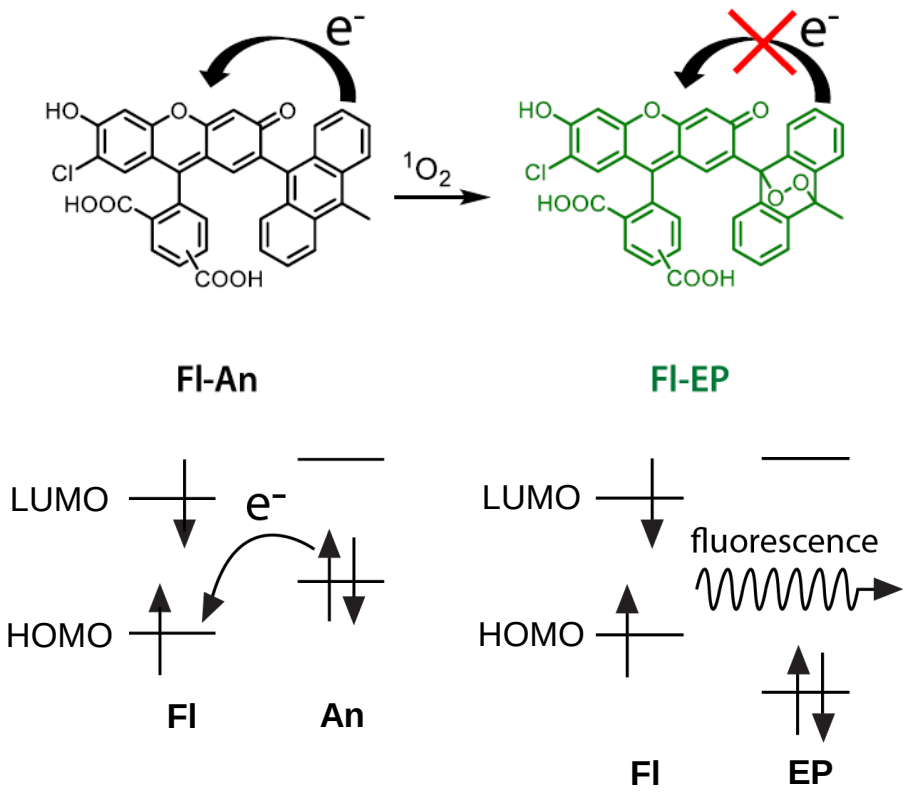


**Figure 3-1.** Expected chemical structures of Fl-An and Fl-EP and Fl fluorescence quenching by An via the intramolecular PET.

**Table 3-1.** HOMO and LUMO Energy Levels of Moieties in Fl-An and Fl-EP Calculated by Semiempirical PM3.[†]

| moieties | HOMO / kJ mol$^{-1}$ | LUMO / kJ mol$^{-1}$ |
|---|---|---|
| Fl | -837.44 | -157.88 |
| An | -773.37 | -99.99 |
| EP | -925.34 | -10.04 |

[†]Using Spartan '08, HOMO and LUMO energies of Fl, An, and EP were calculated for the xanthene moiety (Xa) with the substitution of chlorine and methyl group, 9,10-dimethylanthracene (DMA), and DMA with EP, respectively.

## Experimental Section

**Materials.** Singlet Oxygen Sensor Green® (Fl-An, Invitrogen/Molecular Probes®), 5(6)-carboxy-2',7'-dichlorofluorescein (Fl-Cl, 21882, Sigma), 5(6)-carboxyfluorescein (21877, Sigma), 9,10-dimethylanthracene (DMA, D146706, Aldrich), and α,β,γ,δ-tetrakis(1-methylpyridinium-4-yl)porphyrin (TMPyP4, A5014, TCI) were used without further purification. Endoperoxide form of Fl-An (Fl-EP) was prepared either by continuous irradiation of Fl-An or chemical method that used $Na_2MoO_4 \cdot 2H_2O$ (198-02471, WAKO) and $H_2O_2$ (086-07445, WAKO). Using either a 50 mW $cm^{-2}$ Hg lamp (REX-250, Asahi Spectra) with a bandpass filter (BP420-440, Olympus) or 100 mW $cm^{-2}$ Xe lamp (LAX-C100, Asahi Spectra) with a bandpass filter (BA510-550, Olympus), 2 mL of Fl-An solution was irradiated in the wavelength range of 420–440 or 510–550 nm, respectively, with a magnetic stirring.

Optical properties of fluorescein derivatives, including Fl-An and Fl-Cl, are known to be sensitive to pH because its conjugation and energy level become differed by (de)protonation of xanthene moiety or forming a transparent lactone form. Therefore, an aqueous buffer with pH 8.0 was chosen in order to maintain Fl-An and Fl-Cl as a trianionic form. Throughout this study except nanosecond laser flash photolysis, the author used pH 8.0 Tris-$K^+$ buffer prepared with 200 mM KCl, 4 mM $MgCl_2$, and 28 mM Tris-HCl. HCl and NaOH solution were added to adjust pH.

**Steady-State Measurements.** Ground-state absorption and fluorescence spectra of Fl-An, Fl-Cl, etc., were measured using a Shimadzu UV-3100PC and Horiba FluoroMax-4, respectively.

**Measurement of $\tau_{fl}$ and Fluorescence Quantum Yield ($\Phi_{fl}$).** $\tau_{fl}$ of Fl-An and Fl-Cl was measured using a time-resolved fluorescence microscope with confocal optics (MicroTime 200; PicoQuant, Berlin-Adlershof, Germany). In order to measure $\tau_{fl}$, 70 μL of Fl-An and Fl-Cl solution in pH 8.0 Tris-$K^+$ buffer was loaded into the micro-chamber made by a 1-inch glass cover slip and Secure-Seal (S24733, Invitrogen). The samples were excited through an oil objective (Olympus, UAPON 150XOTIRF; 1.45 NA, 150x) with a 485-nm pulsed laser (PicoQuant, full width at half-maximum 120 ps) controlled by a PDL-800B driver (PicoQuant). The excitation power of ~0.15 μW was used. The emission was collected with the same objective

and detected by a single photon avalanche photodiode (Micro Photon Devices, PDM 50CT and 100CT) through a 75-μm pinhole for spatial filtering to reject out-of-focus signals. The data collected using the PicoHarp 300 TCSPC module (PicoQuant) were stored in the time-tagged time-resolved mode (TTTR), recording every detected photon with its individual timing.

To determine $\Phi_{fl}$ of Fl-An and Fl-EP, 5(6)-carboxyfluorescein ($\Phi_{fl}$ = 0.92) was used as a reference. For the preparation of Fl-EP for $\Phi_{fl}$ determination, a chemical method to generate $^1O_2$ was chosen because the direct irradiation of Fl-An causes the irreversible photobleaching of Fl, leading to the lower $\Phi_{fl}$ than the actual value. In order to decrease the error and prevent from intermolecular interactions, the dye samples were prepared with absorbance of 0.005, 0.01, and 0.015 at 465 nm. Next, the integrated areas of fluorescence spectrum of the samples were calculated and linearly fitted against corresponding absorbance. Finally, $\Phi_{fl}$ was determined by comparing the slope of the linear plot with that for 5(6)-carboxyfluorescein.

**Measurement of Femtosecond Laser Flash Photolysis (fs-LFP).** The sub-ps transient absorption spectra were measured by the pump and probe method using a regenerative amplified titanium sapphire laser (Spectra Physics, Spitfire Pro F, 1 kHz) pumped by a Nd:YLF laser (Spectra Physics, Empower 15) for each dyes dissolved by pH 8.0 Tris-$K^+$ buffer. The samples of Fl-An and Fl-Cl were prepared at the concentration where they have the same absorbance, approximately 1.5 with 2.0 mm pathlength ([Fl-An] = 120 μM and [Fl-Cl] = 108 μM). An excitation pulse at 500 nm was generated by optical parametric amplifier (Spectra Physics, OPA-800CF). A white continuum pulse, which was generated by focusing the residual of the fundamental light to a sapphire plate after a computer controlled optical delay, was divided into two parts and used as the probe and the reference lights, of which the latter was used to compensate the laser fluctuation. Both probe and reference lights were directed to a rotating sample cell with 1.0 mm of optical path and were detected with a charge-coupled device detector equipped with a polychromator (Solar, MS3504). The pump pulse was chopped by a mechanical chopper synchronized to one-half of the laser repetition rate, resulting in a pair of the spectra with and without the pump, from which an absorption change induced by the pump pulse was estimated.

**Measurement of Nanosecond Laser Flash Photolysis (ns-LFP).** The nanosecond transient

absorption spectra were measured by the pump and probe method using the third-harmonic oscillation (355 nm, fwhm of 4 ns) and second harmonic oscillation (532 nm, fwhm of 4 ns) from a Q-switched Nd:YAG laser (Continuum, Surelite II-10) as the excitation sources. The light from a xenon flash lamp (Osram, XBO-450) was focused into the sample solution for the transient absorption measurement. Time profiles of the transient absorption in the UV−Vis region were measured with a monochromator (Nikon, G250) equipped with a photomultiplier (Hamamatsu Photonics, R928) and digital oscilloscope (Tektronics, DPO 3054). Each decay profile was collected after averaging 16 and 64 times for the 355- and 532-nm excitation, respectively.

During the ns-LFP measurements, it should be noted that 45 volume% (vol%) of acetonitrile (ACN) mixed pH 8.0 Tris-$K^+$ buffer was used because the absorption of Fl-An at 532 nm in pH 8.0 buffer was too small to obtain acceptable transient absorption signal for the 532-nm excitation. In the ACN mixed buffer, approximately 5 nm red-shift occurred in Fl-An, resulting in approximately twice increase in absorbance at 532 nm. Meanwhile, the absorption spectral shape of Fl-An in the ground state did not change, which indicated that the trianionic form of Fl was well maintained.

In addition, 355-nm excitation caused significant photodecomposition of dyes during the repetitive scanning. Due to the photo-instability of Fl-An under the 355-nm excitation, it was impossible to obtain the whole transient absorption spectrum with good signal-to-noise ratio. Instead, only decay profiles at the peak position of the transient absorption (430 nm) were measured with 16 averaging times for the 355-nm excitation as shown in Figure 5a. On the other hand, in the case of transient absorption spectrum of Fl-Cl (Figure 4b), most of the photons were absorbed by anthracene molecules, triplet sensitizers. Accordingly, photodecomposition of Fl-Cl by direct excitation was largely prevented.

**Time-Resolved Phosphorescence Measurement.** The samples of Fl-An, Fl-EP, and TMPyP4 were prepared in pH 8.0 Tris-$K^+$ buffer in a 1 × 1 × 4 $cm^3$ quartz cell ([Fl-An] = 43.9 μM, [Fl-EP] ≈ 43.9 μM and [TMPyP4] = 28.7 μM). The third-harmonic oscillation (355 nm, fwhm of 4 ns, 18 mJ $pulse^{-1}$) and second-harmonic oscillation (532 nm, fwhm of 4 ns, 6–6.5 mJ $pulse^{-1}$) from a Q-switched Nd:YAG laser (Continuum, Surelite II-10) were used for the excitation light. The photoinduced luminescence from the sample cell was collected with quartz lenses, passed

through a monochromator, and then introduced into a near IR photomultiplier tube module (Hamamatsu Photonics, H10330A-75). After amplified by 350 MHz amplifier unit (Stanford Research, SR445A), the output of the photomultiplier was sent to a gated photon counter (Stanford Research, SR400) under direct control from a PC via GPIB interface. To measure the lifetime of $^1O_2$, the signal was accumulated (5 repetitions) by changing the delay time from 0 to 70 μs with a gate width of 0.5 μs.

**Results and Discussions**

**Steady-State Photochemistry of Fl-An and Fl-EP.** Figure 3-2 shows the absorption and fluorescence spectra of Fl-An (red) and Fl-EP (blue). In accordance with its suggested structure, the absorption spectrum of Fl-An resembled the superposition of individual absorption spectra of An and Fl. Compared to carboxyfluorescein whose spectral maxima of absorbance and fluorescence were 492 and 517 nm in pH 8.0 Tris−$K^+$ buffer, respectively, Fl-An exhibited slightly red-shifted absorption and fluorescence spectra with 508 and 530 nm peaks, respectively. Considering the Fl-An chemical structure (Figure 3-1), this red-shift was caused by the substitution of chlorine and An on each side of the xanthene group (Xa). Indeed, both absorption and fluorescence spectra of Fl-Cl showed similar peaks to those of Fl-An.

Under irradiation of Fl-An with visible light (420−440 nm) in the presence of oxygen, the formation of Fl-EP was clearly monitored by absorption spectral changes (black → green in Figure 3-2). Simultaneously, the absorbance decrease of Fl at 508 nm occurred due to photodecomposition of Fl by the direct irradiation and $^1O_2$ oxidation. This “self” conversion of Fl-An and photobleaching mechanism will be further discussed in the latter sections. In addition, Fl is the fluorophore in both Fl-An and Fl-EP. Thus, only the fluorescence intensity of Fl was affected by the Fl-EP formation without any changes in the spectral shape and peak position.

The fluorescence quantum yields ($\Phi_{fl}$) of Fl-An, Fl-EP, and Fl-Cl were determined and in accordance with those reported previously (Table 3-2). However, $\Phi_{fl}$ of Fl-EP (~0.4)[24] was found to be approximately half of $\Phi_{fl}$ of the Fl-based dyads proposed by Tanaka et al.11 It is noteworthy that their dyads have An substituted on the center ring of Xa, whereas Fl-An has An substituted on the side ring of Xa. Thus, it is tentatively assumed that the substitution position of

An plays an important role in the internal conversion process influenced by rotational freedom between An and Xa. Suggestions to improve $\Phi_{fl}$ of Fl-EP can be found in the last section.

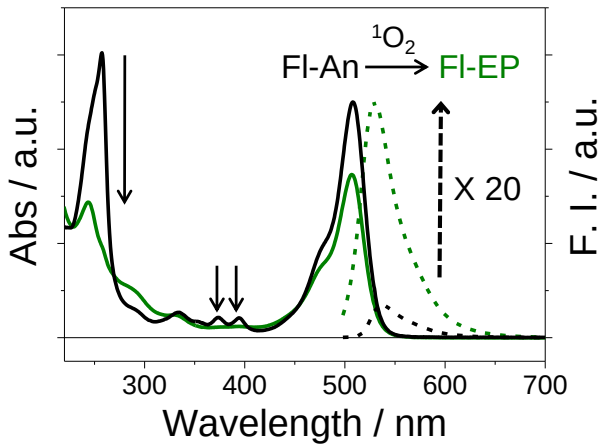


**Figure 3-2.** Normalized absorption (solid lines) and fluorescence spectra (dashed lines, $\lambda_{ex}$ = 465 nm) of Fl-An and Fl-EP in pH 8.0 Tris−$K^+$ buffer. Black arrows indicate spectral changes accompanied by the formation of Fl-EP. Conversion of Fl-An was completed after 13 min of irradiation in the wavelength range 420−440 nm.

**Table 3-2.** $\Phi_{fl}$ and $\tau_{fl}$ of Fl-An, Fl-EP, fluorescein, and Fl-Cl.

| compound | $\Phi_{fl}$ | $\tau_{fl}$ / ns |
|---|---|---|
| Fl-An | 0.009[a]<br>0.019 | 3.13[b] |
| Fl-EP | 0.45[a]<br>0.37 | n.d.[c] |
| fluorescein | 0.92[d] | 3.6[e] |
| Fl-Cl | 0.92 | 3.69 |

[a]Gollmer, A. et al., *Photochem. Photobiol.* **2011,** *87*, 671; [b]$\tau_{fl}$ of Fl-An is considered to be originated from Fl impurities without anthracene moiety (An) and/or preformed Fl-EP; [c].n.d. stands for no data available; [d]Magde, D. et al., *Photochem. Photobiol.* **2002,** *75*, 327; [e]Arik, M. et al., *J. Photochem. Photobiol. A* **2005**, *170*, 105.

**Intramolecular PET of Fl-An in the Singlet Exited State.** Since An and Fl are connected by one single bond and are not conjugated with each other, the intramolecular PET and back electron transfer (i.e. intramolecular charge separation and recombination, respectively) may occur in the picosecond time regime. When the PET occurs, **R** and $An^{\bullet+}$ are generated, and the radical ion pair disappears via the charge recombination. In order to observe such intramolecular electron transfer processes, the femtosecondlaser flash photolysis (fs-LFP) measurement was carried out for Fl-An and Fl-Cl. It should be noted that the transient absorption of **R** was positioned at a wavelength shorter than 400 nm, which was out of the monitoring region for the fs-LFP in the present experiment. Thus, PET and charge recombination of Fl-An were investigated from the transient absorption signals of Fl-An ground state bleaching, Fl-An in the singlet excited state ($^1$Fl*-An), its stimulated emission, and $An^{\bullet+}$ upon excitation at 500 nm which is absorbed by Fl mainly (Figure 3-3a). As shown in Figure 3-3, the broad and negative transient absorption signal centered at approximately 495 nm is assigned to the bleaching of Fl-An and Fl-Cl in the ground state. In addition, the transient absorption signals observed at 400−450 nm and longer than 700 nm are assigned to $^1$Fl* as reported previously.[25−29] In terms of the signal shape and decay time, there were largely two clear differences between $^1$Fl*-An and Fl-Cl in the singlet excited state ($^1$Fl*-Cl).

First, the whole transient absorption (400−450, >700 nm) as well as stimulated emission (around 550 nm) due to $^1$Fl* of $^1$Fl*-An decayed faster than those of $^1$Fl*-Cl. Second, a broad and short-lived transient absorption ($\tau \approx 5$ ps) was observed around 670 nm during the fs-LFP of Fl-An (Figure 3-3b), while no such transient absorption was for Fl-Cl (Figure 3-3d). This transient species exhibited a small rise for approximately 1 ps and then decayed with a time scale of a few ps (Figure 3-3e). Concerning the similarities in the spectral shape and position as reported previously,[15] this absorption can be assigned to $An^{\bullet+}$ generated from the intramolecular PET between $^1$Fl* and An in $^1$Fl*-An.

In order to understand the whole deactivation pathways of $^1$Fl*-An in the picosecond time scale and obtain the responsive rate constants, time profiles of the transient absorption signals were fitted with multi-exponential functions. The global fittings of time-resolved transient absorption spectra of $^1$Fl*-Cl in the range 410−465 nm gave the rate constant for the vibrational cooling and solvent relaxation processes ($k_c$) of $^1$Fl* in a Franck−Condon state ($^1$Fl*$^{hot}$-An) to be $2.3 \times 10^{11}$ $s^{-1}$. This rate constant is in accordance with the previous study that the cooling process

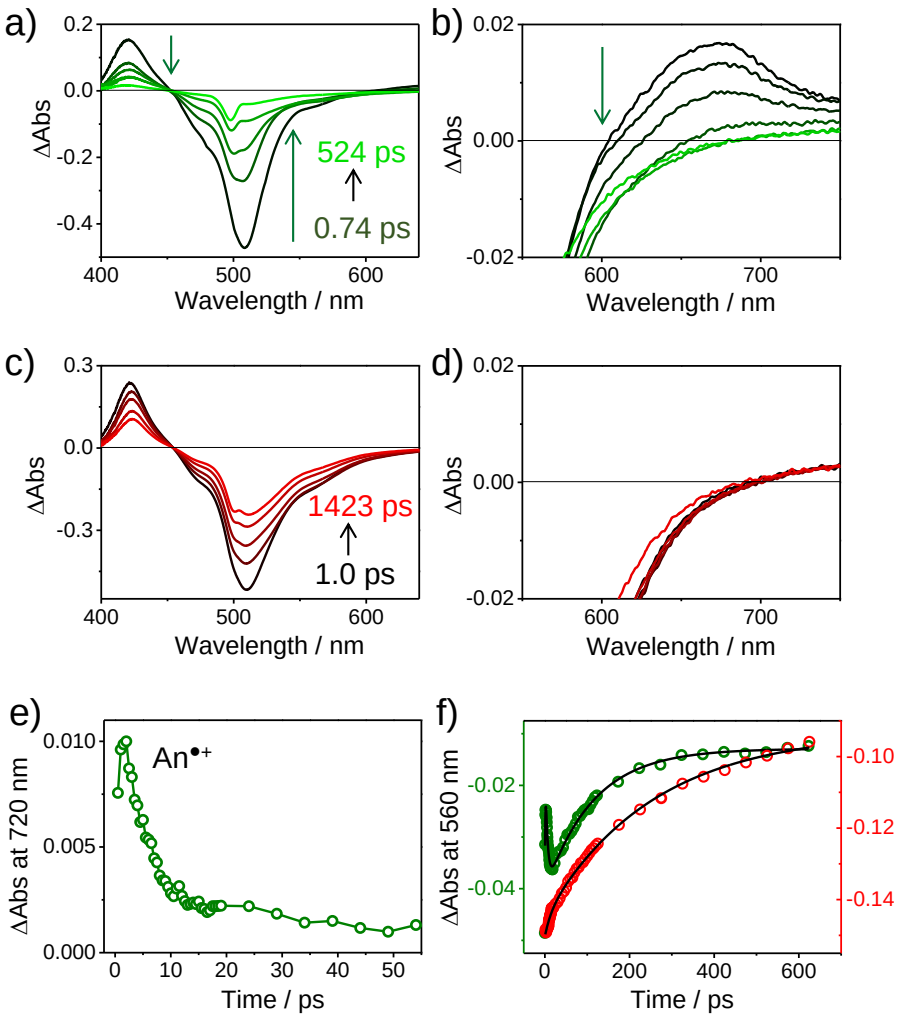


**Figure 3-3. (a)** Transient absorption spectra observed at 0.75, 6, 11, 54, and 524 ps (dark green to green) after a laser pulse during the fs-LFP of Fl-An. **(b)** Transient absorption spectra observed at 1.0, 3, 5, 11, 54, and 104 ps (dark green to green) after a laser pulse during the fs-LFP of Fl-An. Spectral changes due to $^{1}$Fl* decay, ground-state recovery, and charge recombination are directed with green arrows. **(c)** Transient absorption spectra observed at 1.0, 10, 104, 524, and 1423 ps (dark red to red) after a laser pulse during the fs-LFP of Fl-Cl. **(d)** Transient absorption spectra observed at 1.5, 5, 10, 54, 104, and 524 ps (dark red to red) after a laser pulse during the fs-LFP of Fl-Cl. **(e)** Time profile of transient absorption decay of $^{1}$Fl*-An observed at 720 nm. **(f)** Time profiles of transient absorption of $^{1}$Fl*-An (green) and $^{1}$Fl*-Cl (red) at 560 nm fitted with multi-exponential and double-exponential functions, respectively (black lines). [Fl-An] = 120 μM and [Fl-Cl] = 108 μM that have the same absorbance of approximately 3.0 (path length = 1 mm) at the excitation wavelength of 500 nm.

of Fl derivatives completed within a few ps.[27] Using this value, the time profiles of transient absorption of $^1$Fl*-An and $^1$Fl*-Cl at 560 nm were further fitted where stimulated emission of $^1$Fl* and transient absorption of $An^{\bullet+}$ can be observed together (Figure 3-3f). As mentioned earlier, the formation of $An^{\bullet+}$ ($\approx 10^{12}$ $s^{-1}$, Figure 3-3e) was found to be faster than vibrational cooling of $^1$Fl* ($2.3 \times 10^{11}$ $s^{-1}$). Thus, under the present experimental condition (pH 8.0 Tris−$K^+$ buffer and $\lambda_{ex}$ = 500 nm), charge separation and vibrational cooling take place competitively in $^1$Fl*$^{hot}$-An rather than in a sequential manner. As a result, the rate constants for the intramolecular PET and charge recombination of $^1$Fl*-An ($k_{PET}$ and $k_{CR}$, respectively) were determined to be $9.7 \times 10^{11}$ and $2.0 \times 10^{11}$ $s^{-1}$, respectively. In addition, a couple of slow relaxation times observed during $^1$Fl* decay and ground-state recovery apart from electron transfer processes are considered to be the components for the non-exponential decay of $^1$Fl* as reported previously.[27,30,31] Although the $\tau_{fl}$ of Fl is 3−4 ns (Table 3-2), the decay of $^1$Fl* and ground-state recovery kinetics monitored by the fs-LFP are often not in accordance with $\tau_{fl}$ due to the different method of the measurement[29] and intrinsic decay behavior of $^1$Fl* in a non-exponential way.[27,30,31]

As a matter of fact, $^1$Fl*-An should not show any fluorescence or long-lived species because it is deactivated via the intramolecular PET on a ps-time scale. However, the long-lived transient absorption signal for $^1$Fl* (>2 ns) was always observed to some extent during the fs-LFP of Fl-An (Figures 3-3a and 3-3b). This discrepancy is due to the contamination of Fl-EP[24] and infinitesimal impurity of Fl in the Fl-An sample.[23] Similarly, the preformed Fl-EP and/or fluorescent impurities give rise to dim fluorescence of Fl-An ($\Phi_{fl} \leq 0.02$) with $\tau_{fl}$ of 3.13 ns.

**Formation of Fl-An in the Triplet Excited State with Excitation at 532 nm.** Recently, there have been a couple of reports that revealed Fl-An can generate $^1O_2$ under irradiation at various excitation wavelengths even in the absence of Sens.[23,24] Ragas et al. confirmed the $^1O_2$ generation of Fl-An based on the observation of a fluorescence increase with increasing Fl-EP formation and phosphorescence of $^1O_2$ upon the 355 nm excitation.[23] In addition, Gollmer et al. triggered a conversion of Fl-An into Fl-EP using the 420 nm laser excitation.[24] However, the previous reports did not suggest the mechanism of $^1O_2$ generation. In fact, this phenomenon is surprising because Fl-based fluorescent sensors have been well-known to exhibit low $\Phi_{ISC}$ (<0.1), which made Fl an attractive and versatile candidate for the various fluorescent probes.

Furthermore, $^1O_2$ generation by Fl-An under irradiation is definitely an undesirable property for using Fl-An as the $^1O_2$ detection sensor. Herein, the author tried to elucidate this process in detail using nanosecond laser flash photolysis (ns-LFP).

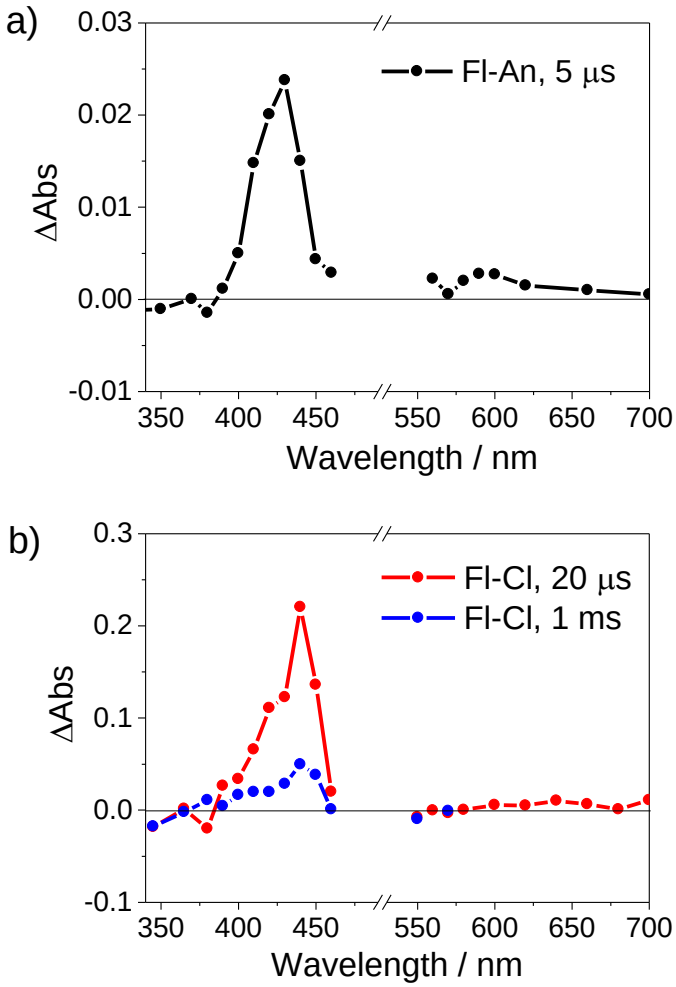


**Figure 3-4. (a)** Transient absorption spectra observed at 5 μs after a laser pulse during the ns-LFP of Fl-An with [Fl-An] = 100 μM at $\lambda_{ex}$ = 532 nm and 19 mJ cm$^{-2}$. **(b)** Transient absorption spectra observed at 20 μs (red) and 1 ms (blue) after a laser pulse during the ns-LFP of Fl- Cl in the presence of anthracene as a triplet Sens with [Fl-Cl] = 100 μM and [anthracene] = 300 μM at $\lambda_{ex}$ = 355 nm and 10 mJ cm$^{-2}$. In order to increase the absorbance of Fl-An at 532 nm, 45 vol% ACN in pH 8.0 Tris−K$^+$ buffer solution was used with a 0.5 cm path length.

To begin with, it is noteworthy that $^1O_2$ is generated from the bimolecular triplet−triplet energy transfer between $^3$Sens* and $^3O_2$. Considering the chemical structure of Fl-An (Figure 3-1), An and Fl behave as an independent chromophore, since they are not conjugated with each other. Hence, $^1O_2$ must be generated from the triplet−triplet energy transfer between An and/or Fl moieties in the triplet excited states ($^3$An* and/or $^3$Fl*, respectively) and $^3O_2$.

In order to clarify the excited state dynamics and species of Fl-An for the $^1O_2$ generation, transient absorption measurements using the ns-LFP were carried out. As shown in Figure 3-4a, only one peak at 430 nm was observed when Fl-An was excited at 532 nm. Nonetheless, the peak assignment was complicated because **X**, $^3$An*, and $^3$Fl* have absorption in the range 400−450 nm. Here, **X** is a kind of the radical cation species of trianionic Fl, resulting in the net charge of −2, and often generated from the triplet−singlet/triplet−triplet intermolecular PET or photoionization.[25,32−34] Unlike $^3$An* and $^3$Fl*, a decay rate of radical species is often insensitive to the oxygen concentration. On the other hand, the Parson group has reported that not only radical species but also rhodamine derivatives in the triplet excited state could be observed at around 400 nm.[26] Concerning the different kinds of dye and solvent, it is certainly plausible to monitor the absorption of $^3$Fl* in the range 400−450 nm. Although the absorption of 9,10-dimethylanthracene (DMA) in the triplet excited state ($^3$DMA*) was observed in the same wavelength region, the possibility of $^3$An*, generated from the intramolecular triplet−triplet energy transfer, was excluded. In Figure 3-4b, the transient absorption of Fl-Cl was well observed at 440 nm, although Fl-Cl does not have An (Figure 3-4b, red). Moreover, the triplet energy level of $^3$DMA* is slightly higher than that of $^3$Fl* (Table 3-3).

Taken together, the transient absorption observed in the range 400−450 nm is assigned to $^3$Fl*. This result is opposite to the report by Ragas et al. that no transient absorption of Fl-An at around 430 nm was observed upon the 532 nm excitation.[22] To understand this discrepancy, it is noteworthy that Fl-An exhibits too small ground state absorption at 532 nm to perform transient absorption measurement. Thus, 45 vol% acetonitrile (ACN)-mixed buffer solution was prepared to induce a slight spectral red-shift (app. 5 nm) and finally succeeded to observe the transient absorption signal clearly upon the 532 nm excitation (Figures 3-4a and 3-5a, lower). In addition, with the 532 nm excitation, the transient absorption decay profile at 430 nm was found to be oxygen-sensitive (Figure 3-5a, lower). Finally, clear rise and decay of $^1O_2$ phosphorescence were observed for Fl-Cl, and its singlet oxygen generation quantum yield ($\Phi_\Delta$) was determined to be

0.06 with the excitation at 532 nm. Since $^1O_2$ generation implicates the presence of $^3$Sens*, this finding further supported that $^3$Fl*-An was indeed formed and generated $^1O_2$ under visible light irradiation.

**Table 3-3.** Energy levels of Fl, An, and EP in the singlet and triplet excited states, and oxidation and reduction potentials of Fl and An from the previous studies.

| moieties | Singlet excitation energy / kJ mol$^{-1}$ | Triplet excitation energy / kJ mol$^{-1}$ | $E(D^+/D)$ / V vs SCE | $E(A/A^-)$ / V vs SCE |
|---|---|---|---|---|
| Fl (Fl-Cl) | 230.9[a] | 164.3[b] | 1.42[c] | -1.29[c] |
| An (DMA) | 301[d] | 168[d] | 1.67[d] | -2.14[e] |
| EP (DMA with endoperoxide) | 371.5[f] | 299.1[f] | n.d.[g] | n.d.[g] |

[a]Calculated from the 0-0 absorption of Fl-An; [b]Miura, T. et al., *J. Am. Chem. Soc.* **2003,** *125*, 8666; [c]Zhang, X.-F. et al., *Photochem. Photobiol.* **2010,** *86*, 492; [d]Wilkinson, F. et al., *J. Phys. Chem. Ref. Data* **1993,** *22*, 113; [e]Song, J. H. et al., *J. Am. Chem. Soc.* **1997,** *119*, 7381; [e]Corral, I. et al., *J. Comput. Chem.* **2008**, *29*, 1982; [g]n.d. stands for no data available.

**Two-Photon Ionization of Fl-An with Excitation at 355 nm.** During the present study, two-photon ionization of Fl-An was found to be an interesting phenomenon of Fl-An with the 355 nm excitation, indicating the wavelength effect of the excitation on the transient species. The 355 nm excitation of Fl-An induced the formation of the transient absorption at 430 nm which did not completely decay even by 2 ms regardless of the oxygen concentration (Figure 3-5a, upper). Meanwhile, the 532-nm excitation induced the transient absorption at 430 nm which decayed sensitively to oxygen (Figure 3-5a, lower). Obviously, the transient species observed with the 355 and 532 nm excitation were not identical, although they were monitored at the same wavelength.

Moreover, the formation yield of the transient species caused by the 355 and 532 nm excitations showed different dependencies on the laser intensity, indicating further information on their formation processes (Figure 3-5b). With the excitation at 532 nm, the transient absorption intensity increased linearly against the laser intensity, while the 355 nm excitation induced the nonlinear increase in transient absorption intensity. The plot of the logarithm of

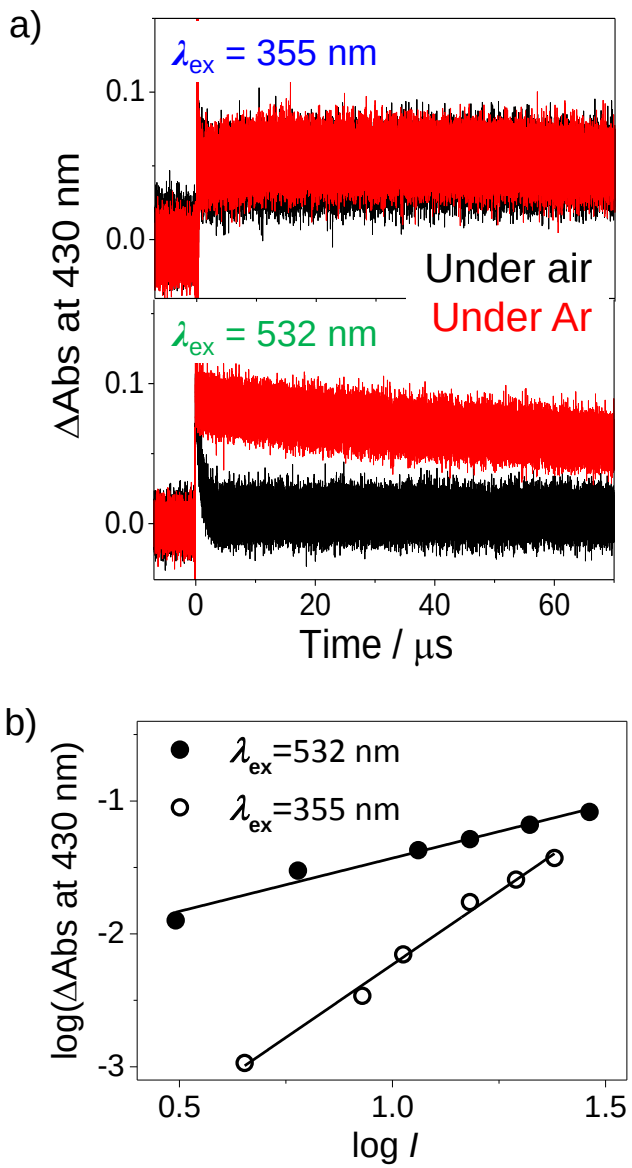


**Figure 3-5. (a)** Decay profiles of the transient absorption at 430 nm during the ns-LFP of Fl-An. Values of 24 and 29 mJ $cm^{-2}$ were used for $\lambda_{ex}$ = 355 and 532 nm, respectively, under the air- (black) and Ar-saturated (red) conditions. **(b)** Effects of the laser intensity ($I$, units: mJ $cm^{-2}$) and $\lambda_{ex}$ on the transient absorption at 430 nm observed at 100 ns and 5 μs after a laser pulse for the 532 nm (closed circles) and 355 nm excitation (open circles), respectively. Black lines are the results of linear fitting with slopes of 0.8 and 2.2 for the 532 and 355 nm excitation, respectively. [Fl-An] = 100 μM in the air-saturated 45 vol% ACN in pH 8.0 buffer solution with a 1 cm path length.

transient absorption intensity at 430 nm versus the logarithms of the 532 and 355 nm laser intensities showed linear lines with slopes of 0.8 and 2.2, respectively (Figure 3-5b). The results clearly indicated that the transient species observed at 430 nm were formed via the one-photon and two-photon processes with excitation at 532 and 355 nm, respectively.

With the excitation at 532 nm, $^3$Fl*-An with the peak of transient absorption at 430 nm was produced by one-photon absorption and easily quenched by nearby oxygen. From the fitting of decay profiles, the decay rate constants for $^3$Fl*-An ($k_T$) were found to be $1.2 \times 10^6$ and $1.5 \times 10^3$ $s^{-1}$ in the air and Ar-saturated conditions, respectively (cf. the latter becomes probably smaller if oxygen is completely removed from the solution). Based on the obtained $k_T$ and concentration of dissolved oxygen in 45 vol% ACN-mixed buffer solution, the rate constant of the bimolecular triplet−triplet energy transfer from $^3$Fl*-An to $^3O_2$ ($k_q$) was calculated to be $k_q = 1.2 \times 10^9$ $M^{-1}$ $s^{-1}$ (Table 3-4).

On the other hand, with the excitation at 355 nm, the transient species with an absorption peak at 430 nm was produced via the two-photon process. To date, the $\lambda_{ex}$-dependent behavior of Fl and rhodamine derivatives in the excited state has been substantially studied.[25,26,32] According to the report of the Lougnot group, irradiation of Fl-An with UV light instantaneously generates $^1$Fl*-An, and the subsequent absorption of the second photon further pumps $^1$Fl*-An up to Fl-An in the higher singlet excited state ($S_n$).[25] Consequently, this two-photon process leads to the ionization in a part to give **X** and solvated electron. Similarly, the transient species with a peak at 430 nm with the 355 nm excitation is assigned to be **X** caused by the two-photon ionization. Furthermore, the long-lived species was observed even at 1 ms after a pulse during the ns-LFP of Fl-Cl (Figure 3-4b, blue), and assigned to **X** produced with a direct excitation of Fl-Cl at 355 nm. In fact, not only the two-photon ionization but also the intermolecular PET between $^3$Fl* and Fl in the ground state or two $^3$Fl* have been considered to generate **X**.[33,35,36] If this bimolecular reaction occurred as the main process for the formation of **X**, the corresponding **R** must be monitored. However, the characteristic sharp transient absorption of **R** at 380 nm was obviously absent in Figure 4b, and negligible absorbance within a noise range in the case of Fl-An was detected at 380 nm (data are not shown). Furthermore, insensitivity of the decay signal against oxygen implicated (Figure 3-5a) that $^3$Fl*-An does not play a role in the formation of **X**. Finally, it should be pointed out that Ragas et al. assigned the long-lived species of Fl-An induced by the 355 nm excitation to **X**, resulting from the PET from Fl to $^1$An*.[23] Nonetheless, fs-LFP

experiments revealed that the charge recombination process deactivates R-An$^{\bullet+}$ within a few ps (Figure 3-3e). In addition, the charge separated states of the similar dyads were reported to exhibit μs lifetimes.[15] Furthermore, the nonlinear relation of Fl-An between the laser intensity and formation of its transient species indicates the excitation at 355 nm induces two-photon absorption, resulting in the long-lived radical species, **X** (Figure 3-5b). Overall, the transient species of Fl-An after the 355 nm excitation was presumably caused by two-photon ionization, rather than the electron transfer between Fl and An moieties.

**Relaxation Pathways of Fl-An.** Considering the obtained results and previous reports, a diagram for the individual deactivation pathway for the 355 and 532 nm excitation is proposed in Figure 3-6. To start with, the 355 nm excitation could pump both An and Fl (blue arrows). Especially, laser intensities used in the present study (>10 mJ cm$^{-2}$) enabled the two-photon ionization of Fl, resulting in **X**. The ionization quantum yields ($\Phi_{ion}$) were determined to be 0.0021 and 0.0026 at 19.5 and 24.0 mJ cm$^{-2}$, respectively. Since **X** is generated via two-photon absorption, $\Phi_{ion}$ increases as the laser intensity is raised. As reported previously, **X** becomes the main cause of dye photobleaching.[37] Hence, vulnerability of Fl-An against the 355 nm excitation can be understood by the formation of **X** readily produced with the high-intensity UV irradiation. Furthermore, concerning each redox potential and electrostatic interaction energy between the Fl-An radical ion pair (Table 3-3 and ref 15), both of the PET from Fl to $^1$An* and from An to $^1$Fl* are presumably possible, which results in **X**-An$^{\bullet-}$ and **R**-An$^{\bullet+}$, respectively. Due the relatively weak absorption of Fl-An in the ground state at 355 nm for the fs-LFP measurement and difficulty in the selective excitation of each moiety, the PET induced by the 355 nm excitation was not investigated in this study. In addition, a conversion of Fl-An into Fl-EP with the UV irradiation[23] implicates that the 355 nm excitation produces not only **X** but also $^1O_2$ via the deactivation of $^3$An*. Overall, $^1$An* is considered to be mostly deactivated via non-radiative relaxation pathways. This assumption is supported by the results of preliminary tests that the 350 and 375 nm excitations did not induce either An fluorescence or intramolecular singlet−singlet energy transfer from $^1$An* to Fl.

On the other hand, the 532 nm excitation pumped only Fl of Fl-An according to its absorption spectrum. Subsequently, the absence of destructive deactivation pathways facilitated the excited Fl-An to be relaxed in a photostable way. It should be noted that **R**-An$^{\bullet+}$ mainly originated from

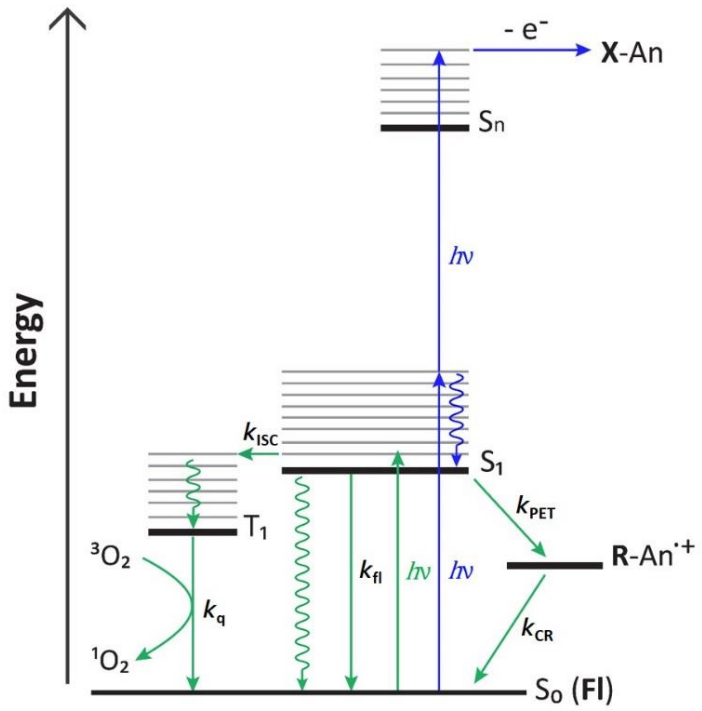


**Figure 3-6.** Relaxation pathways of Fl of Fl-An in the excited states, which were directly monitored in the present study. Blue and green arrows illustrate the excitation and deactivation processes with the 355 and 532 nm excitation, respectively. **X** and **R** indicate one-electron oxidized and reduced Fl, respectively.

**Table 3-4.** Various rate constants related to the relaxation pathways of Fl-An in the excited states shown in Figure 3-6.

| processes | descriptions | rate constants |
|---|---|---|
| $^1$Fl*-An → **R**-An$^{\bullet+}$ | Intramolecular electron transfer between $^1$Fl* and An | $k_{PET} = 9.7 \times 10^{11}$ s$^{-1}$ |
| **R**-An$^{\bullet+}$ → Fl-An | Charge recombination between **R** and An$^{\bullet+}$ | $k_{CR} = 2.0 \times 10^{11}$ s$^{-1}$ |
| $^1$Fl*-An → Fl-An + *hυ* | Radiative relaxation of $^1$Fl* | $k_{fl} = 2.5 \times 10^{8}$ s$^{-1}$ [a] |
| $^1$Fl*-An → $^3$Fl*-An | Intersystem crossing from $^1$Fl* to $^3$Fl* | $k_{ISC} = 6.6 \times 10^{6}$ s$^{-1}$ [b] |
| $^3$Fl*-An + $^3$O$_2$ → Fl-An + $^1$O$_2$ | Triplet-triplet energy transfer from $^3$Fl* to $^3$O$_2$ | $k_q = 1.2 \times 10^{9}$ M$^{-1}$ s$^{-1}$ |

[a]Calculated from $\Phi_{fl}$ and $\tau_{fl}$ of Fl-Cl; [b]Lougnot, D.-J. et al., *J. Photochem.* **1980,** *12*, 215.

$^1$Fl*$^{hot}$-An under the present experimental condition, but the charge separation of relaxed $^1$Fl*-An is still possible and may become the major process for fluorescence quenching provided that the different solvent and excitation wavelength are used. To prevent from overgeneralization of the relaxation pathway of Fl-An, the direction of arrow and process was denoted as $^1$Fl*-An → **R**-An$^{\bullet+}$ in Figure 3-6 and Table 3-4, respectively. In addition, the transient absorption of Fl-An (Figure 3-5a, below) decayed in an oxygen-dependent manner, and Fl-An was completely converted into Fl-EP under prolonged irradiation of visible light (Figure 3-2). Taken together, $^1$Fl* is thought to be relaxed via the intersystem crossing in a part to result in $^3$Fl* when the intramolecular PET process is prohibited.

**Evaluation of Fl-An and Suggestions for $\Phi_{fl}$ Improvement.** Fl-An has been a promising and attractive fluorescent sensor to detect $^1O_2$ because of its high sensitivity and selectivity to $^1O_2$, good turn on/off contrast, and water solubility. Also, it has similar absorption and fluorescence spectra with Fl. Thus, it can be exploited in a wide range of optical instruments. During the additional experiments using epi-illumination microscopy, the author could observe clear blinking and one-step photobleaching behavior of spin-coated Fl-EP, which are characteristics of fluorescence observed at the single-molecule level (Figure 3-7). This finding shed light on the potential usage of Fl-An to observe $^1O_2$ formation using single-molecule fluorescence spectroscopy. Moreover, there have been a number of reports that Fl-An was successfully exploited in biological studies in vitro as well as in vivo from DNA oligomers to human cell and plant leaves.[17–19,24] On the whole, Fl-An is considered to be particularly suitable for the biological and medical research which necessitate water-solubility and generally use continuous-wave light sources with lower fluence as compared to the pulsed laser.

Despite the several advantages above, the present study suggested that Fl-An should be used with a careful consideration because the undesirable processes, such as $^1O_2$ generation and photodecomposition, can occur depending on $\lambda_{ex}$, laser intensity, and oxygen concentration. Since prolonged irradiation leads to the gradual decrease in fluorescence of Fl-An, initially high $\Phi_{fl}$ is important to attenuate the inevitable fluorescence decrease upon irradiation time. $\Phi_{fl}$ of Fl-EP is approximately half (~0.4) of that of the similar dyads suggested by Tanaka et al. (>0.8).[11] From parabolic fitting of $k_{PET}$ and $k_{CR}$ of the dyads with Marcus theory, they obtained the electronic coupling matrix element ($V$) value relatively smaller (7.0 cm$^{-1}$) as compared to those

of other reported dyads (~1−100 $cm^{-1}$).[15] It was explained by the restricted free rotation between Xa and An rings because of a carboxylic acid substituted on An that kept Xa and An in orthogonal geometry. On the other hand, according to the structure of Fl-An,[24] An is substituted on the side ring of Xa, which has a larger angle for free rotation as compared to the center position substitution, and does not have an additional substitution group that holds Xa and An perpendicular to each other. Generally speaking, free rotation of chromophore is closely related to an increase in the internal conversion quantum yield ($\Phi_{IC}$) and finally leads to a decrease in $\Phi_{fl}$.[38] Thus, the different substitution position of An on Xa and the introduction of carboxilyic acid on An can be considered in order to decrease rotation freedom between An and Xa rings, enhance $\Phi_{fl}$, and obtain a brighter signal of Fl-An in the presence of $^1O_2$.

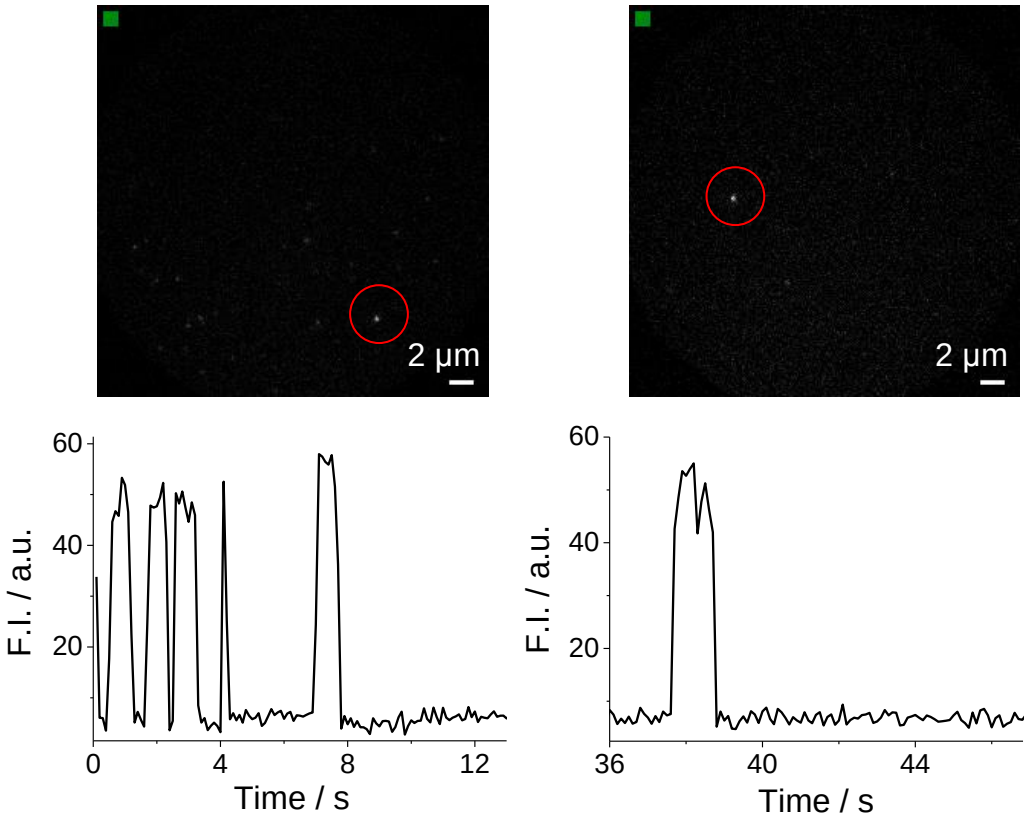


**Figure 3-7.** Time trajectory of single-molecule fluorescence of Fl-EP. $\lambda_{ex}$ = 514 nm and scale bar: 2 μm.

## Conclusion

In the present study, the author has thoroughly scrutinized the photochemistry of Fl-An: its validity of a fluorescence sensor, intramolecular PET dynamics, $^1O_2$ generation, etc. The author has confirmed that absorption of An disappeared and fluorescence increased with the formation of Fl-EP during irradiation of Fl-An in the range 420−440 nm (Figure 3-2). Furthermore, the PET as the intramolecular fluorescence quenching of $^1$Fl* by An in the absence of $^1O_2$ to give **R**-$An^{\bullet+}$ ($k_{PET}$ = 9.7 × $10^{11}$ $s^{-1}$) and the subsequent back electron transfer to reproduce Fl-An occurred ($k_{CR}$ = 2.0 ×$10^{11}$ $s^{-1}$) (Figure 3-3). Finally, on the basis of the ns-LFP measurements, photodynamics of Fl-An from the μs to ms time regime were strongly dependent on λex and oxygen concentration (Figures 3-4 and 3-5). Formation of **X** ($\Phi_{ion}$ = 0.003 at 24 mJ $cm^{-2}$) and $^3$An* during irradiation of Fl-An at 355 nm caused the irreversible dye photobleaching and $^1O_2$ generation, respectively. Meanwhile, the excitation at 532 nm resulted in the formation of $^3$Fl* that subsequently generated $^1O_2$ ($\Phi_\Delta$ < 0.06 and $k_q$ = 1.2 × $10^9$ $M^{-1}$ $s^{-1}$) and Fl-EP. Compared to the previous studies on Fl-An that lack a comprehensive discussion and quantitative analysis on the kinetics, this report clearly proposed and fully elucidated the whole picture of the relaxation dynamics of Fl-An using various time-resolved spectroscopic methods.

The author would like to make a final remark on Fl. Since the 1870s, Fl is one of the most widely used fluorescence markers in a variety of fields. Nonetheless, the results presented here suggest that photochemistry of Fl-An, one of the Fl derivatives, has a great dependence on the irradiation conditions, and it can generate $^1O_2$ by the excitation in the UV and visible range. Subsequently, generated $^1O_2$ further oxidizes Fl, resulting in the photooxidation and dye photobleaching.[36] Due to its photoinstability, nowadays, Fl is not frequently used in studies which require intense and prolonged irradiation, for example, single-molecule fluorescence spectroscopy and dye laser application, respectively. On the other hand, Fl is still actively used in the biological studies in order to visualize organelles, map intracellular pH, and detect ROS.[39–42] Because the prolonged irradiation undoubtedly leads to the formation of $^1O_2$ and consequently a cytotoxic effect and photodegradation of the dye, the researchers who choose Fl as a fluorescent marker should take a particular note of the irradiation conditions.

**References**


(1) Ogilby, P. R. *Chem. Soc. Rev.* **2010**, *39*, 3181.
(2) Tachikawa, T.; Majima, T. *J. Fluoresc.* **2007**, *17*, 727.
(3) Apel, K.; Hirt, H. *Ann. Rev. Plant Biol.* **2004**, *55*, 373.
(4) Dröge, W. *Physiol. Rev.* **2002**, *82*, 47.
(5) Zheng, G.; Chen, J.; Stefflova, K.; Jarvi, M.; Li, H.; Wilson, B. C. *Proc. Natl. Acad. Sci. U.S.A.* **2007**, *104*, 8989.
(6) da Silva, E. F. F.; Pedersen, B. W.; Breitenbach, T.; Toftegaard, R.; Kuimova, M. K.; Arnaut, L. G.; Ogilby, P. R. *J. Phys. Chem. B* **2011**, *116*, 445.
(7) Kuimova, M.; Botchway, S.; Parker, A.; Balaz, M.; Collins, H.; Anderson, H.; Suhling, K.; Ogilby, P. *Nat. Chem.* **2009**, *1*, 69.
(8) Oleinick, N. L.; Morris, R. L.; Belichenko, I. *Photochem. Photobiol. Sci.* **2002**, *1*, 1.
(9) Naito, K.; Tachikawa, T.; Cui, S.-C.; Sugimoto, A.; Fujitsuka, M.; Majima, T. *J. Am. Chem. Soc.* **2006**, *128*, 16430.
(10) Sen, F.; Boghossian, A. A.; Sen, S.; Ulissi, Z. W.; Zhang, J.; Strano, M. S. *ACS Nano* **2012**, *6*, 10632.
(11) Tanaka, K.; Miura, T.; Umezawa, N.; Urano, Y.; Kikuchi, K.; Higuchi, T.; Nagano, T. *J. Am. Chem. Soc.* **2001**, *123*, 2530.
(12) Voigt, N. V.; et al. *Nat. Nanotechnol.* **2010**, *5*, 200.
(13) Christ, T.; Kulzer, F.; Bordat, P.; Basché, T. *Angew. Chem., Int. Ed.* **2001**, *40*, 4192.
(14) Arian, D.; Kovbasyuk, L.; Mokhir, A. *J. Am. Chem. Soc.* **2011**, *133*, 3972.
(15) Miura, T.; Urano, Y.; Tanaka, K.; Nagano, T.; Ohkubo, K.; Fukuzumi, S. *J. Am. Chem. Soc.* **2003**, *125*, 8666.
(16) Zhang, Y.; Aslan, K.; Previte, M. J. R.; Geddes, C. D. *Proc. Natl. Acad. Sci. U.S.A.* **2008**, *105*, 1798.
(17) Osakada, Y.; Kawai, K.; Tachikawa, T.; Fujitsuka, M.; Tainaka, K.; Tero-Kubota, S.; Majima, T. *Chem. Eur. J.* **2012**, *18*, 1060.
(18) Flors, C.; Fryer, M. J.; Waring, J.; Reeder, B.; Bechtold, U.; Mullineaux, P. M.; Nonell, S.; Wilson, M. T.; Baker, N. R. *J. Exp. Bot.* **2006**, *57*, 1725.
(19) Shen, Y.; Lin, H.; Huang, Z.; Xiao, L.; Chen, D.; Li, B.; Xie, S. *Proc. SPIE* **2010**, *7845*, 78451F.
(20) Xiao, L.; Gu, L.; Howell, S. B.; Sailor, M. J. *ACS Nano* **2011**, *5*, 3651.
(21) Vankayala, R.; Sagadevan, A.; Vijayaraghavan, P.; Kuo, C.-L.; Hwang, K. C. *Angew. Chem., Int. Ed.* **2011**, *50*, 10640.
(22) Ragàs, X.; Cooper, L. P.; White, J. H.; Nonell, S.; Flors, C. *ChemPhysChem* **2011**, *12*, 161.
(23) Ragas, X.; Jimenez-Banzo, A.; Sanchez-Garcia, D.; Batllori, X.; Nonell, S. *Chem. Commun.* **2009**, 2920.
(24) Gollmer, A.; Arnbjerg, J.; Blaikie, F.; Pedersen, B.; Breitenbach, T.; Daasbjerg, K.; Glasius, M.; Ogilby, P. *Photochem. Photobiol.* **2011**, *87*, 671.
(25) Lougnot, D.-J.; Goldschmidt, C. R. *J. Photochem.* **1980**, *12*, 215.

(26) Ferguson, M.; Beaumont, P.; Jones, S.; Navaratnam, S.; Parsons, B. *Phys. Chem. Chem. Phys.* **1999**, *1*, 261.
(27) Fita, P.; Fedoseeva, M.; Vauthey, E. *J. Phys. Chem. A* **2011**, *115*, 2465.
(28) Dobryakov, A. L.; Kovalenko, S. A.; Ernsting, N. P. *J. Chem. Phys.* **2005**, *123*, 044502.
(29) Mani, T.; Niedzwiedzki, D. M.; Vinogradov, S. A. *J. Phys. Chem. A* **2012**, *116*, 3598.
(30) Choi, J.; Kim, S.; Tachikawa, T.; Fujitsuka, M.; Majima, T. *Phys. Chem. Chem. Phys.* **2011**, *13*, 5651.
(31) Hilgendorff, M.; Sundström, V. *J. Phys. Chem. B* **1998**, *102*, 10505.
(32) Duarte, F. J.; Hillman, L. W. *Dye Laser Principles: With Applications*; Academic Press: Boston, MA, 1990.
(33) Song, L.; Varma, C.; Verhoeven, J.; Tanke, H. *Biophys. J.* **1996**, *70*, 2959.
(34) Cordier, P.; Grosswei, Li. *J. Phys. Chem.* **1968**, *72*, 2018.
(35) Kasche, V.; Lindqvist, L. *J. Phys. Chem.* **1964**, *68*, 817.
(36) Gaigalas, A. K.; Wang, L.; Cole, K. D.; Humphries, E. *J. Phys. Chem. A* **2004**, *108*, 4378.
(37) Widengren, J.; Chmyrov, A.; Eggeling, C.; Lofdahl, P.; Seidel, C. *J. Phys. Chem. A* **2007**, *111*, 429.
(38) Berezin, M. Y.; Achilefu, S. *Chem. Rev.* **2010**, *110*, 2641.
(39) Han, J.; Burgess, K. *Chem. Rev.* **2009**, *110*, 2709.
(40) Park, Y. I.; et al. *Adv. Mater*. **2012**, *24*, 5755.
(41) Idris, N. M.; Gnanasammandhan, M. K.; Zhang, J.; Ho, P. C.; Mahendran, R.; Zhang, Y. *Nat. Med.* **2012**, *18*, 1580.
(42) Wang, X.-d.; Stolwijk, J. A.; Lang, T.; Sperber, M.; Meier, R. J.; Wegener, J.; Wolfbeis, O. S. *J. Am. Chem. Soc.* **2012**, *134*, 17011.

# Chapter 4. Unprecedented J-aggregate Formation of Si-Rhodamine and 9-Phenylanthracene Dyad and its Photochemistry

## Introduction

Self-assembly formation and dynamics of charge and energy transports through the building blocks are of central importance in the development of photovoltanics, optodevice, and solar cell.[1] Not only in nanodevice development, but a formation of chromophore aggregation is also an intriguing phenomenon for the design of a fluorescence probe.[2-4] For instance, aggregation-induced emission (AIE) has successfully overcome a typical drawback of dyes at the high concentration (i.e. a few μM to mM depending on the dye), resulting in fluorescence quenching. It rather gives higher signal-to-noise (S/N) ratio as dye concentration increases and hence is especially suitable for *in vivo* imaging.[3] In addition, several examples of aggregation-induced colorimetric changes versus various stimulus have been reported, which can be easily detected by the naked eye and appropriate to a practical sensory material.[2]

According to the exciton theory, two interacting molecules can form either blue-shifted and non-fluorescent dimer or red-shifted and fluorescent dimer.[5] The former is generally called H-aggregate, whereas the latter is assigned to J-aggregate, depending on the values of the angle ($\theta$) between the longitudinal axis of the monomer transition moments ($54.7° < \theta < 90°$ is H-aggregate, whereas $0° < \theta < 54.7°$ is J-aggregate).[5] As mentioned above, it is the H-aggregate formation that induces fluorescence quenching of the common fluorophores in poor solvent at the high concentration.[6-9] Compared to porphyrin, perylene dimide, and cyanine derivatives that many rational molecular designs have been introduced to control the aggregate formation,[10] the slipped stacking of the common fluorescence probe has been mostly achieved by adsorption on the surface such as glass and zeolite.[11, 12] Even though there are a few reports on the stimulus-induced J-aggregation of fluorophore without a template,[13] their exact structures and photochemistry have not been clarified in depth. To construct a self-assembly of rhodamine without non-physiological additives, the author focused on the organic molecular blocks which form crystal structures with multi-color fluorescence depending on the chromophore arrangement.[14, 15] In this study, H- and J-aggregate formations of silicon-containing rhodamine

(Si-rhodamine) substituted by 9-phenylanthracenyl group, namely Si-An, were investigated (Figure 4-1).

## Experimental Section

**Materials.** All chemical reagents and solvents used for the synthesis were purchased from Sigma-Aldrich Chemical Co., Tokyo Chemical Industries, Nacalai Tesque, and Wako Pure Chemical, and used without further purification. 2-Methylbenzene substituted Si-rhodamine (Si-Me, Figure 4-1) was synthesized according to the previous report by Koide et al.[16], and Si-An was synthesized as described in Supporting Figure. In all spectroscopic experiments, Si-An and Si-Me stored in dimethyl sulfoxide (DMSO) at –20°C in dark were used.

**Characterizations of Si-An.** $^{1}$H-, $^{13}$C-nucler magnetic resonance (NMR) spectra, and high resolution mass spectrum (HRMS) of Si-An were measured by a JEOL ESC400 (400 MHz), JEOL ESA600 (150 MHz), and LTQ Orbitrap XL™ Hybrid Ion Trap-Orbitrap Mass Spectrometer with electron spray ionization (ESI), respectively. NMR chemical shift, *J*-value and integral were calculated using Delta Ver.5 software (JEOL).

**Steady-State Measurements.** Methanol at the spectroscopic grade, pH 7.5 phosphate buffered saline (PBS) solution without $Ca^{2+}$ and $Mg^{2+}$ (both purchased from Nacalai Tesque), or MilliQ water were used as solvent. Ground-state absorption and fluorescence emission spectra were measured using a Shimadzu UV-3100 and Horiba FluoroMax-4, respectively. Bulk irradiation was performed using a xenon source (LAX-C100, Asahi Spectra) and wavelength filter (BA510-550, Olympus). Particle size of Si-An aggregates was measured using a fiber-optics particle analyzer with autosampler, FPAR-1000 (Otsuka electronics).

**Single Crystal Diffraction.** Diffraction data were collected by using the synchrotron radiation ($\lambda$ = 0.8000 Å) at the BL38B1 in the SPring-8 with approval of JASRI (2014A1252). The cell refinements were performed with HKL2000 software.[17] Direct method (SIR-2008) was used for the structure solution.[18] Calculation was performed with the observed reflections [$I > 2\sigma(I)$] with

the program CrystalStructure crystallographic software packages,[19] except for refinement, which was performed using SHELXL-2013.[20] All non-hydrogen atoms was refined with anisotropic displacement parameters, and hydrogen atoms were placed in idealized positions and refined as rigid atoms with the relative isotropic displacement parameters.

$C_{39}H_{37}ClN_2O_5Si$, $M_w$ = 677.27, $a$ = 9.8459(5), $b$ = 10.5371(10), $c$ = 19.8151(17) Å, α = 94.748(5)°, β = 98.528(5)°, γ = 110.714(5)°, $V$ = 1881.2(3) Å$^3$, $T$ = 93 K, triclinic, space group $P$-1 (No. 2), $Z$ = 2, $\rho_{calcd}$ = 1.196 g cm$^{-3}$, 6548 unique reflections, the final $R$1 and $wR$2 values 0.0958 ($I > 2.0\sigma(I)$) and 0.3422 (all data), respectively. Crystallographic data for this paper has been deposited at the Cambridge Crystallographic Data Centre under deposition numbers CCDC 1037986.

**Transient Absorption Measurements.** The transient absorption spectra on the sub-ps to ns time scale were measured by the pump and probe method using a regenerative amplified titanium sapphire laser (Spectra Physics, Spitfire Pro F, 1 kHz) pumped by a Nd:YLF laser (Spectra Physics, Empower 15) for Si-Me, Si-An, and Si-DMA dissolved in methanol or MilliQ water. In methanol where Si-rhodamine is present as a monomer, the samples of Si-Me, Si-An, and Si-DMA were prepared at the concentration where they have the absorbance of 1.2, 1.2, and 0.9 with 0.2-cm path length at 650 nm, respectively ([Si-Me], [Si-An], and [Si-DMA] ≈ 65 μM). In MilliQ, Si-An H- and J-aggregate samples were prepared at the concentration where they have the absorbance of approximately 0.37 at 650 nm and 1.4 at 740 nm with 0.1-cm path length, respectively ([Si-An] = 100 and 200 μM for H- and J-aggregate samples, respectively). An excitation pulse at 650 or 740 nm (i.e. the former is for monomer and H-aggregate samples, and the latter is for J-aggregate sample) was generated by optical parametric amplifier (Spectra Physics, OPA-800CF). A white continuum pulse, which was generated by focusing the residual of the fundamental light to a rotating $CaF_2$ plate after a computer controlled optical delay, was divided into two parts and used as the probe and the reference lights, of which the latter was used to compensate the laser fluctuation. Both probe and reference lights were directed to a sample cell with 0.1 cm of path length and were detected with a charge-coupled device detector equipped with a polychromator (Solar, MS3504).

**Exchanging Counterion of Si-An.** Before the treatment, chloride ion is considered to be the counterion of Si-An, which probably comes from washing with brine during the work-up process of Si-An synthesis. In order to change the counterion of Si-rhodamine to the bulkier one, the previously reported method for rhodamine B octadecyl ester has been followed.[21] Briefly, 1 mg of Si-An (app. 1.8 μmol) dissolved in 0.2 mL acetonitrile was added to the 0.8 mL acetonitrile solution containing 50 eq. of sodium tetraphenylborate ($NaBPh_4$) or sodium hexafluorophosphate ($NaPF_6$). Under magnetic stirring, Si-An solution with excess salts were kept in dark for overnight. Next, the blue solid was obtained after reduced pressure evaporation, followed by extraction with water to remove excess amounts of salt. Exchanging of counterion from $Cl^-$ to $BPh_4^-$ or $PF_6^-$ was confirmed by different $R_f$ of thin layer chromatography (TLC) and $^1$H-NMR spectra especially in the case of $NaBPh_4$ (data not shown). From $R_f$ of TLC, exchanging of counteranion of Si-An has been accomplished with nearly 100% yield although the exact yield could not be determined due to errors in weight caused by remaining salt and absolutely small amount of Si-An ($\leq$ 1 mg after extraction).

**Measurements of $\tau_{fl}$ and Quantum Yield** ($\Phi_{fl}$)**.** $\tau_{fl}$s of Si-Me and Si-An in methanol were measured using a time-resolved fluorescence microscope with a confocal optics (MicroTime 200; PicoQuant, Berlin-Adlershof, Germany). In order to measure $\tau_{fl}$, 70 μL of 100 nM Si-Me or 500 nM Si-An methanol solutions were loaded into the micro-chamber made by a 1-inch glass cover slip and Secure-Seal (S24733, Invitrogen). The samples were excited through an oil objective (Olympus, UAPON 150XOTIRF; 1.45 NA, 150x) with a 640-nm pulsed laser (PicoQuant, full width at half-maximum 120 ps) controlled by a PDL-800B driver (PicoQuant). The emission was collected with the same objective and detected by a single photon avalanche photodiode (Micro Photon Devices, PDM 50CT) through a 75-μm pinhole for spatial filtering to reject out-of-focus signals and 680/40 bandpass filter (Chroma). The data collected using the PicoHarp 300 TCSPC module (PicoQuant) were stored in the time-tagged time-resolved mode (TTTR), recording every detected photon with its individual timing.

To determine $\Phi_{fl}$ of Si-An, Si-Me ($\Phi_{fl}$ = 0.32) was used as a reference. In order to decrease the error and prevent the intermolecular interactions, the dye samples with absorbance of 0.005, 0.01, and 0.015 at 600 nm were prepared. Next, the integrated areas of fluorescence spectra of the

samples were calculated and linearly fitted against the responsive absorbance. Finally, $\Phi_{fl}$ was determined by comparing the slope of the linear plots with that of Si-Me.

**Pulse Radiolysis of Si-Me.** Pulse radiolysis experiments were performed using an electron pulse (28 MeV, 8 ns, 0.7 kGy per pulse) from a linear accelerator at Osaka University. In the present study, 200 μM Si-Me was dissolved in pH 7.4 PBS buffer solution with [*tert*-butanol] = 100 mM to generate Si-rhodamine radical anion (Si-R$^{\bullet-}$), and as for Si-rhodamine radical cation (Si-R$^{\bullet+}$), [$Na_2S_2O_8$] = 3 mM was further added.[22] The transient absorption measurement during the pulse radiolysis was carried out using a nanosecond photoreaction analyzer system (Unisoku, TSP-1000). A pulsed 450 W Xe arc lamp (Ushio, UXL-451-0) was employed as a monitor light source. The monitor light passed through the sample solution was focused on the entrance slit of a monochromator (Unisoku, MD200) and detected with a photomultiplier tube (Hamamatsu Photonics, R2949) and a transient digitizer (Tektronix, TDS580D). The transient absorption spectra were measured using a photodiode array (Hamamatsu Photonics, S3904-1024F) with a gated image intensifier (Hamamatsu Photonics, C2925-01) as a detector. Transient extinction coefficients ($\varepsilon$) of Si-rhodamine radical cation and anion were calculated as compared to the concentration of the initially appeared transient species of $Cl_2^{\bullet-}$ and $e_{sol}^-$, respectively ($\varepsilon$ of $Cl_2^{\bullet-}$ and $(e^-)_{aq}$ are 8,800 $M^{-1}$ $cm^{-1}$ at 340 nm[23] and 23,000 $M^{-1}$ $cm^{-1}$ at 700 nm,[24] respectively). Both spectra of Si-R$^{\bullet+}$ and Si-R$^{\bullet-}$ (Figure 4-7a) were taken at 5 μs after a pulse.

## Results and Discussions

**Synthesis and Optical Properties of Si-An.** Phenylanthracene derivatives form diverse crystal structures from the slipped-stacked column to herringbone structures upon the addition of solvent, organic and inorganic salts.[14] The author substituted 9-phenylanthracene to Si-rhodamine, expected to work as an intramolecular template to align fluorophore in an unusual way. Si-rhodamine is a far-red to near-infrared fluorescent rhodamine derivative and has been actively exploited especially in high-resolution fluorescence microscopy of cell imaging.[7, 25] Similar to the previous Si-rhodamine derivatives, Si-An exhibits far-red absorption and fluorescence ($\lambda_{abs}$ = 648 nm and $\lambda_{fl}$ = 667 nm in methanol). However, fluorescence quantum yield and lifetime ($\Phi_{fl}$

and $\tau_{fl}$, respectively) of Si-An were 0.05 and 0.75 ns in methanol, respectively, which are 6-fold weaker and 5 times shorter than Si-rhodamine without an anthracene moiety (Si-Me). Similar phenomenon has been reported previously that $\Phi_{fl}$ of hydroxyphenylfluorone (i.e. a dyad of fluorescein and benzene) is 4 times smaller than that of TokyoGreen (i.e. a dyad of fluorescein and 2-methylbenzene).[26] This is because the methyl substitution at 2 position of the benzene prohibits rotations between fluorescein and phenyl moieties, whereas this geometric hindrance does not exist in hydroxyphenylfluorone, resulting in the increased rate of internal conversion. If there is no faster additional relaxation process apart from fluorescence, therefore, weaker fluorescence of Si-An than Si-Me originates from the increased rate of internal conversion, caused by more freedom of the ring rotation between Si-rhodamine and phenyl moieties.

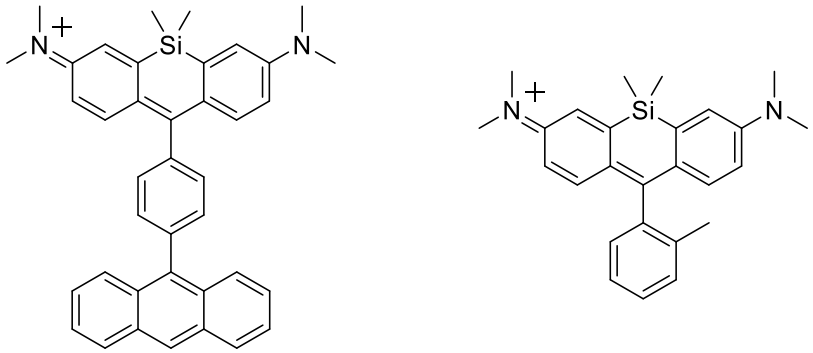


**Figure 4-1.** Chemical structures of Si-An and Si-Me.

**Table 4-1.** $k_{rad}$ and $k_{nr}$ of Si-Me and Si-An calculated from $\Phi_{fl}$ and $\tau_{fl}$ in methanol.

| entry | $\Phi_{fl}$ | $\tau_{fl}$ / ns | $k_{rad}$ / $s^{-1}$ | $k_{nr}$ / $s^{-1}$ |
|---|---|---|---|---|
| Si-Me | 0.32 | 3.56 | $0.9 \times 10^8$ | $1.9 \times 10^8$ |
| Si-An | 0.05 | 0.75 | $0.9 \times 10^{8\,a}$ | $1.8 \times 10^{9\,b}$ |

[a]Since fluorophores of Si-Me and Si-An are the same, Si-rhodamine, $k_{rad}$s of Si-Me and Si-An are assumed to be the same when calculating $k_{nr}$; [b]This value is calculated based on $\tau_{fl}$ of Si-An.

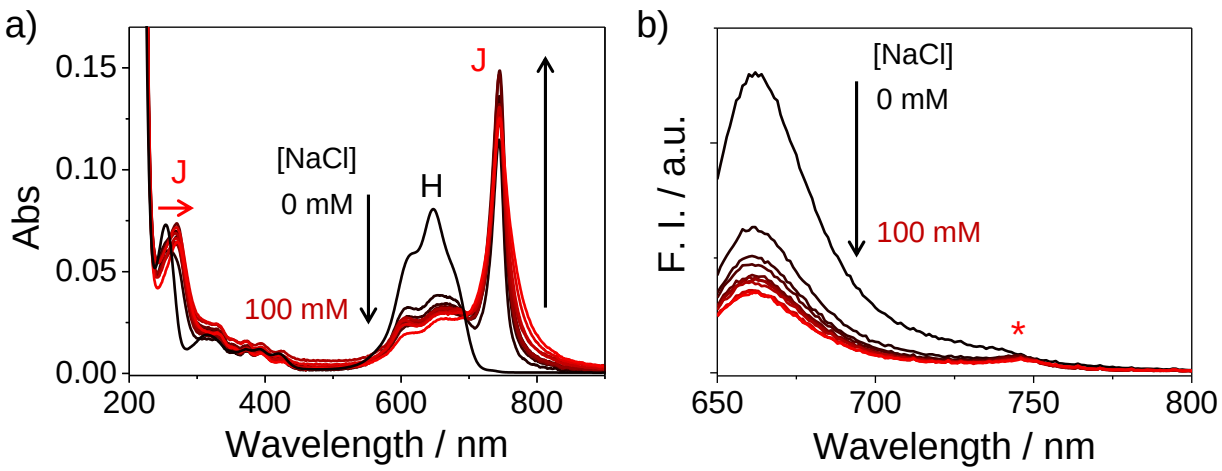


**Figure 4-2.** Changes in **(a)** absorption and **(b)** fluorescence spectra of Si-An in MilliQ water upon the addition of NaCl from 0 to 100 mM (dark red to red). [Si-An] = 5 μM, pathlength: 0.2 cm, and $\lambda_{ex}$ = 640 nm. The spectra were taken at around 30 min after the sample preparation. Black and red arrows show spectral changes reflecting a conversion from H- to J-aggregates of Si-rhodamine and the arrangement of anthracene moieties in a slipped-stacked manner, respectively. A red asterisk indicates J-aggregate emission of Si-An.

**Spectral Changes upon H- and J-Aggregate Formations of Si-An.** In the aqueous solution, Si-rhodamine normally forms H-aggregate similar to other rhodamine derivatives, such as rhodamine B and tetramethylrhodamine.[6,7,9] Surprisingly, Si-An is found to change its aggregation from H- to J-type upon the addition of NaCl ($\lambda_{J,abs}$ = 744 nm, Figure 4-2a). Moreover, the number of photons emitted (cf. integral of fluorescence spectra) of Si-An decreases as more Si-An J- aggregate forms (Figure 4-2b). Even though J-aggregate is known to be fluorescent based on the exciton theory, fluorescence of Si-An J-aggregate is negligible ($\lambda_{J,fl}$ = 746 nm, a red asterisk of Figure 4-2b). This is an unexpected phenomenon considering that a radiative relaxation process is allowed in J-aggregate, opposite to H-aggregate.[5]

**$^1O_2$ Reactivity of Si-An J-Aggregate.** To understand this finding comprehensively, absorption and fluorescence spectral changes during disruption of Si-An J-aggregate have been monitored (Figure 4-3). Anthracene derivative is known to react with singlet oxygen ($^1O_2$), which is

molecular oxygen in the lowest singlet excited state, and forms endoperoxide at its center ring.[6, 27] In Figure 4-3, changes in Si-An absorption and fluorescence spectra under 510−550 nm photoirradiation of tetra-(*N*-methyl-4-pyridyl)porphyrin (TMPyP4) for 120 min are shown. Interestingly, simultaneous changes in absorption spectra, a decrease of J-aggregate band at 742 nm and increase of Si-An monomer band at 648 nm, were monitored, while absorption bands that correspond to the anthracene moiety decreased. At the same time, fluorescence increased approximately 3-fold upon $^1O_2$ addition reaction. Here, after endoperoxide formation at the center ring of anthracene, the planarity of the anthracene moiety is lost, resulting in a prevention of dense J-aggregate packing of Si-An and a release of monomeric molecules of endoperoxidized Si-An (Si-EP). Thus, fluorescence quenching of Si-An J-aggregate is correlated to the pattern of molecular packing that facilitates an additional relaxation pathway of Si-rhodamine in the singlet excited state ($^1$Si-R*).

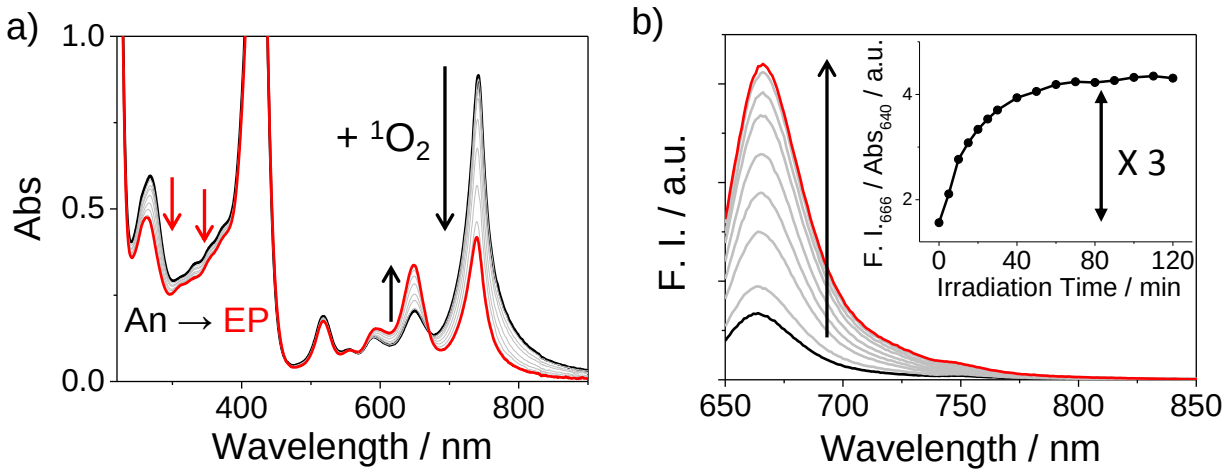


**Figure 4-3.** Changes in **(a)** absorption and **(b)** fluorescence spectra of Si-An induced by $^1O_2$ addition reaction, leading to the conversion from Si-An to Si-EP (black to red). Black and red arrows indicate absorption changes due to J-aggregate dissociation and anthracene endoperoxidation, respectively. 20:80 vol% methanol/PBS solution ([NaCl] = 110 mM), [Si-An] = 5 μM, [TMPyP4] = 10 μM, pathlength: 1 cm, and $\lambda_{ex}$ = 640 nm were used. 510−550 nm with a 100 mW cm$^{-2}$ xenon source was used to excite TMPyP4. **(b, inset)** Increase in fluorescence intensity at 666 nm divided by the absorbance at 640 nm versus irradiation time.

**X-Ray Crystal Structure of Si-An.** X-ray crystallographic analysis of Si-An was carried out to understand the correlation between the optical phenomena and packing pattern of Si-An aggregate. As shown in Figure 4-4, Si-rhodamine and anthracene moieties are all slipped stacked each other, and in particular, $\theta$ between the longitudinal axes of two Si-rhodamine molecules is determined to be 21.77° (Figure 4-4b). The X-ray crystallographic and the optical measurements well agree with the characteristics of J-aggregate: i) the angle of coplanar inclined transition dipoles ($\theta$) is in a range of $0° < \theta < 54.7°$; and ii) a sharp red-shifted absorption band with 2−3 nm Stokes shift (Figure 4-2). In addition, it is notable that the obtained crystal structure of Si-An contains ten water molecules and two chloride ions in one unite cell. This result implies that a presence of counterion plays an important role to maintain the slipped-stacked alignment of Si-An in crystal (Figure 4-4b). Indeed, bromide and iodide ion could induce J-aggregate of Si-An (Figures 4-5a and 4-5b), whereas exchanging counteranion to bulkier one such as hexafluorophosphate ($PF_6^-$) and tetraphenylborate ($BPh_4^-$) disabled any aggregate formation although hydrophobicity increased by coupling with lipophilic counterions (Figures 4-5c and 4-5b).

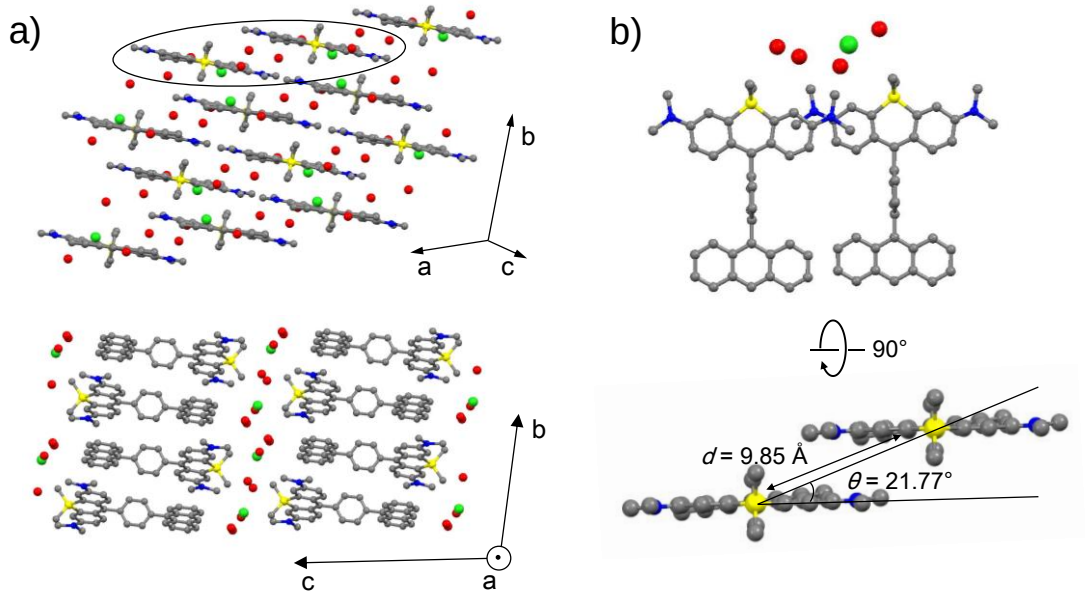


**Figure 4-4. (a)** Extended views of the crystal structure of Si-An aggregate. Carbon, silicon, nitrogen atoms, water molecule, and chloride ion are represented in gray, yellow, blue, red, and green, respectively. **(b)** Geometry of the two nearest Si-An molecules depicted in a black circle in Figure 4-4a.

From dynamic light scattering (DLS) measurements, there are at least two populations in the size of Si-An J-aggregate regardless of the concentration of Si-An: one in a range of 200−800 nm and another growing up to tens of μm during 2.5 hr incubation (Figure 4-6). Meanwhile, in the absence of NaCl or just after the addition of NaCl, the size of Si-An aggregate was undetectable, indicating that the size of H-aggregate is smaller than the detection limit of DLS (i.e. 1−3 nm).

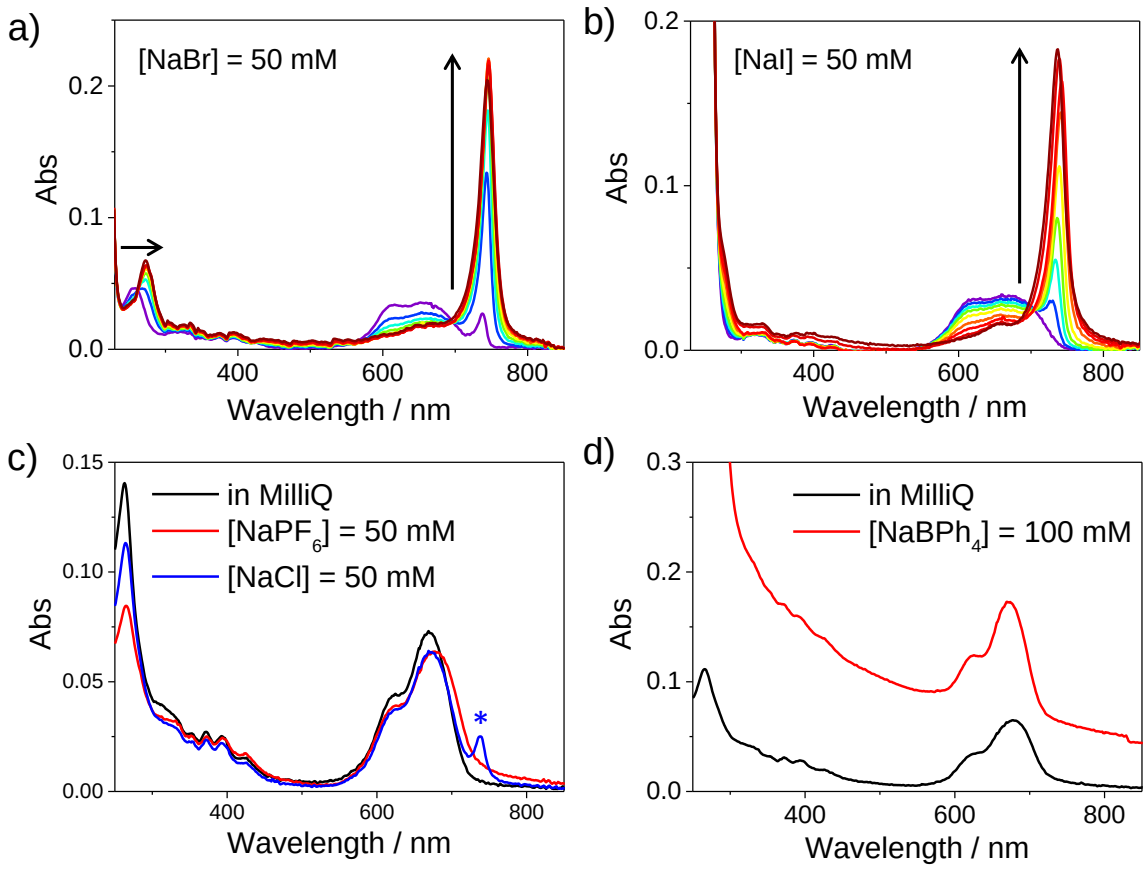


**Figure 4-5. (a, b)** Formation of Si-An J-aggregate in the presence of **(a)** [NaBr] and **(b)** [NaI] = 50 mM in MilliQ (violet to red color). Black arrows show the time dependent absorption changes, related to J-aggregate formation. [Si-An] = 5 μM and pathlength: 0.2 cm. **(c, d)** Absorption spectra of Si-An with **(c)** $PF_6^-$ and **(d)** $BPh_4^-$ in the absence and presence of additional salts after 1 hr incubation. In MilliQ, both absorption spectra of Si-An with $PF_6^-$ and $BPh_4^-$ (black lines) show a monomer-like shape, indicating that no H- and J-aggregate were formed because of the steric effect on the Si-rhodamine moiety. Further addition of $NaPF_6$ and $NaBPh_4$ did not induce spectral changes. On the other hand, by adding [NaCl] = 50 mM to Si-An with $PF_6^-$ in MilliQ solution, absorption band of J-aggregate could be monitored as depicted by a blue asterisk.

Concerning the previous studies on rhodamine aggregates, rhodamine derivatives tend to form antiparallel H-dimer (i.e. directing an opposite side each other) at $10^{-5}$ M.[28, 29] In particular, a dimethylsilyl group of Si-rhodamine may interrupt the parallel stacking of Si-rhodamine molecules. Overall, in the aqueous solution, Si-An presumably forms antiparallel H-dimer, whereas microcrystals of Si-An J-aggregate (200−800 nm) are formed in the presence of halide ion, and spontaneously gathered together, resulting in the secondary aggregates with a loss of J-aggregate characteristics.[30]

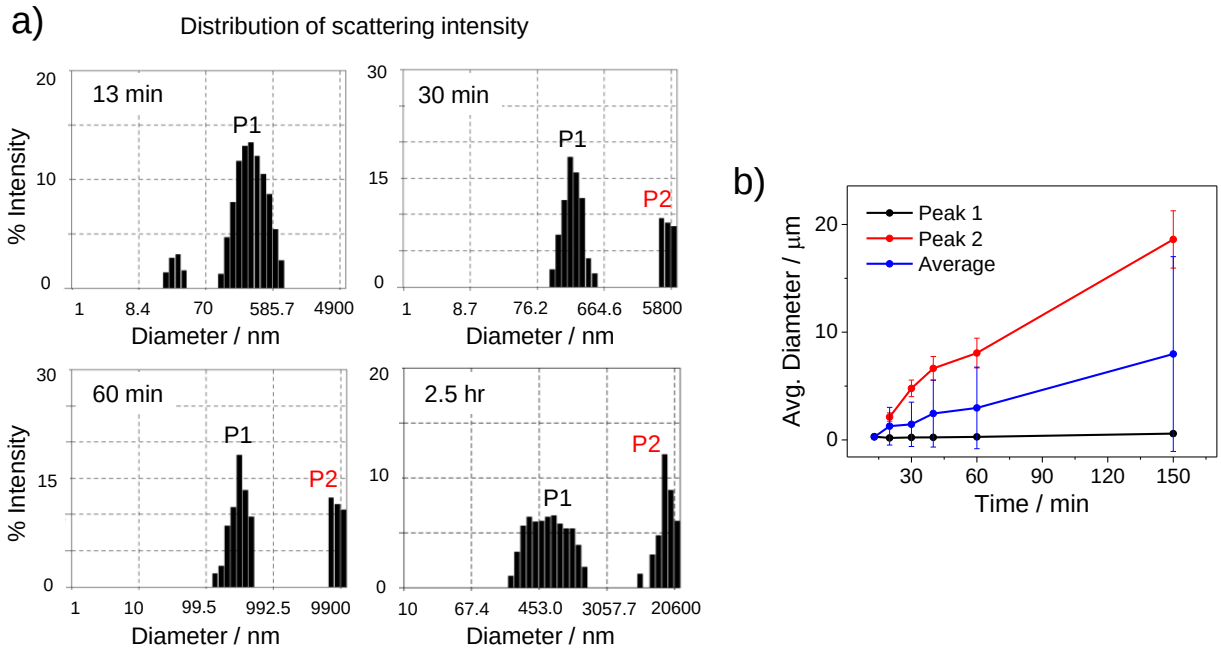


**Figure 4-6. (a)** DLS results of Si-An J-aggregate formation. **(b)** Time-dependent changes in the average diameter of two aggregates of peak 1 and peak 2 as written in Figure 4-6a. [Si-An] = 5 µM and [NaCl] = 50 mM in MilliQ. Before the addition of NaCl and during initial 13 min of incubation, scattering signal was never observed. Thus, Si-An H-aggregate formed in MilliQ is considered to be a few nm in size or smaller, indicating that H-dimer or oligomer is probably formed in the aqueous solution. On the other hand, there are at least two different J-aggregates in size (peak 1 and peak 2, black and red, respectively): In the case of peak 1, the monitored diameter is fluctuating between 200 and 600 nm, while peak 2 shows a gradual size increase from 2 to 18 µm during 150 min. The peak 1 and peak 2 are tentatively assigned to a unit of Si-An J-aggergate and the secondary aggregation of the J-aggregate unites, respectively.

**Photochemical Properties of Si-Rhodamine and Si-An Monomer in the Excited State.** To clarify relaxation dynamics of monomer, H-, and J-aggregates and the reason for fluorescence quenching of Si-An J-aggregate, transient absorption measurements were carried out. First, transient absorption spectra of Si-rhodamine the singlet excited state ($^1$Si-R*), Si-rhodamine in the triplet excited state ($^3$Si-R*), radical anion and cation of Si-rhodamine (Si-R$^{\bullet-}$ and Si-R$^{\bullet+}$, respectively) were measured by the fs-LFP, ns-LFP, and pulse radiolysis of Si-Me monomer. As shown in Figure 4-7, all of the transient spectra resemble those of the previously reported rhodamine derivatives, such as rhodamine123, with 20–80 nm red-shift. The transient extinction coefficients of Si-rhodamine in the excited state are summarized in Table 4-2.

Subsequently, transient absorption measurements of Si-An monomer were carried out using the fs-LFP. Figures 4-8a and 4-8b show transient absorption spectra of monomeric Si-An in MeOH with 650-nm excitation. As shown in Figure 4-8, transient absorption spectra of Si-An in the shorter wavelength region (Figure 4-8a) closely resemble the transient absorption spectrum of $^1$Si-R* (black, Figure 4-7a). However, radical species such as Si-R$^{\bullet-}$, Si-R$^{\bullet+}$, and radical cation of anthracene (An$^{\bullet+}$)[27] have not been observed for transient absorption spectra of Si-An. In addition,

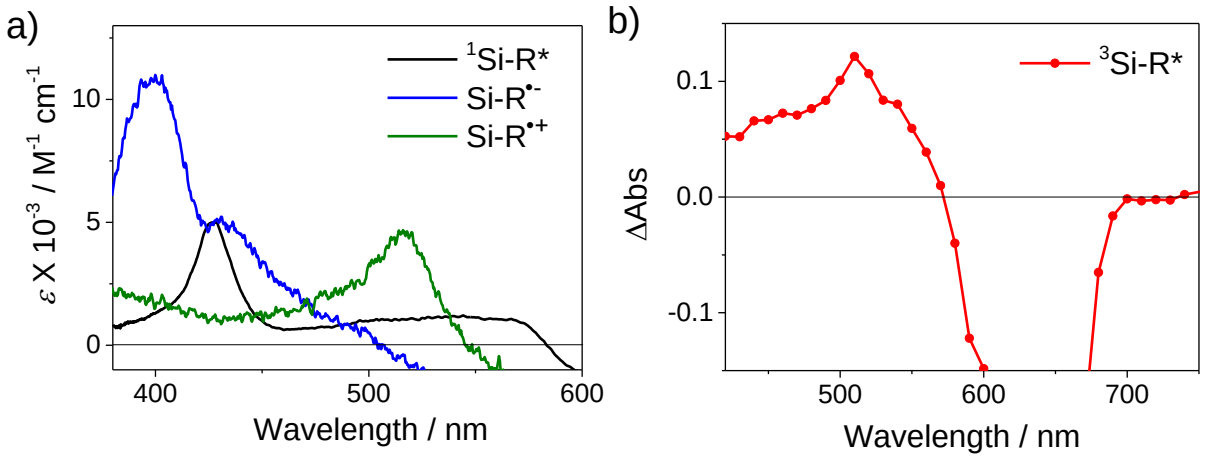


**Figure 4-7. (a)** Transient absorption spectra of $^1$Si-R* (black) in MeOH measured by fs-LFP, and Si-R$^{\bullet-}$ (blue) and Si-R$^{\bullet+}$ (green) in the aqueous solutions, measured by a pulse radiolysis, and **(b)** $^3$Si-R* in MeOH measured by ns-LFP in the presence of triplet energy donor, anthracene. Detailed measurement conditions are described in Experimental Section. Each transient extinction coefficient is summarized in Table 4-2.

**Table 4-2.** $\varepsilon$ of Si-rhodamine in the excited state.

| entry | max. $\lambda$ / nm | $\varepsilon$ / $M^{-1}$ $cm^{-1}$ | solvent | method |
|---|---|---|---|---|
| $^1$Si-R* | 427 | 5,000 | MeOH | fs-LFP |
| $^3$Si-R* | 510 | n.d.[†] | MeOH | ns-LFP |
| Si-R$^{\bullet-}$ | 399 | 10,900 | PBS buffer | Pulse radiolysis |
| Si-R$^{\bullet+}$ | 516 | 4,630 | PBS buffer | Pulse radiolysis |

[†]n.d.: Not determined.

the decay of $^1$Si-R* and ground state recovery occurred faster in Si-An than Si-Me. Hence, faster deactivation of $^1$Si-R* and weak fluorescence of Si-An than those of Si-Me is due to the increased internal conversion rate.

**Photochemical Properties of Si-An Aggregates in the Excited State.** Based on the results so far, it is assumed that the additional relaxation pathway becomes available in the Si-An J-aggregates due to the characteristic molecular alignment as depicted in Figure 4-4.

On the other hand, spectral shapes of transient absorption of Si-An aggregates were significantly different from monomeric Si-An. As for Si-An H-aggregate (Figures 4-8c and 4-8d), mainly three transient species were generated by 650-nm excitation: $\tau$ = 0.6 and 16.8 ps which show the maximum absorption at 430 and 510 nm, respectively (Figure 4-9a). It is notable that deactivation mechanisms of H-aggregate are varied depending on the characteristics of chromophore. Most accepted opinion for rhodamine H-dimer is ultrafast internal conversion among two exciton bands (i.e. sub-ps to ps-time scale), followed by intersystem crossing to form dimer in the triplet excited state, since a direct transition from the lower exciton state to the ground state is forbidden in H-aggregate.[12, 29] On the other hand, exciton trapping or excimer formation are also well-known relaxation pathways of H-aggregates.[31, 32] Because the transient absorption spectra of H-aggregate resemble the superposition of various transient species of Si-rhodamine (Figures 4-7a and 4-8c), here, the transient species with $\tau$ = 0.6 and 16.8 ps time constants were tentatively assigned to the exciton and ‘intermediate’ states, respectively (Figure 4-10).

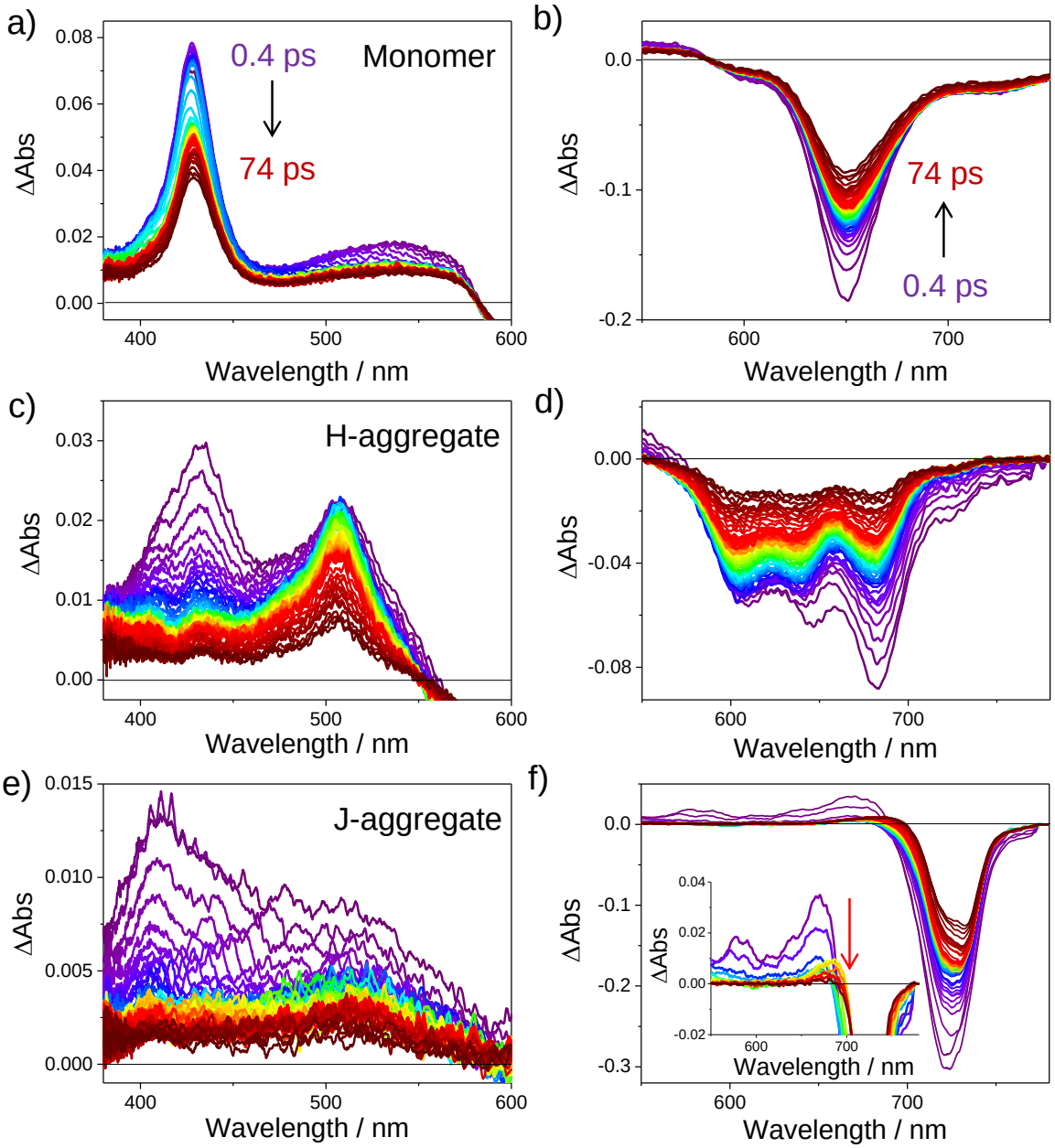


**Figure 4-8.** Transient absorption spectra monitored from 0.4 to 74 ps (violet to red) after a laser pulse during the fs-LFP of Si-An **(a, b)** monomer in methanol, and **(c, d)** H- and **(e, f)** J-aggregate in the aqueous solution. Si-An monomer and H-aggregate were excited at 650 nm, whereas J-aggregate was excited at 740 nm, near to the maximum of J-band. **(f, inset)** Enlarged transient absorption spectra at 0.4, 0.6, 0.8, 1.0, 2.5, 5.4, 10.4, 30, 100, 204, 404, 604, and 1004 ps after a laser pulse of fs-LFP of Si-An J-aggregate (violet to red). A red arrow shows a decrease in transient absorption of exction.

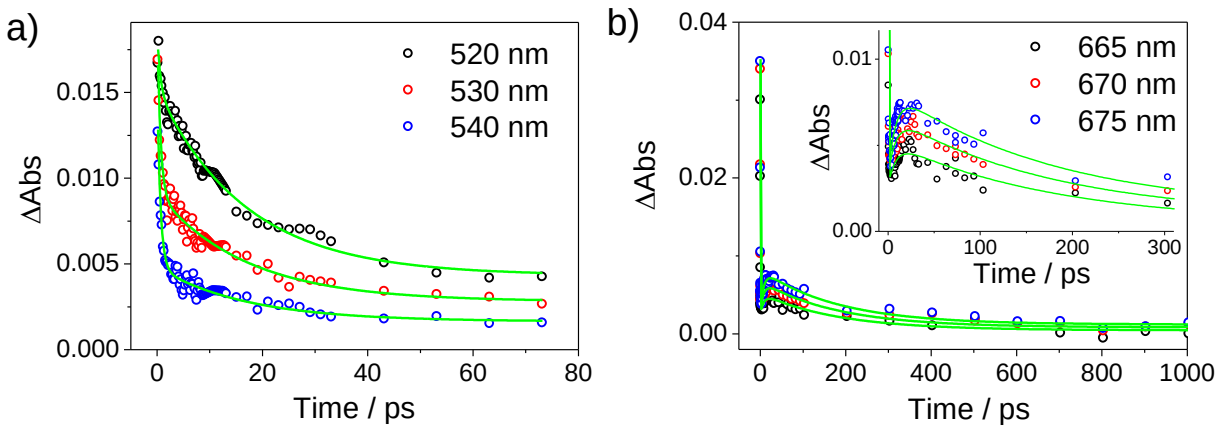


**Figure 4-9.** Time profiles of transient absorption decay (open circles) and multi-exponential global fitting results (green lines) of Si-An **(a)** H-aggregate and **(b)** J-aggregate from the transient absorption data as shown in Figures 4-8c and 4-8e, respectively. Biexponential function ($\tau$ = 0.6 and 16.8 ps) and triexponential function ($\tau$ = 0.3, 8.1, and 180 ps) are used for fitting the data of H-aggregate and J-aggregate, respectively. It should be noted that there is a long-lived component remained after the fitting of H-aggregate data (Figure 4-9a), approximately around a few hundreds ps.

For Si-An J-aggregate, broad positive transient absorption throughout 380−600 nm and negative transient absorption at around 730 nm were monitored upon a selective J-band excitation at 740 nm (Figures 4-8e and 4-8f). The negative transient absorption at 700−750 nm is from ground state bleaching of Si-An J-aggregate and a scattering signal induced by 740-nm excitation. Moreover, as shown in the inset of Figure 4-8f, another positive transient absorption was induced with three time constants: 0.3, 8.1, and 180 ps (Figure 4-9b). The red-shifting positive transient absorption with higher energy than the ground state bleaching signal has been reported by the previous studies on J-aggregate systems based on cyanine or porphyrin deritatives.[33] Similarly, 0.3, 8.1, and 180 ps are assigned to the internal conversion between two exciton bands, exciton-exciton annihilation (EEA) process, and decay of one-exciton state, respectively (Figure 4-10).[31, 34] Although there are no consensus time scale of EEA process, the author tentatively assigned 0.3 ps to the internal conversion from spectral similarities between two fastest transient species in H- and J-aggregates (Figures 4-8c and 4-8e). On the other hand, transient species of H-aggregate with $\tau$ = 16.8 ps at 510 nm was not obvious in J-aggregate. This

difference is also in accordance with the previous studies that J-aggregate is prone to transport the excitation energy as exciton migration rather than being relaxed through other intermediate states.[31, 32]

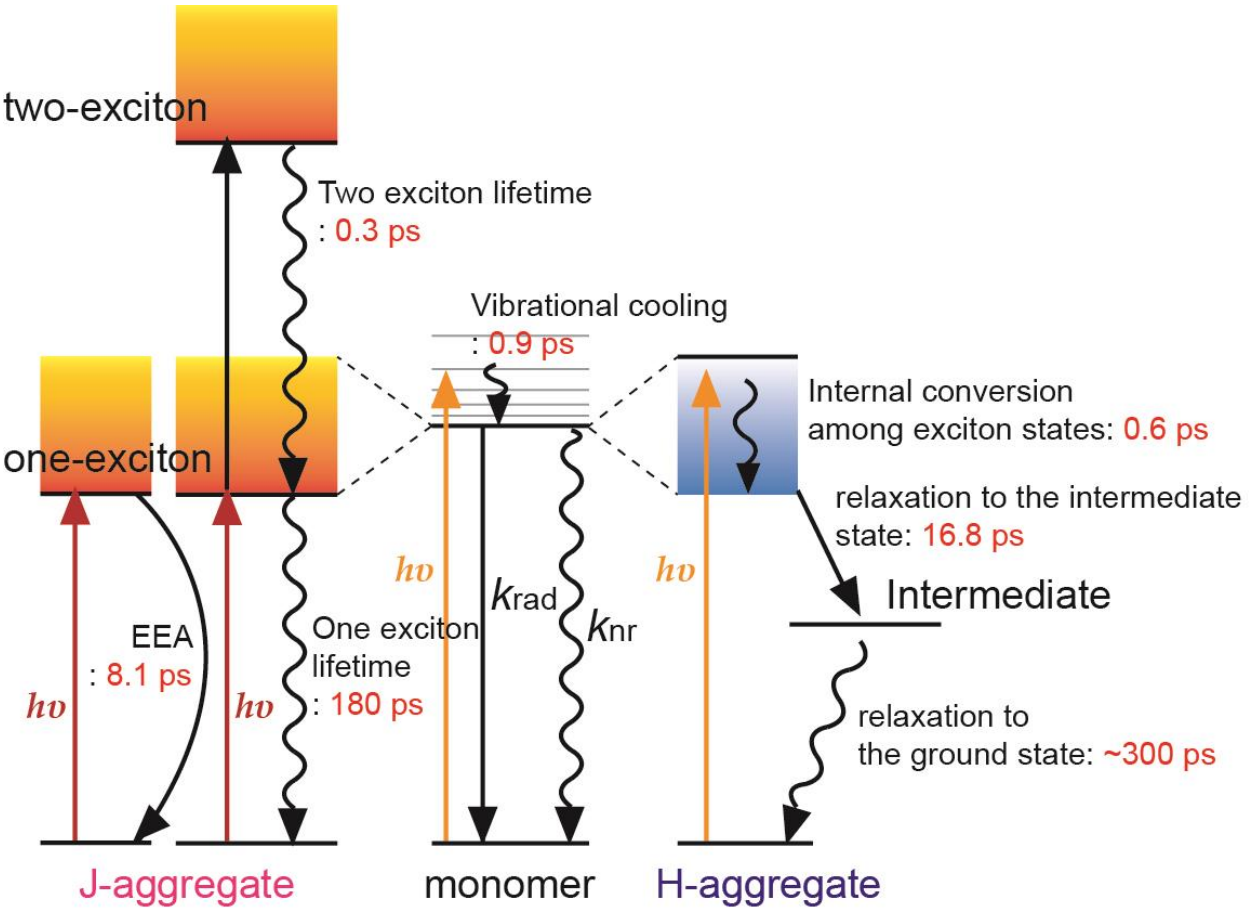


**Figure 4-10.** Plausible relaxation pathways and time constants of Si-An monomer, H-aggregate, and J-aggregate. Orange and red arrows indicate 650-nm and 740-nm excitations, respectively. The rates of radiative and non-radiative relaxation ($k_{rad}$ and $k_{nr}$, respectively, as shown above) of Si-Me and Si-An are summarized in Table 4-1. Intermediate state for H-aggregate relaxation may be either the triplet excited state or excimer state.

Taken together, fluorescence quenching upon J-aggregate formation is considered to originate from efficient EEA and probable intermolecular interactions between Si-rhodamine and

anthracene moieties du e to the reduced inter-chromophore distance upon J-aggregate formation.[35] Considering PET occurs in Si-rhodamine substituted by 9,10-dimethylanthracenyl group (see Figure 5-1) with lower oxidation potential than that of anthracene (1.05 and 1.19 V vs SCE, respectively),[36] introducing electron donating groups to 9-phenylanthracene will quench fluorescence of Si-An completely via the intermolecular PET in J-aggregate microcrystal.

**Application to Cell Imaging.** It was found that Si-An can penetrate the plasma membrane of a living cell and reside in mitochondria easily (Figure 4-11). This phenomenon is mostly due to +1 partial charge of Si-rhodamine and appropriate lipophilicity of Si-An, which shares the same mechanism with Si-DMA (see Chapter 5) One interesting aspect is that Si-An must have formed J-aggregate in the culture medium ($[Cl^-] \approx 120$ mM), but there was no difference in cell permeability and mitochondria localization between Si-An J-aggregate and Si-DMA H-aggregate.

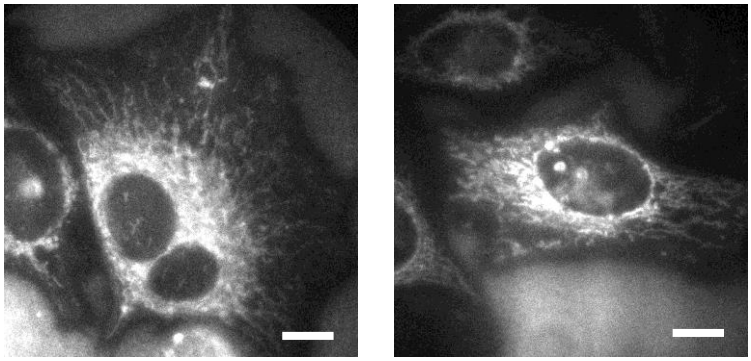

**Figure 4-11.** Si-An fluorescence image in HeLa cell. [Si-An] = 100 nM was incubated together with HeLa cell for 1 hr. $\lambda_{ex}$ = 640 nm and scale bar: 10 μm.

## Conclusion

The author has designed and thoroughly characterized H- and J-aggregate system of Si-rhodamine substituted by 9-phenylanthracenyl group using X-ray crystallography and transient absorption measurements. This study proposes a potential of phenylanthracenyl group as a versatile intramolecular template to align the target fluorophores depending on the presence of organic solvent and counter ions.[14] To conclude, provided that the anthracene moiety is properly

modified, a fluorophore with 9-phenylanthracenyl group will suggest a new paradigm of $^1O_2$ detection, for instance, a promising intracellular fluorescence probe with high S/N ratio achieved by complete fluorescence quenching via intermolecular PET.

## References


(1) (a) Verma, S.; Ghosh, H. N., *J. Phys. Chem. Lett.* **2012,** *3*, 1877; (b) Sartin, M. M.; Huang, C.; Marshall, A. S.; Makarov, N.; Barlow, S.; Marder, S. R.; Perry, J. W., *J. Phys. Chem. A* **2013,** *118*, 110.

(2) (a) Sagara, Y.; Komatsu, T.; Ueno, T.; Hanaoka, K.; Kato, T.; Nagano, T., *J. Am. Chem. Soc.* **2014,** *136*, 4273; (b) Yoon, S.-J.; Chung, J. W.; Gierschner, J.; Kim, K. S.; Choi, M.-G.; Kim, D.; Park, S. Y., *J. Am. Chem. Soc.* **2010,** *132*, 13675; (c) Huber, V.; Katterle, M.; Lysetska, M.; Würthner, F., *Angew. Chem., Int. Ed.* **2005,** *44*, 3147.

(3) (a) Hong, Y.; Lam, J. W. Y.; Tang, B. Z., *Chem. Soc. Rev.* **2011,** *40*, 5361; (b) Lee, Y.-D.; Lim, C.-K.; Singh, A.; Koh, J.; Kim, J.; Kwon, I. C.; Kim, S., *ACS Nano* **2012,** *6*, 6759.

(4) Ogawa, M.; Kosaka, N.; Choyke, P. L.; Kobayashi, H., *ACS Chem. Biol.* **2009,** *4*, 535.

(5) (a) Kasha, M.; Rawls, H. R.; Ashraf El-Bayoumi, M., *Pure Appl. Chem.* **1965**, *11*, 371; (b) Choi, S.; Bouffard, J.; Kim, Y., *Chem. Sci.* **2014,** *5*, 751.

(6) Kim, S.; Tachikawa, T.; Fujitsuka, M.; Majima, T., *J. Am. Chem. Soc.* **2014,** *136*, 11707.

(7) Lukinavičius, G.; Umezawa, K.; Olivier, N.; Honigmann, A.; Yang, G.; Plass, T.; Mueller, V.; Reymond, L.; Corrêa, I. R.; Luo, Z. G.; Schultz, C.; Lemke, E. A.; Heppenstall, P.; Eggeling, C.; Manley, S.; Johnsson, K., *Nat. Chem.* **2013,** *5*, 132.

(8) Sekiguchi, K.; Yamaguchi, S.; Tahara, T., *J. Phys. Chem. A* **2006,** *110*, 2601.

(9) Packard, B. Z.; Komoriya, A.; Toptygin, D. D.; Brand, L., *J. Phys. Chem. B* **1997,** *101*, 5070.

(11) (a) Würthner, F.; Kaiser, T. E.; Saha-Möller, C. R., *Angew. Chem., Int. Ed.* **2011,** *50*, 3376; (b) *J-Aggregates*; Kobayashi, T. Ed.; World Scientific; Singapore, 2011; (c) Fennel, F.; Wolter, S.; Xie, Z.; Plötz, P.-A.; Kühn, O.; Würthner, F.; Lochbrunner, S., *J. Am. Chem. Soc.* **2013,** *135*, 18722; (d) Ley, D.; Guzman, C. X.; Adolfsson, K. H.; Scott, A. M.; Braunschweig, A. B., *J. Am. Chem. Soc.* **2014,** *136*, 7809; (e) Supur, M.; Fukuzumi, S., *ECS J. Solid State Sci. Technol.* **2013,** *2*, M3051; (f) Eisele, D. M.; Knoester, J.; Kirstein, S.; Rabe, J. P.; Vanden Bout, D. A., *Nat. Nanotechnol.* **2009,** *4*, 658.

(11) (a) Giovanella, U.; Leone, G.; Ricci, G.; Virgili, T.; Lopez, I. S.; Rajendran, S. K.; Botta, C., *Phys. Chem. Chem. Phys.* **2012,** *14*, 13646; (b) Martinez, V.; Arbeloa, F.; Prieto, J.; Lopez, T.; Arbeloa, I., *J. Phys. Chem. B* **2004,** *108*, 20030; (c) del Monte, F.; Levy, D., *J. Phys. Chem. B* **1998,** *102*, 8036; (d) Busby, M.; Blum, C.; Tibben, M.; Fibikar, S.; Calzaferri, G.; Subramaniam, V.; De Cola, L., *J. Am. Chem. Soc.* **2008,** *130*, 10970.

(12) Nasr, C.; Liu, D.; Hotchandani, S.; Kamat, P. V., *J. Phys. Chem.* **1996,** *100*, 11054.

(13) (a) Kamino, S.; Horio, Y.; Komeda, S.; Minoura, K.; Ichikawa, H.; Horigome, J.; Tatsumi, A.; Kaji, S.; Yamaguchi, T.; Usami, Y.; Hirota, S.; Enomoto, S.; Fujita, Y., *Chem. Commun.*

**2010,** *46*, 9013; (b) Sanchez-Valencia, J. R.; Toudert, J.; Gonzalez-Garcia, L.; Gonzalez-Elipe, A. R.; Barranco, A., *Chem. Commun.* **2010,** *46*, 4372; (c) Lu, H.; Xue, Z.; Mack, J.; Shen, Z.; You, X.; Kobayashi, N., *Chem. Commun.* **2010,** *46*, 3565; Olivier, J.-H.; Widmaier, J.; Ziessel, R., *Chem. –Eur. J.* **2011,** *17*, 11709.
(14) (a) Hinoue, T.; Miyata, M.; Hisaki, I.; Tohnai, N., *Angew. Chem., Int. Ed.* **2012,** *51*, 155; (b) Sugino, M.; Hatanaka, K.; Araki, Y.; Hisaki, I.; Miyata, M.; Tohnai, N., *Chem.–Eur. J.* **2014,** *20*, 3069; (c) Sugino, M.; Hatanaka, K.; Miyano, T.; Hisaki, I.; Miyata, M.; Sakon, A.; Uekusa, H.; Tohnai, N., *Tetrahedron Lett.* **2014,** *55*, 732.
(15) (a) An, B.-K.; Gierschner, J.; Park, S. Y., *Acc. Chem. Res.* **2011,** *45*, 544; (b) Maggini, L.; Bonifazi, D., *Chem. Soc. Rev.* **2012,** *41*, 211.
(16) Koide, Y.; Urano, Y.; Hanaoka, K.; Terai, T.; Nagano, T., *ACS Chem. Biol*. **2011,** *6*, 600.
(17) Otwinowski, Z.; Minor, W., *Methods Enzymol.* **1997**, *276*, 307.
(18) Burla, M. C.; Caliandro, R.; Camalli, M.; Carrozzini, B.; Cascarano, G. L.; De Caro, L.; Giacovazzo, C.; Polidori, G.; Siliqi, D.; Spagna, R., *J. Appl. Cryst.* **2007,** *40*, 609.
(19) Crystal Structure ver 4.1, Crystal Structure Analysis Package, Rigaku Corporation (2000-2014). Tokyo 196-8666, Japan.
(20) Sheldrick, G. M., *Acta Crystallogr., A* **2008**, *64*, 112.
(21) Reisch, A.; Didier, P.; Richert, L.; Oncul, S.; Arntz, Y.; Mély, Y.; Klymchenko, A. S., *Nat. Commun.* **2014,** *5*, 4089.
(22) Ferguson, M.; Beaumont, P.; Jones, S.; Navaratnam, S.; Parsons, B., *Phys. Chem. Chem. Phys.* **1999,** *1*, 261.
(23) Jayson, G. G.; Parsons, B. J.; Swallow, A. J., *J. Chem. Soc., Faraday Trans. 1* **1973,** *69*, 1597.
(24) Hare, P. M.; Price, E. A.; Stanisky, C. M.; Janik, I.; Bartels, D. M., Solvated Electron Extinction Coefficient and Oscillator Strength in High Temperature Water. *J. Phys. Chem. A.* **2010,** *114*, 1766.
(25) (a) Uno, S.-N.; Kamiya, M.; Yoshihara, T.; Sugawara, K.; Okabe, K.; Tarhan, M. C.; Fujita, H.; Funatsu, T.; Okada, Y.; Tobita, S.; Urano, Y., *Nat. Chem.* **2014,** *6*, 681; (b) Lukinavicius, G.; Reymond, L.; D'Este, E.; Masharina, A.; Gottfert, F.; Ta, H.; Guther, A.; Fournier, M.; Rizzo, S.; Waldmann, H.; Blaukopf, C.; Sommer, C.; Gerlich, D. W.; Arndt, H.-D.; Hell, S. W.; Johnsson, K., *Nat. Methods* **2014,** *11*, 731; (c) Kushida, Y.; Nagano, T.; Hanaoka, K., *Analyst* **2015,** DOI: 10.1039/C4AN01172D.
(26) Urano, Y.; Kamiya, M.; Kanda, K.; Ueno, T.; Hirose, K.; Nagano, T., *J. Am. Chem. Soc.* **2005,** *127*, 4888.
(27) Kim, S.; Fujitsuka, M.; Majima, T., *J. Phys. Chem. B* **2013,** *117*, 13985.
(28) Halterman, R. L.; Moore, J. L.; Mannel, L. M., *J. Org. Chem.* **2008,** *73*, 3266.
(29) Setiawan, D.; Kazaryan, A.; Martoprawiro, M. A.; Filatov, M., *Phys. Chem. Chem. Phys.* **2010,** *12*, 11238.
(30) Li, A.; Zhao, L.; Hao, J.; Ma, R.; An, Y.; Shi, L., *Langmuir* **2014,** *30*, 4797.

(31) Fink, R. F.; Seibt, J.; Engel, V.; Renz, M.; Kaupp, M.; Lochbrunner, S.; Zhao, H.-M.; Pfister, J.; Würthner, F.; Engels, B., *J. Am. Chem. Soc.* **2008,** *130*, 12858.
(32) Lindquist, R. J.; Lefler, K. M.; Brown, K. E.; Dyar, S. M.; Margulies, E. A.; Young, R. M.; Wasielewski, M. R., *J. Am. Chem. Soc.* **2014,** *136*, 14912.
(33) (a) Minoshima, K.; Taiji, M.; Misawa, K.; Kobayashi, T., *Chem. Phys. Lett.* **1994,** *218*, 67; (b) Johnson, A. E.; Kumazaki, S.; Yoshihara, K., *Chem. Phys. Lett.* **1993,** *211*, 511; (c) Sytina, O. A.; van Stokkum, I. H. M.; van Grondelle, R.; Groot, M. L., *J. Phys. Chem. A* **2010,** *115*, 3936.
(34) Marciniak, H.; Li, X.-Q.; Würthner, F.; Lochbrunner, S., *J. Phys. Chem. A* **2010,** *115*, 648.
(35) Beckers, E. H. A.; Meskers, S. C. J.; Schenning, A. P. H. J.; Chen, Z.; Würthner, F.; Marsal, P.; Beljonne, D.; Cornil, J.; Janssen, R. A. J., *J. Am. Chem. Soc.* **2005,** *128*, 649.
(36) Fukuzumi, S.; Ohkubo, K.; Okamoto, T., *J. Am. Chem. Soc.* **2002,** *124*, 14147.

**Supporting Figure.** Synthesis of Si-An

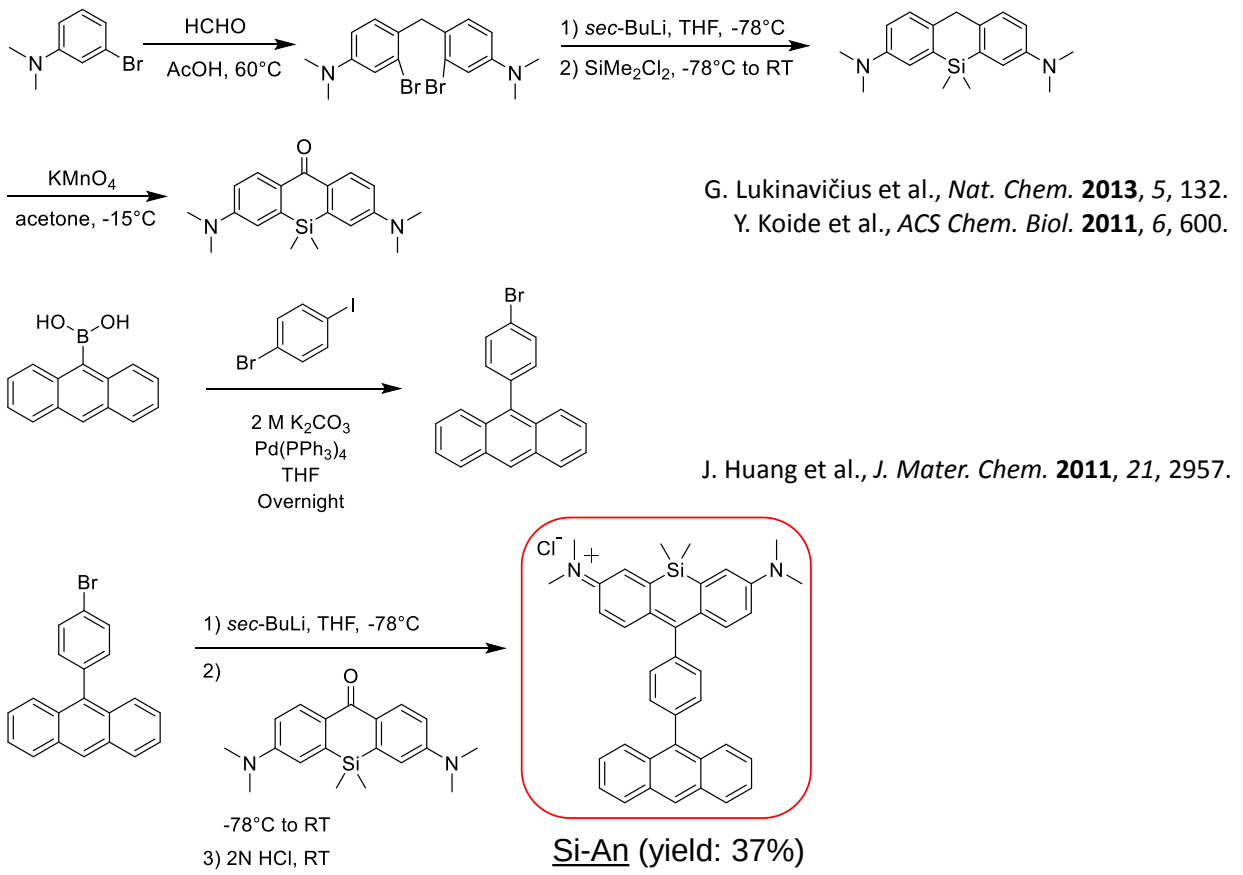

# Chapter 5. Far-Red Fluorescence Detection of Intracellular Singlet Oxygen: Si-Rhodamine and Dimethylanthracene Dyad

## Introduction

Singlet oxygen ($^1O_2$) is molecular oxygen in the lowest excited state.[1] In biological and medical studies, $^1O_2$ is of a particular importance because of its key role in photodynamic therapy (PDT), an emerging anticancer treatment using photoirradiation and photosensitizers (Sens).[2] In PDT, $^1O_2$ is the first molecule immediately generated after photoirradiation in the aerobic condition, resulting in direct oxidation of nearby biomolecules, shutdown of the vascular system, and finally inflammation or immune reaction to tumor tissue.[3] Hence, investigating the formation and diffusion dynamics of $^1O_2$ is highly necessary to understand anticancer mechanisms of PDT at the molecular level. Cytotoxic mechanisms of Sens in PDT can be explained as type-I and type-II.[1,2] Type-II photosensitization includes all kinds of reactions where the excited Sens is quenched by a collision with oxygen in the ground state ($^3O_2$). Meanwhile, in type-I photosensitization, adjacent molecules (except $^3O_2$) quench the excited Sens often through electron transfer. Upon photoirradiation of injected photosensitizers, a majority of $^1O_2$ is produced via triplet−triplet intermolecular energy transfer from Sens in the triplet excited state ($^3$Sens*) to $^3O_2$ (eq 1).

$$^3\text{Sens}^* + {}^3O_2 \rightarrow \text{Sens} + {}^1O_2 \qquad (1)$$

This is a typical reaction of $^1O_2$ formation via type-II photosensitization. On the other hand, it is notable that the superoxide anion can be generated by either type-I, type-II, or secondary biological processes after photoirradiation, such as mitochondrial damage. As summarized in previous reviews,[2,4−6] the superoxide anion often acts as a “primary” reactive oxygen species (ROS) because they can be further converted into other ROS such as $H_2O_2$ and $^1O_2$ through various biological reactions.

To detect $^1O_2$, phosphorescence measurement has been generally used in PDT.[1,7,8] From time-resolved phosphorescence measurement, intracellular $^1O_2$ lifetime ($\tau_\Delta$) is found to be varied from a few tens of nanoseconds to 3 μs, depending on the experimental conditions.[2,7,9] Undoubtedly, monitoring $^1O_2$ with its luminescence provides the most direct information on $^1O_2$ formation and

further behaviors. Unfortunately, however, the intensity of phosphorescence is typically much weaker than that of fluorescence. In addition, to obtain time trajectories of $^1O_2$ with good signal-to-noise ratio, the exchange of intracellular liquid from $H_2O$ to $D_2O$ is mostly required. Thus, realtime mapping (e.g., subsecond acquisition time) of $^1O_2$ formation at the subcellular spatial resolution is extremely challenging using the currently available near-IR detector and under physiological conditions.[10,11] Considering the current problems, the fluorescence detection of $^1O_2$ is ultimately required to trace $^1O_2$ formation and its dynamics at the subcellular level under physiological conditions (i.e. $H_2O$-based culture media).

Despite continuous efforts on the development of a fluorescent probe for $^1O_2$ detection,[12–15] merely a few cases enabled imaging $^1O_2$ in living cells.[16–20] Moreover, Singlet Oxygen Sensor Green (SOSG), a widely used commercial $^1O_2$ probe, exhibits several critical weak points in live cell imaging: self-oxidation upon photoirradiation, cell impermeability (or nonspecific staining at the relatively high incubating concentration, 10 μM), and a necessity of green excitation ($\lambda_{abs}$ = 508 nm) where a cell autofluorescence signal is induced.[21,22] Before this study, only Song et al.[16] and Dai et al.[17] succeeded in monitoring intracellular $^1O_2$ produced during photoirradiation of Sens using the fluorescent probe based on europium complexes. Surprisingly, however, there was no adequate $^1O_2$ fluorescence probe to monitor intracellular $^1O_2$ during PDT at the subcellular level. The drawbacks of SOSG and lack of a suitable and successful organic probe for $^1O_2$ mapping have inspired us to develop a new far-red fluorescent probe for the $^1O_2$ detection.

In this study, the author have synthesized a far-red fluorescent probe of $^1O_2$, composed of 9,10-dimethylanthracene (DMA) and silicon-containing rhodamine (Si-rhodamine) moieties, namely, Si-DMA (Figure 5-1). Recently, Si-rhodamine has been actively applied for the detection of various biological substances[23–26] and super-resolution imaging both in vitro and in vivo.[27] In light of the previous works, it was affirmed that Si-rhodamine is a promising far-red chromophore for the intracellular $^1O_2$ mapping. Here, Si-rhodamine is found to exhibit 3 times lower quantum yield of $^1O_2$ generation ($\Phi_\Delta$) than that of 2,7-dichlorofluorescein, a chromophore of SOSG. Furthermore, Si-DMA can selectively reside in mitochondria and provide an instantaneous response to intracelluar $^1O_2$. Compared to the previously reported intracellular $^1O_2$ probes,[16–19] Si-DMA shows outstanding results to visualize intracellular $^1O_2$ in real-time and to distinguish different localizations of Sens and photosensitization mechanisms.

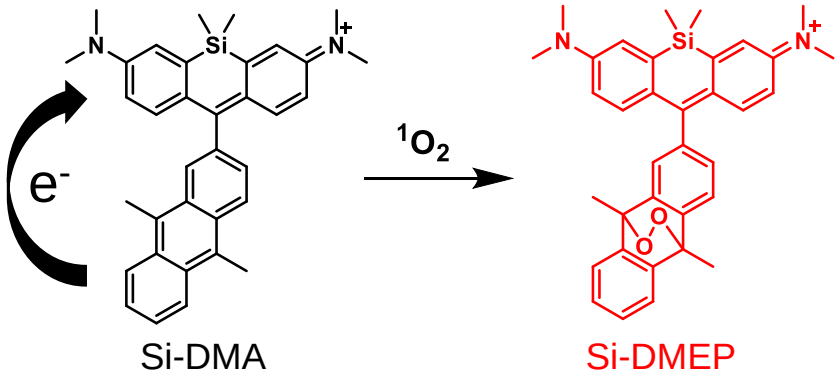


**Figure 5-1.** Chemical structures of Si-DMA and its enperoxidized product (Si-DMEP).

**Experimental Section**

**Materials.** All chemical reagents and solvents used for the synthesis were purchased from Sigma-Aldrich Chemical Co., Tokyo Chemical Industries, Nacalai Tesque, and Wako Pure Chemical, and used as received. 2-Methylbenzene-substituted Si-rhodamine (Si-Me, Figure 4-1) was synthesized according to the previous report by Koide et al.,[23] and Si-DMA was synthesized as described in Supporting Figure. Si-DMA and Si-Me were stored in dimethyl sulfoxide (DMSO) at −20°C in the dark. The following Sens were chosen for living cell experiments: 5-aminolevulinic acid (5-ALA, Sigma-Aldrich), a precursor of heme, and tetra-(*N*-methyl-4-pyridyl)porphyrin (TMPyP4, Tokyo Chemical Industries). SOSG, CellROX Green, MitoTracker Green FM, and Dextran 10000 MW labeled by Alexa Fluor 488 or Alexa Fluor 647 (A488- and A647-dextran, respectively) were purchased from Molecular Probes and used for $^1O_2$ and ROS detection, mitochondrial and lysosomal markers, respectively.

**Characterizations of Si-DMA.** $^1$H-nucler magnetic resonance (NMR) spectrum and high resolution mass spectrum (HRMS) of Si-DMA were measured by a JEOL ESC400 (400 MHz) and LTQ Orbitrap XL™ Hybrid Ion Trap-Orbitrap Mass Spectrometer with electron spray ionization (ESI). NMR chemical shift, *J*-value and integral were calculated using Delta Ver.5 software (JEOL).

**Ex Vivo Steady-State Measurements.** Without a notation, all bulk spectroscopic measurements were performed in methanol at the spectroscopic grade or pH 7.5 phosphate buffered saline (PBS) solution without $Ca^{2+}$ and $Mg^{2+}$ (both purchased from Nacalai Tesque). Ground-state absorption and fluorescence emission spectra were measured using a Shimadzu UV-3100 and Horiba FluoroMax-4, respectively. Bulk irradiation was performed using a xenon source (LAX-C100, Asahi Spectra) and band-pass filter (BA510-550, Olympus).

**Selectivity Tests.** The aggregate formation decreases the effective concentration of the dye, which slows the reaction rate of Si-DMA. Thus, 5 μM solution of Si-DMA in the 1:1 mixture of MeOH and pH 7.4 PBS buffer solution was first prepared to make sure Si-DMA is present as a monomer. Next, 10 mM solutions of various ROS ($^1O_2$, $O_2^{\bullet-}$, $H_2O_2$, HOCl, ROO$^\bullet$, and $^\bullet$OH) were prepared by adding reagents as follows:

1. $^1O_2$: 10 mM NaOCl and 10 mM $H_2O_2$
2. $O_2^{\bullet-}$: 10 mM $KO_2$
3. $H_2O_2$: 30% $H_2O_2$ solution diluted to 10 mM
4. HOCl: 10 mM NaOCl
5. ROO$^\bullet$: 10 mM 2, 2-azobis (2-amindinopropane) dihydrochloride
6. $^\bullet$OH: 1 mM $FeSO_4 \bullet 7H_2O$ and 10 M $H_2O_2$.

Under vigorous magnetic stirring, Si-DMA solutions containing each ROS were kept in dark for 10 min. Subsequently, corresponding absorption and fluorescence spectra of the samples were measured.

**Time-Resolved Phosphorescence Measurement.** The samples of Rose Bengal and Si-Me were prepared in 1:9 DMSO/MeOH solution in a 1 × 1 × 4 $cm^3$ quartz cell. The second-harmonic oscillation (532 nm, 4 ns fwhm, 5.0 mJ $cm^{-2}$ $pulse^{-1}$) from a Q-switched Nd:YAG laser (Continuum, Surelite II-10) was used for the excitation light. The photoinduced luminescence from the sample cell was collected with quartz lenses, passed through a monochromator, and then introduced into a near-IR photomultiplier tube module (Hamamatsu Photonics, H10330A-75). After being amplified by a 350 MHz amplifier unit (Stanford Research, SR445A), the output of the photomultiplier was sent to a gated photon counter (Stanford Research, SR400) under direct control from a PC via the GPIB interface. To measure the lifetime of $^1O_2$, the signals were

accumulated (five repetitions) by changing the delay time from 0 to 50 μs with a gate width of 1.0 μs.

**Cells and Cell Culture.** HeLa cells and RAW 264.7 macrophages were kindly provided by the RIKEN BRC through the National Bio-Resource Project of the MEXT, Japan, and Prof. Tsuyoshi Nishi (SANKEN, Osaka University), respectively. Without a notation, cell experiments carried out in this study were performed using HeLa cells. HeLa cells and RAW 264.7 macrophages were cultivated in Dulbecco's modified Eagle medium (D6429, Sigma) supplemented with 10% fetal bovine serum (10099-141, Gibco) at 37 °C in a humidified incubator under 5% $CO_2$.

**Protocols of the Dye Staining.** For the treatment requiring the incubation shorter than 2 hr, serum-free culture medium with HEPES 20 mM was used, while serum-containing culture medium with HEPES 20 mM was used for the treatment longer than 4 hours to maintain cell viability. To label mitochondria, MitoTracker Green FM was diluted to 50 nM and incubated for 30 min, whereas Dextran 10,000 MW labeled by Alexa Fluor 488 or Alexa Fluor 647 (A488- and A647-dextran, respectively) were diluted to 50 μg ml-1 and incubate for 24 hr to stain lysosomes. In addition, the quick protocol to introduce CellROX Green was followed as provided by Molecular Probe®. Diluted Si-DMA and Si-Me were incubated for 30 min to 2 hr depending on the experiments. To deliver photosensitizers (Sens), 150 μg ml-1 5-ALA or 10 μM TMPyP4 were incubated for 4 and 24 hr, respectively. As reported previously, 5-ALA is converted to protoporphyrin IX (PpIX) in mitochondria, and this biosynthesis was confirmed by fluorescence emission of PpIX.

**KillerRed Expression.** A general protocol of Lipofectamine® 2000 (Invitrogen) was followed to express KillerRed vector. In detail, 2 × 105 HeLa cells were subcultured in 35-mm glass bottom dish, which became approximately 50% confluent on the following day. Subsequently, the complex solution of lipofectamine reagent-DNA vector was prepared by mixing 6 μl of Lipofectamine® 2000 and 7 μl of pKillerRed-dMito vector (0.5 μg mL-1, Evrogen, cat.# FP964) in Opti-MEM solution (Gibco), and incubating it for 20 mins at RT. 300 μl of the complex solution was added to growth media, and incubated it for 24 hrs. Expression of KillerRed was confirmed by monitoring KillerRed fluorescence using a wide-field microscope as shown in

Figure 5-8c.

**Live Cell Imaging.** To monitor fluorescence increase of Si-DMA during photoirradiation of Sens, an Olympus IX81 inverted fluorescence microscope and a 640 nm CW laser (Coherent) were used to irradiate Sens and monitor the probe simultaneously. A 35 mm μ-dish with a glass bottom (ibidi) with HeLa cells was excited through an oil objective (Olympus, PlanApo 100×/1.40 oil). The emission image was collected with the same objective and recorded by an EMCCD camera (Roper Scientific, Evolve 512) through a dichroic beamsplitter (Semrock, Di02-R635) and a band-pass filter (Chroma, HQ690/70). During data acquisition, the same environment as an incubator (37 °C and 5% $CO_2$) was maintained using a Chamlide TC (Live Cell Instrument). Pseudocolor fluorescence images were prepared by reprocessing the obtained movie file using OriginPro 9.1 (OriginLab) and ImageJ.

To confirm the localization of dyes, in particular, cellular organelles, an objective scanning confocal microscope (PicoQuant, MicroTime 200) coupled with an Olympus IX71 inverted fluorescence microscope was used. An 8-well μ-slide (ibidi) with HeLa cells was excited at two wavelengths, 405/640 nm or 485/640 nm, using a pulsed laser (PicoQuant) controlled by a PDL-800B driver (PicoQuant) through an oil objective (Olympus, UPlanSAPo 100x/1.40 oil/0.17/FN26.5). Subsequently, the emission was collected with the same objective and detected by a single photon avalanche photodiode (Micro Photon Devices, PDM 50CT and 100CT) through a beam splitter (90% transmission, 10% reflection), suitable band-pass filters, and 75 μm pinhole for spatial filtering to reject out-of-focus signals. Two images for green and red channels were further processed to obtain a merged image using OriginPro 9.1 (OriginLab) and ImageJ.

## Results and Discussions

**Synthesis and Optical Properties of Si-DMA.** As proposed by Nagano et al.[23] and Johnsson et al.,[27] Si-containing xanthone was first synthesized, and then connected to 2-bromo-9,10-dimethylanthracene, which is a reactive site for $^1O_2$, resulting in Si-DMA (19% yield). $^1O_2$-induced conversion of Si-DMA to Si-DMEP is illustrated in Figure 5-1. Detailed synthesis description and characterization can be found in Supporting Figure.

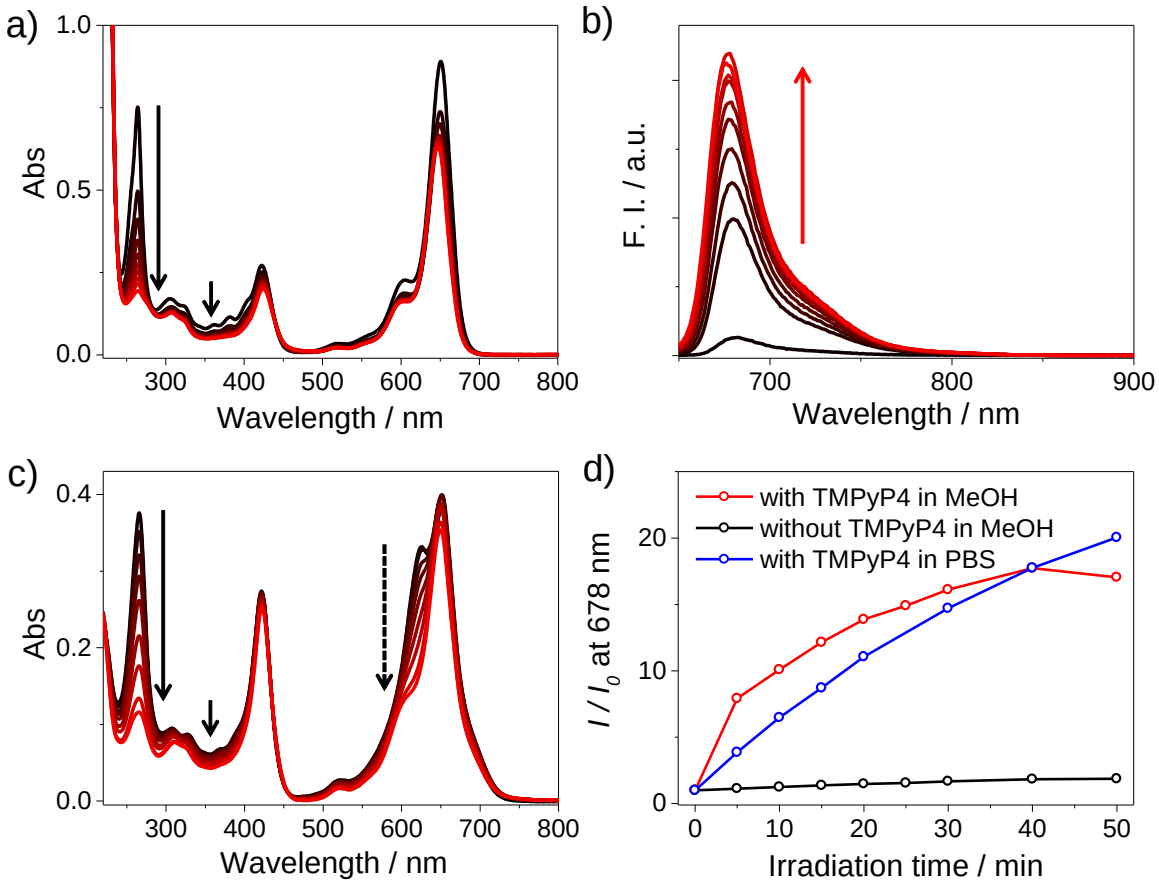


**Figure 5-2.** Absorbance and fluorescence changes of Si-DMA in methanol **(a,b)** and in PBS solution **(c)** upon photoirradiation of codissolved TMPyP4 for 50 min (black to red). Black arrows in **(a,c)** indicate absorbance changes due to peroxidation of DMA (bold lines) and dissociation of H-aggregates (dashed lines), while a red arrow in **(b)** shows fluorescence increase during 50 min irradiation. **(d)** Si-DMA fluorescence increase during 50 min photoirradiation. [Si-DMA] = 50 μM, [TMPyP4] = 5 μM, and 510−550 nm irradiation at 0.07 W $cm^{-2}$ with magnetic stirring was used for $^1O_2$ formation.

Figure 5-2 shows time-dependent changes in absorbance and fluorescence of Si-DMA upon photoirradiation of coincubated TMPyP4. In the absence of $^1O_2$, the excited Si-rhodamine is quenched by photoinduced electron transfer (PET) from DMA, resulting in dim fluorescence ($\Phi_{fl}$ = 0.01 in methanol). Polarity-dependent fluorescence quenching and transient absorption spectra of Si-DMA support that Si-DMA is indeed deactivated by PET (Figure 5-3). This intramolecular PET and subsequent charge recombination process in Si-DMA are considered to be similar to the

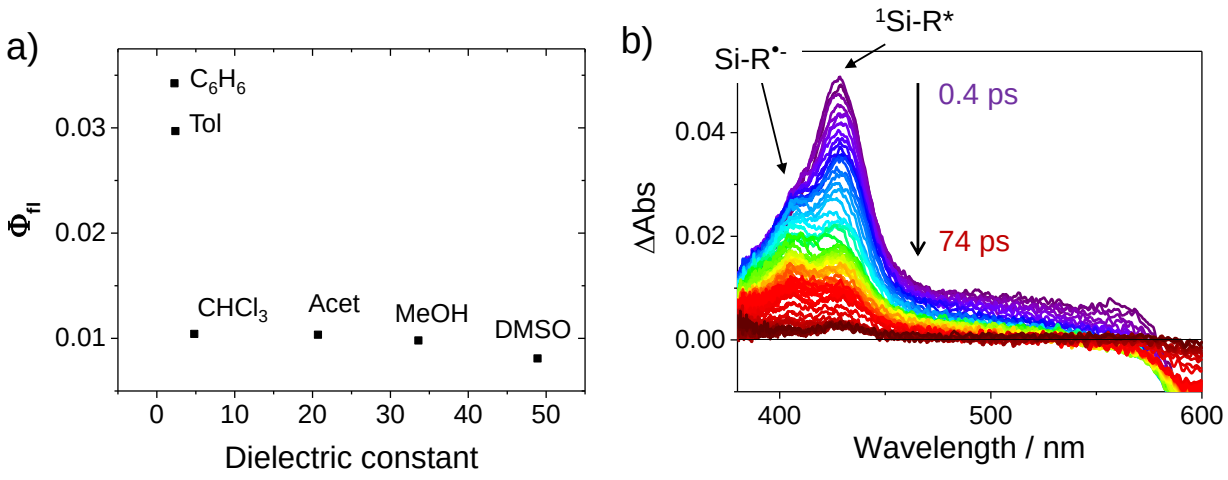


**Figure 5-3. (a)** Fluorescence quantum yield ($\Phi_{fl}$) dependence on dielectric constants of the solution. In order to confirm that fluorescence quenching of Si-DMA is due to PET, $\Phi_{fl}$ of Si-DMA in six solvents with different dielectric constants were measured. As a result, $\Phi_{fl}$ = 0.034, 0.030, 0.010, 0.010, 0.010, and 0.008 in benzene, toluene, chloroform, acetone, methanol, and DMSO, respectively, were determined, showing a good dependence with their dielectric constants. **(b)** Transient absorption spectra measured from 0.6 to 74 ps (violet to red) after a laser pulse during the fs-LFP of Si-DMA in MeOH. [Si-DMA] = 61 μM in MeOH which has the absorbance of 0.9 at 650 nm with a 0.2 cm pathlength cell. $\lambda_{ex}$ = 650 nm.

previously reported xanthene−anthracene dyads.[22,28] Furthermore, Si-DMA converts into bright form (Si-DMEP, $\Phi_{fl}$ = 0.17 in methanol) by reacting with $^1O_2$ and forming endoperoxide on the center ring of DMA because PET from DMA to Si-rhodamine is prohibited (Figure 5-1). Approximately, 18-fold increase in fluorescence was observed in MeOH (Figures 5-2b and 5-2d, red), accompanying a disappearance of anthracene absorbance (black arrows, Figure 5-2a). Similar spectral changes were observed when $^1O_2$ was induced by a chemical catalyst. In addition, it has been reported that some anthracene derivatives, such as arylanthracene and alkynylanthracene, undergo a reversible reaction with $^1O_2$ upon increasing temperature, that is, a formation of endoperoxide and release of $O_2$.[29] Nonetheless, the DMA moiety in Si-DMA does not release $O_2$ after endoperoxidation but is probably prone to be decomposed at temperatures above 70 °C, which is much greater than that at physiological conditions.[21]

Interestingly, Si-DMA is found to form H-aggregates in the aqueous solution (Figure 5-2c). This is because substituting an anthracene moiety reduces the hydrophilicity of Si-DMA as compared to Si-Me, which is a monomer in PBS solution at the same concentration (5 μM). A blue-shifted absorption peak at 625 nm is clear evidence to indicate the H-aggregates of rhodamine chromophores.[30–32] This blue-shifted shoulder gradually decreases as Si-DMEP forms (Figure 5-2c, red arrow), implying that endoperoxide formation at the anthracene ring disrupts a stacking of rhodamine fluorophores. In Figure 5-2d, the slower rate of Si-DMEP formation in the case of H-aggregates compared to that of monomeric Si-DMA is presumably caused by (1) a decrease in the absolute chromophore concentration due to the aggregate formation and (2) necessity of aggregate dissociation by (or for) reacting with $^1O_2$. A similar result is also obtained in the presence of chemically prepared $^1O_2$. Furthermore, a larger fluorescence increment observed in PBS solution (22-fold) than that in MeOH (18-fold) is probably due to additional fluorescence quenching upon H-aggregate formation before photoirradiation. Overall, both monomeric and H-aggregates of Si-DMA can react to $^1O_2$, while Si-DMEP does not favor the aggregate formation due to a loss of anthracene planarity.

**Evaluations of Si-DMA as a $^1O_2$ Probe.** Si-DMA is tested to confirm whether it can respond to $^1O_2$ quantitatively and selectively without self-oxidation of the dye. First, both Si-DMA monomer and H-aggregates show linear fluorescence increase versus [$^1O_2$] generated by $NaClO/H_2O_2$ (Figure 5-4a). Furthermore, Si-DMA exhibits a good selectivity toward $^1O_2$ out of other ROS, which agrees with the previous anthracene based $^1O_2$ probes (Figure 5-4b).[12,13,16] In addition, no significant fluorescence decrease was observed in various ROS solutions, indicating chromophore stability of Si-DMA against ROS.

As briefly mentioned earlier, one critical weak point of SOSG is its non-negligible $^1O_2$ generation due to the excitation of the chromophore moiety.[22] Even though most of the SOSG molecules are deactivated via ultrafast intramolecular PET ($k_{PET}$ = 9.7 × $10^{11}$ s−1), trivial impurities of initially bright SOSG, such as nonsubstituted fluorescein (~0.3%)[33] or peroxidized SOSG molecules, cannot be deactivated via PET and are in charge of $^1O_2$ generation upon continuous photoirradiation.[21,22,33] To observe $^1O_2$ produced during PDT that often requires prolonged photoirradiation from a few minutes to hours, self-oxidation of the dye by light excitation should be avoided. In order to confirm that Si-rhodamine is an appropriate

chromophore as a $^1O_2$ probe, $\Phi_\Delta$ of Si-Me was determined using time-resolved phosphorescence measurement (Figure 5-5). Using Rose Bengal as a reference ($\Phi_\Delta$ = 0.76 in MeOH),[34] $\Phi_\Delta$ of Si-Me is around 0.02. This value is considered to reflect the possible maximum $\Phi_\Delta$ of Si-DMA and Si-DMEP when deactivation pathways via PET is completely blocked. Furthermore, $\Phi_\Delta$ of Si-Me is 3 times smaller than that of 2,7-dichlorofluorescein, a fluorophore of SOSG ($\Phi_\Delta$ = 0.06).[22]

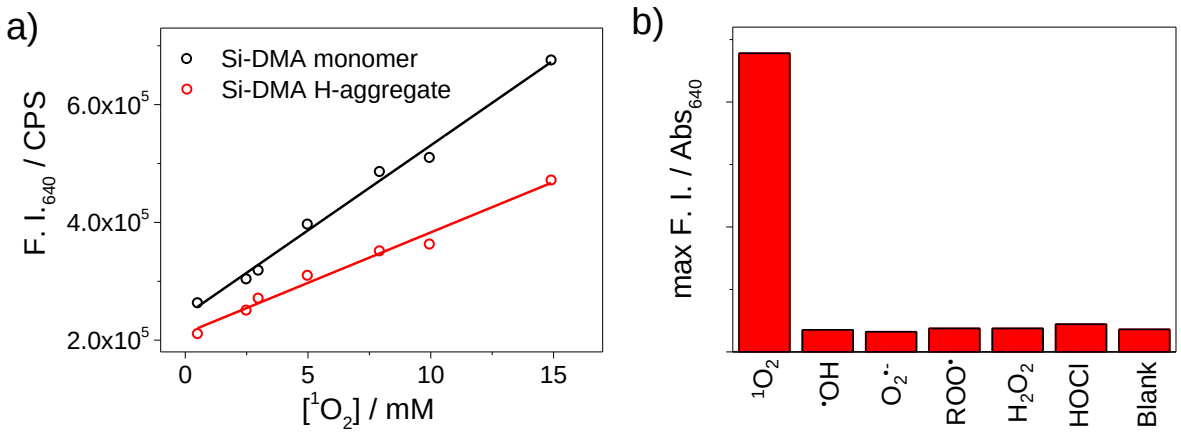


**Figure 5-4. (a)** Fluorescence increase of Si-DMA monomer (black) and H-aggregate (red) in the solutions of DMSO:MeOH:Tris-Buffer 1:49:50 and DMSO:Tris-Buffer 1:99, respectively, upon $^1O_2$ generated by NaOCl/$H_2O_2$ reaction ([Si-DMA] = 5 μM). Linear fittings of the obtained data show a good correlation between Si-DMA response and [$^1O_2$]. Since the absolute fluorescence intensity of Si-DMA H-aggregates is smaller than that of monomer, 1-nm wider slit width of excitation wavelength was used during measurements to decrease signal-and-noise ratio of the aggregate case. From the linear fittings, the slope of Si-DMA monomer is approximately 1.7 times larger than that of Si-DMA H-aggregates. This result implies that Si-DMA H-aggregates provides a significant fluorescence increase only when comparably larger amount of $^1O_2$ is present. **(b)** Selectivity of Si-DMA toward $^1O_2$ among other ROS. Maximum fluorescence intensity divided by the absorbance at 640 nm was compared. [Si-DMA] = 5 μM and [ROS] = 10 mM in 1:1 MeOH/PBS solution, stirred for 10 min.

Finally, Si-DMA is considered to be fairly photostable, as shown in Figure 5-2d (black). During 50 min irradiation, no photobleaching is observed in the absence of photosensitizer. In

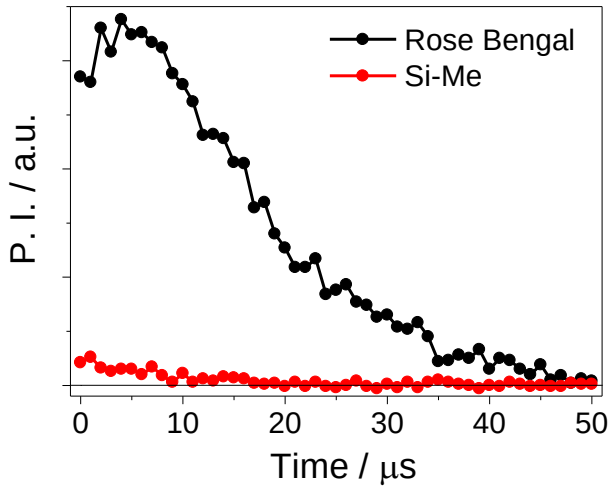


**Figure 5-5.** Time profiles of $^1O_2$ phosphorescence intensity (P.I.) of Rose Bengal (black) and Si-Me (red) observed at 1280 nm ($\lambda_{ex}$ = 532 nm at 5.0 mJ cm$^{-2}$ pulse$^{-1}$) in 1:9 DMSO/MeOH solution. Both samples were prepared to have the same absorbance of 0.5 at 532 nm (pathlength = 1 cm). [Rose Bengal] = 21.5 μM and [Si-Me] = 250 μM.

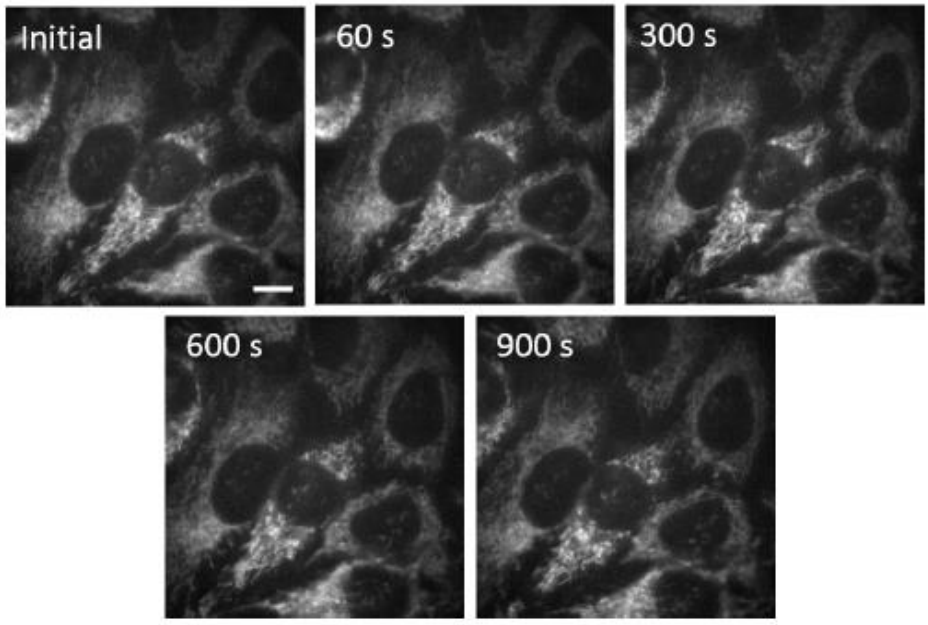


**Figure 5-6.** Photostability of Si-DMA in HeLa cells upon continuous 640-nm irradiation at 0.6 W cm$^{-2}$. [Si-DMA] = 100 nM, Scalr bar: 10 μm.

addition, this photostability is maintained when Si-DMA is introduced to HeLa cells (Figure 5-6). This result is in accordance with the previous study on Si-rhodamine.[24]

**Mitochondrial Localization of Si-DMA.** Positive net charge of a dye, such as that of rhodamine 123 (R123)[35,36] and lipophilic cyanine cation, JC-1,[37,38] facilitates its mitochondrial accumulation due to mitochondrial membrane potential.[39] Here, the author found that Si-DMA can reside in mitochondria with high selectivity (Figure 5-7). The long, thin, and branched fibrillar fluorescence image of Si-DMA clearly proves its selective localization in mitochondria.[40] In addition, it does not have a strong preference to reside in mitochondria around the nucleus or edge of the cell, different from 5-ALA-derived PpIX (discussed later). On the other hand, concentrations higher than 1 μM seem to result in nonspecific localization and even higher than 5 μM shows cytotoxicity determined by vacuole formation and cell detachment. The latter effect is due to the loss of mitochondrial membrane potential upon excess loading of Si-DMA.[39] Hence, in this study, [Si-DMA] less than 100 nM was chosen to ensure the homogeneous, selective, and nontoxic staining of mitochondria (Figures 5-7a and 5-7b).

It is notable that connecting DMA to Si-rhodamine does not affect its intrinsic localization, whereas azo-benzene-substituted Si-rhodamine is mainly localized in the lysosome.[26] Meanwhile, SOSG, a trianionic molecule, stains HeLa cells in a nonspecific and inefficient manner. More importantly, mitochondria are the main target organelles in PDT because mitochondrial actions and dysfunctions are closely related to the programmed cell death.[41−43] Thus, a selective mitochondrial staining of Si-DMA indeed takes advantage of visualizing intracellular $^1O_2$ particularly during PDT.

**Fluorescence Detection of Intracellular $^1O_2$: Dependent on the Localization of Sens.** To deliver Sens selectively to mitochondria, the author chose 5-ALA, which is a commercialized PDT drug as a precursor for the biosynthesis of PpIX.[2,42,44−46] The excess amount of biosynthesized PpIX, which could not be bound to Fe to form heme, is accumulated in mitochondria, and this phenomenon readily happens especially in cancer cells. When the localization of PpIX derived by [5-ALA] = 150 μg $mL^{-1}$ was traced, the synthesized PpIX was found to be initially localized in mitochondria and soon diffused to the cytoplasm (Figure 5-8).

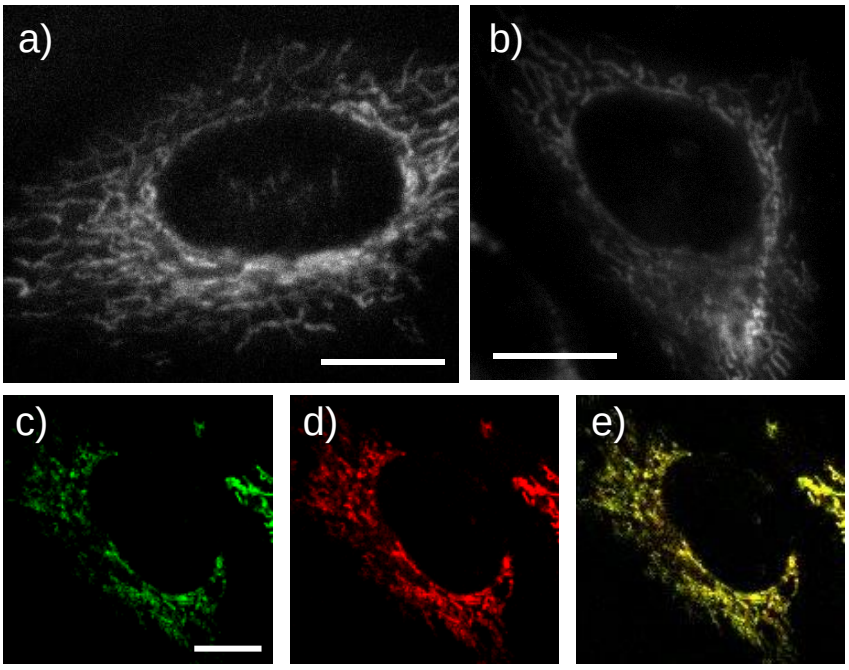


**Figure 5-7.** HeLa cells stained with [Si-DMA] = **(a)** 20 and **(b)** 100 nM for 1 h. **(c–e)** Colocalization test of Si-DMA in mitochondria. **(c)** MitoTracker Green and **(d)** [Si-DMA] = 100 nM. Clear colocalizations of two dyes are observed in the merged image **(e)**. Intensities of each image have been adjusted to obtain a clear picture. Scale bar = 10 μm.

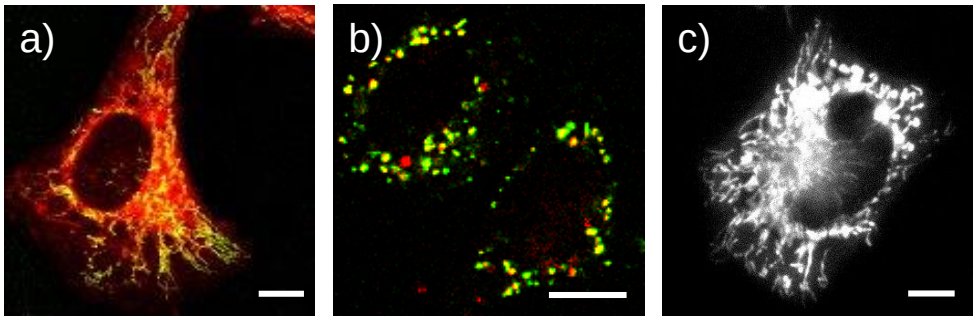


**Figure 5-8.** Intracellular localizations of Sens. **(a)** Fluorescence of MitoTracker Green, 5-ALA-derived PpIX, and merged points are depicted in green, red, and yellow, respectively. **(b)** Fluorescence of A488-dextran, TMPyP4, and merged points are depicted in green, red, and yellow, respectively. **(c)** Fluorescence of KillerRed monitored after 24 h transfection of mitochondria-targeted KillerRed vector. Scale bar = 10 μm.

In particular, PpIX is predominantly localized in the perinuclear region as reported previously.[42,47,48] In light of the previous reports, 5-ALA was incubated for 4 h in order to maximize the amount of synthesized PpIX.[44,45]

Figure 5-9a shows reprocessed pseudocolor images of Si-DMA fluorescence in HeLa cells during 640 nm irradiation of PpIX. It is clearly shown that photoirradiation of PpIX induces an increase of Si-DMA fluorescence rapidly (within 10 s) and more significantly in the perinuclear region as compared to the cell edge. The same tendency is observed when the incubation concentration of Si-DMA is increased to 100 nM. Here, an evident fluorescence increase along the mitochondria structure provides a much clearer picture of intracellular $^1O_2$ generation as compared to the previous $^1O_2$ probes with 5-ALA-derived PpIX.[15,17]

It should be confirmed that the fluorescence increase of Si-DMA shown in Figure 5-9a is caused by $^1O_2$ generation and not by environmental changes of mitochondria upon PDT. To confirm, a cell permeable $^1O_2$ quencher, sodium azide ($NaN_3$) was added, and monitored approximately 4−6-fold deceleration in the initial rates of fluorescence increase (Figure 5-10). Furthermore, mitochondrial environmental changes, such as viscosity, did not influence the fluorescence of Si-DMA (Figure 5-11a).

Subsequently, another type-II Sens that exhibits nonmitochondrial localization is introduced to monitor fluorescence response of Si-DMA. TMPyP4 is one of the frequently used type-II Sens in a model study of PDT because it is water soluble and can bind to a DNA aptamer, finally delivered to the nucleus of cancer cells.[49−51] Prior to coincubating with Si-DMA, it was confirm that TMPyP4 first resides in lysosomes after 24 h incubation (Figure 5-8b). Next, 640 nm irradiation triggered lysosomal rupture, followed by relocalizations of TMPyP4 to the cytoplasm and nucleus. Relocalization of Sens in lysosomes is a well-known phenomenon in PDT, which maximizes a cytotoxic effect of $^1O_2$ from dispersed Sens molecules.[43,52]

Since fluorescence of TMPyP4 is not intense enough ($\Phi_{fl}$ = 0.047 in $H_2O$)[53] and Q-band absorbance at 640 nm is relatively small, lysosomal rupture events cannot be monitored by TMPyP4 fluorescence with the same photoirradiation and detection conditions used to image Si-DMA. Thus, lysosomes were additionally stained using A647-dextran to observe intracellular events and fluorescence changes of Si-DMA simultaneously with the excitation of TMPyP4. As depicted by the white arrows in Figure 5-9b, lysosomes containing A647-dextran and TMPyP4 are distinguishable due to their granular structures and strong fluorescence. Upon 640 nm

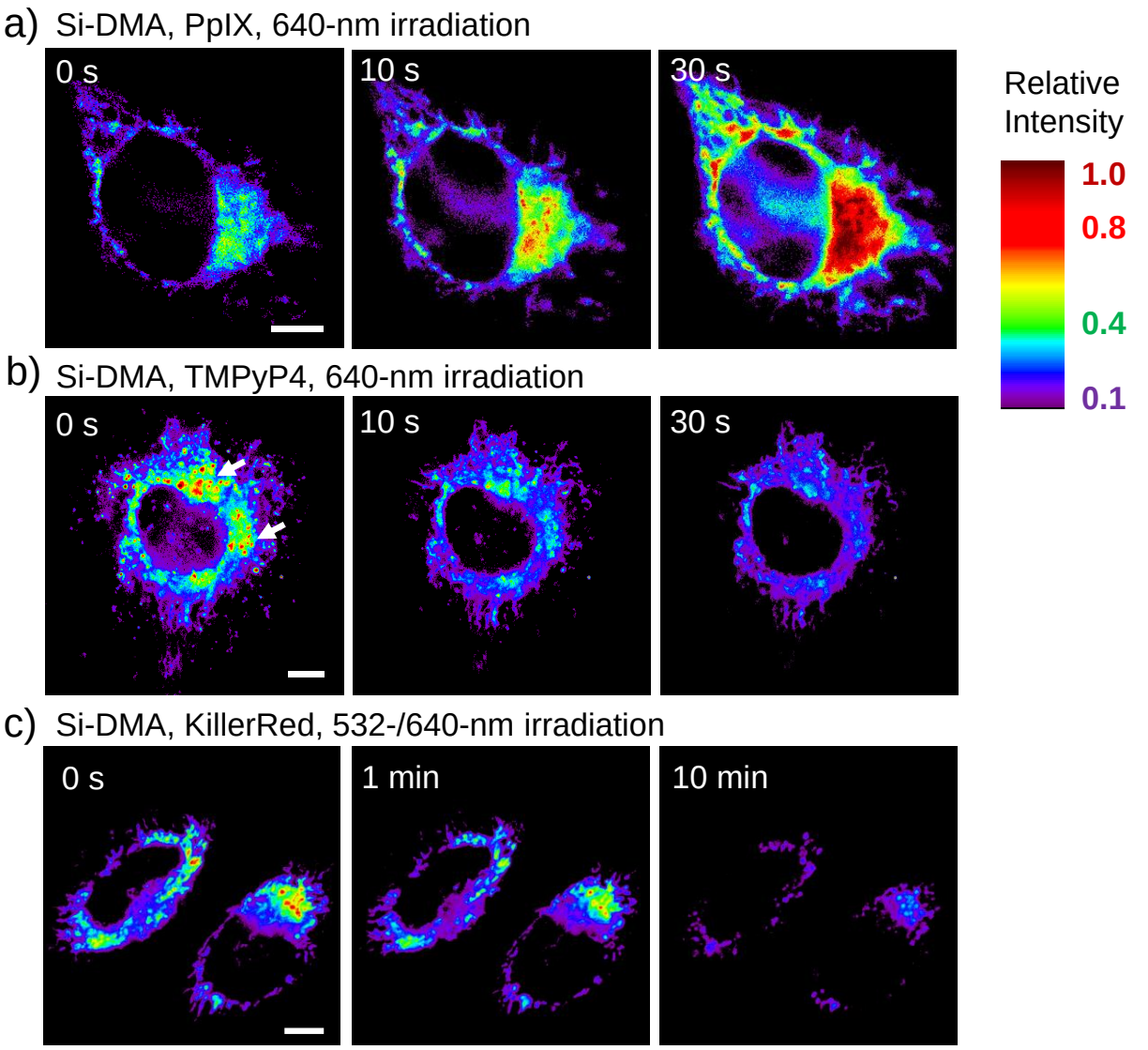


**Figure 5-9.** Pseudocolor fluorescence images of HeLa cells with Si-DMA and **(a)** 5-ALA-induced PpIX, **(b)** 24 h incubated TMPyP4 and lysosome marker (A647-dextran), and **(c)** mitochondria-targeted KillerRed. Granular structures indicated by white arrows in **(b)** are lysosomes that are ruptured within 10 s by TMPyP4 irradiation. [Si-DMA] = 25 nM was incubated for 1 h in the HeLa cells containing corresponding Sens. **(a,b)** One-color irradiation at 640 nm (0.6 W $cm^{-2}$) was used to generate $^1O_2$ and monitor Si-DMA fluorescence simultaneously. Meanwhile, two-color irradiation was required to excite Si-DMA and KillerRed **(c)**; 0.5 and 0.6 W $cm^{-2}$ were used for 532 and 640 nm irradiation, respectively. Scale bar = 10 μm.

irradiation for 10 s, lysosomal rupture and TMPyP4 diffusion substantially occur. However, fluorescence of Si-DMA does not increase even after TMPyP4 relocalization (Figure 5-9b).

In short, the heterogeneous fluorescence increase shown in Figure 5-9a is considered to reflect the localization of PpIX because Si-DMA is localized in mitochondria almost homogeneously over the cell body (Figure 5-8a). In contrast, Si-DMA does not react with $^1O_2$ generated by TMPyP4 (Figure 5-9b), which changes its location from lysosome to cytoplasm and nucleus upon photoirradiation. Taken together, Si-DMA can respond to only mitochondrial-originating $^1O_2$. This is because of the short diffusion distance of intracellular $^1O_2$ (at longest, approximately 300 nm) in aqueous solution.[9]

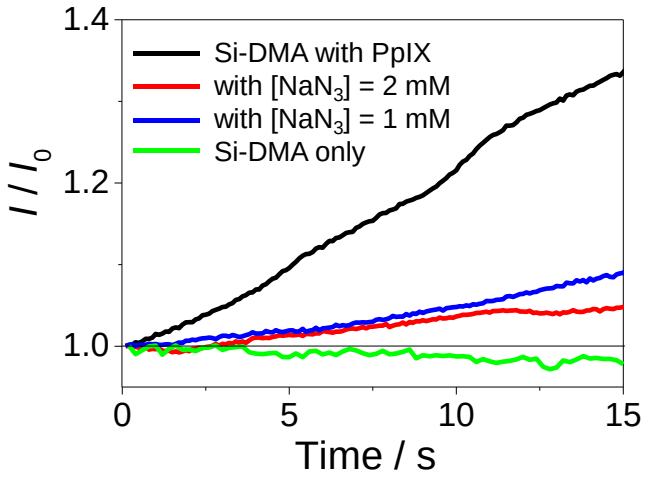


**Figure 5-10.** Fluorescence changes of Si-DMA during 15 s of 640 nm irradiation at 0.6 W $cm^{-2}$ with PpIX induced by 5-ALA (black), with the addition of [$NaN_3$] = 2 mM (red), 1 mM (blue), and Si-DMA without Sens and $NaN_3$ (green). All data are obtained by averaging mean count changes monitored in 5−8 cells.

**Fluorescence Detection of Intracellular $^1O_2$: Dependent on the Type of Sens.** In the previous section, 5-ALAderived PpIX and TMPyP4 were used, and both are standard type-II Sens with high $\Phi_\Delta$ (0.54 and 0.74, respectively).[34] As a comparison, KillerRed was chosen as an exemplary case of photosensitizing protein, and it could be expressed selectively in mitochondria (Figure 5-

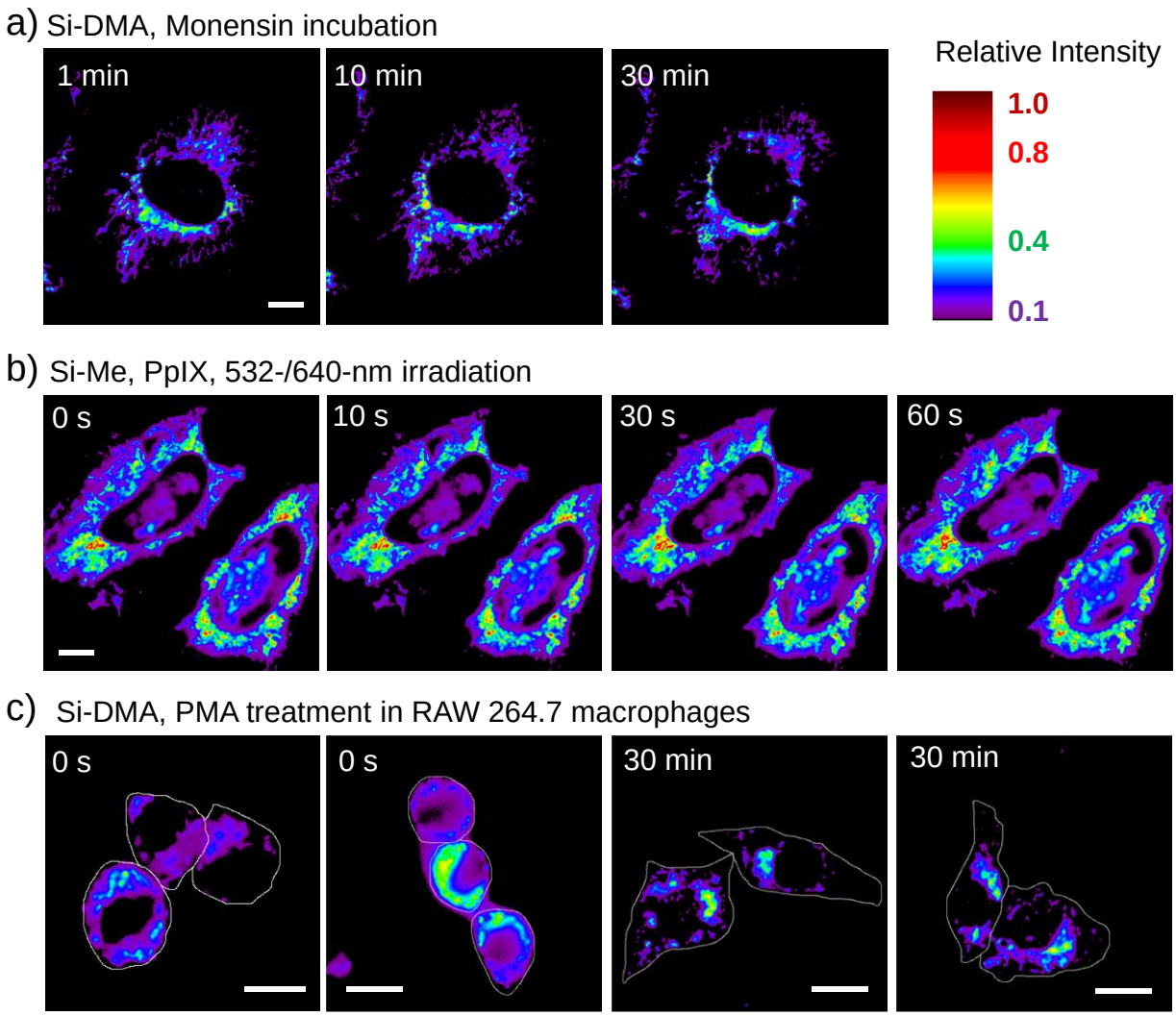


**Figure 5-11.** Pseudocolor fluorescence images of **(a)** Si-DMA with monensin incubation and **(b)** Si-Me with PpIX under 532- and 640-nm irradiation in HeLa cells, and **(c)** Si-DMA before and after PMA treatment in RAW 264.7 macrophages. [Si-DMA] = 25 nM or [Si-Me] = 100 nM were incubated for 1 hr. Scale bar: 10 μm. 0.6 W $cm^{-2}$ was used for 640-nm irradiation to image Si-DMA, whereas 0.5 and 0.005 W $cm^{-2}$ were used for 532- and 640-nm irradiation, respectively, for Si-Me imaging as well as PpIX excitation. It is notable that fluorescence of Si-Me is so strong compared to of Si-DMA that approximately 100 times weaker excitation was required to prevent signal saturation. In Figure 5-11c, the shape of RAW 264.7 macrophages are depicted by white line.

8c).[54] Upon photoirradiation, the chromophore of KillerRed, the *N*-acylimine group composed of Gln-Tyr-Gly, is excited and subsequently quenched by one electron reduction from the adjacent amino acid residue, resulting in the radical anion of the chromophore (type-I photosensitization). Its characteristic phototoxicity originates from the presence of a water-filled channel reaching the chromophore of KillerRed.[55,56] Thus, KillerRed can generate a superoxide anion by electron transfer from the radical anion of its chromophore to $^3O_2$.

Pseudocolor images of Si-DMA and KillerRed fluorescence ($\lambda_{em}$ = 610 nm),[54] collected by the same detection channel (655−725 nm), are shown in Figure 5-9c. Since $\lambda_{abs}$ of KillerRed is 585 nm,[54] two-color excitation at 532 and 640 nm is used to excite KillerRed and Si-DMA, respectively. In fact, KillerRed fluorescence is not negligible compared to that of Si-DMA (red spots in the 0 s image of Figure 5-9c). During 10 min photoirradiation, however, only photobleaching of both species was observed without fluorescence increase of Si-DMA (Figures 5-9c). As shown in Figure 5-4b, Si-DMA can only respond to $^1O_2$ but not superoxide, hydrogen peroxide, and other ROS. Thus, this result implies that the amount of $^1O_2$ generated by KillerRed is far insufficient to induce a conversion of Si-DMA to Si-DMEP even though KillerRed is colocalized in mitochondria. On the other hand, photoirradiation of KillerRed causes relocalization and DNA binding of CellROX Green, which infers the generation of oxygen radical species. Generation of a superoxide anion in a proportional manner upon photoirradiation of KillerRed is in good accord with the previous report.[57]

**$^1O_2$ Diffusion Distance and Its Concentration Affect Fluorescence Increase of Si-DMA.** To understand different responses of Si-DMA to three Sens (Figure 5-9), the total cumulative [$^1O_2$] during photoirradiation of Sens was firstly considered. The extent of PDT cytotoxic effects, so-called PDT dose, is influenced by three factors: light, oxygen, and drug.[7] Here, the same light intensity of 640 nm irradiation (except KillerRed) was used, and there is only a slight difference in Q-band absorbance of PpIX and TMPyP4. Furthermore, the previous study found merely a marginal difference of $\Delta pO_2$ between mitochondria or endosomes and air-saturated medium in HeLa cells.[44,58] Overall, nearly identical light doses and homogeneous $pO_2$ over a whole cell infer that light dose and [$^3O_2$] are not conclusive factors to derive the different results in Si-DMA fluorescence, as shown in Figure 5-9.

Next, the effective area of $^1O_2$ within its lifetime was considered. Time-resolved

phosphorescence measurement is the most direct method to study formation and decay of intracellular $^1O_2$.[1,10] Although the reported lifetime of $^1O_2$ varies depending on the experimental conditions (a few tens of nanoseconds to 3 μs),[2,7,9] the longest travel distance of intracellular $^1O_2$ has been reported to be ~268 nm over a period t of twice its lifetime.[7] Furthermore, a diameter of mitochondria fibril is ~200−400 nm,[40] and both Si-DMA and accumulated PpIX are considered to be located inside the mitochondrial inner membrane.[39,46] Such a complete colocalization within a diffusible area of $^1O_2$ is regarded as the main reason for a highly localization-selective response of Si-DMA. On the other hand, $^1O_2$ diffusion across different intracellular organelles is theoretically impossible as proven by imaging of Si-DMA fluorescence (Figure 5-9b).

In the case of KillerRed, the inefficient $^1O_2$ generation of KillerRed is proven by its photocytotoxicity that is rather higher in $H_2O$ than in $D_2O$[59] and silence at 1270 nm upon photoirradiaiton where $^1O_2$ phosphorescence can be observed.[57] Instead, hydrogen peroxide and a superoxide anion can form $^1O_2$ as a byproduct of the Haber−Weiss reaction (i.e. $H_2O_2 + O_2^{\bullet-} \rightarrow {}^1O_2 + {}^{\bullet}OH + {}^{-}OH$). Vegh et al., however, reported that KillerRed exhibits the quantum yield of hydrogen peroxide generation less than 1% because the generated superoxide anion is quenched inside of the protein by amino acid residues.[57] In fact, even if the superoxide anion is largely generated in a living cell, various enzymatic systems such as superoxide dismutase will quench superoxide to $^3O_2$.[5,6] In accordance with this result, the fluorescence increase of Si-DMA was not monitored under excessive ROS generation in mitochondria induced by an oxidative burst in RAW 264.7 macrophage (Figure 5-11c; the detailed discussion can be found in Supporting Information). This finding further supports that Si-DMA maintains its selectivity to $^1O_2$ in a living cell, while it does not respond to the trace amount of intracellular $^1O_2$.

**Potential Usages of Si-DMA.** To conclude, other potential usages of Si-DMA are proposed in addition to visualization of mitochondrial $^1O_2$ during PDT. Using a newly designed far-red fluorescence probe, Si-DMA, the author succeeded in increasing the spatial resolution of $^1O_2$ detection up to a single mitochondrial tubule (Figure 5-9a). This fluorescence increase was never monitored in the case of TMPyP4 that resides in lysosomes, nucleus, and cytoplasm. Considering the localization-dependent response, it was first suggested that Si-DMA can be used as mitochondrial markers of Sens to confirm its accurate internalization. As mentioned above, mitochondria is the main target organelle in the PDT study because dysfunction of mitochondria

exerts the strongest cytotoxicity.[41–43] Practically, an infinitesimal addition of Si-DMA to the culture media can quickly stain mitochondria (cf. [Si-DMA] = 20 nM and 30 min incubation was enough to stain). So far, R123 and other cationic dyes have been used to visualize changes in the mitochondrial structure and to confirm localization of a particular substance in mitochondria. In addition to both usages, Si-DMA can further provide information about whether the mitochondria-targeted type-II Sens works properly in terms of $^1O_2$ generation.

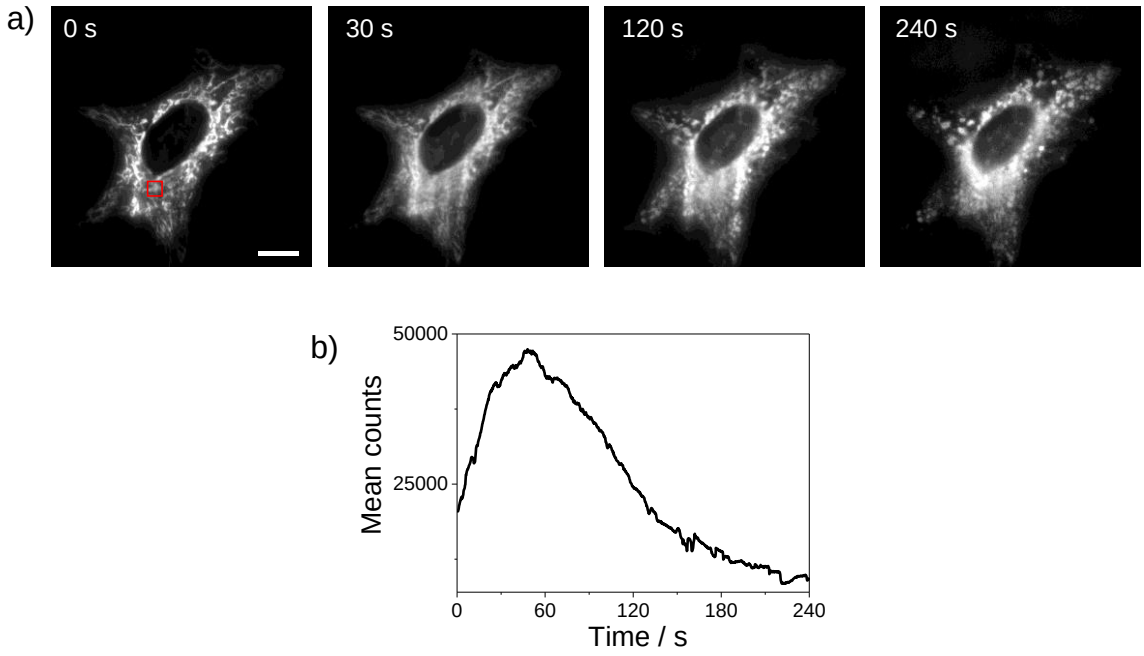


**Figure 5-12. (a)** Si-DMA fluorescence change upon 640-nm irradiation (0.6 W cm$^{-2}$) of 5-ALA-derived PpIX and **(b)** mean counts change of ROI (red box in 0-s image). Intensities of each image have been adjusted to obtain a clear picture. [Si-DMA] = 100 nM and Scale bar: 10 μm.

Second, Si-DMA can be presumably used to indicate PDT dose and cell viability. Upon prolonged photoirradiation at 640 nm (2−4 min), fragmentation of the mitochondrial structure and cell shrinkage accompanied by dimmer fluorescence of Si-DMA were observed (Figure 5-12). Simultaneously, vacuole formation and granular appearance of cell structures were monitored (data are not shown here but are identical to Figure 1 of ref 48). Moreover, fluorescence of Si-DMA upon photoirradiation rarely increased in dying or dead cells. This is considered to be due to (1) defocusing caused by cell morphology change, (2) leak of Si-DMA

upon a loss of mitochondrial membrane potential,[48] and (3) increase in overall intracellular viscosity, making a collision between $^1O_2$ and Si-DMA difficult.[60] In this sense, slight fluorescence decrease of Si-DMA shown in Figure 5-9b (Sens: TMPyP4) is not caused by $^1O_2$-derived photo-oxidation but rather by intracellular environmental change as described above. With further systematic and quantitative studies on the correlation among the fluorescence change of Si-DMA, PDT dose, and cell death pathways (e.g., apoptosis and necrosis), Si-DMA will possibly work as a barometer to report acute cytotoxicity and cell viability during PDT.

## Conclusion

In this study, the author proposed a new and promising far-red fluorescent probe, Si-DMA, for the intracellular $^1O_2$ detection. As a dyad of Si-rhodamine and DMA, Si-DMA is present as a monomer and H-aggregates in organic solvents and neutral buffered solutions, respectively, while both of the states can react with $^1O_2$. A cationic charge and adequate lipophilicity of Si-DMA facilitate the selective mitochondrial localization. In the cell experiment, fluorescence of Si-DMA increases only by photoirradiation of colocalized and type-II Sens, PpIX. On the other hand, type-II Sens with non-mitochondrial localizations, mitochondria-targeted KillerRed, and an oxidative burst of the macrophage fails to change Si-DMA fluorescence. This result confirms a short diffusion distance of $^1O_2$ (~ 400 nm) and substantial generation of $^1O_2$ by type-II Sens ($\Phi_\Delta$ of PpIX = 0.54). This was so far the first example of a $^1O_2$ fluorescence probe to suggest a clear image of $^1O_2$ formation during PDT at the subcellular level. To conclude, the author would like to emphasize the potential of Si-rhodamine derivatives to be exploited in the single-molecule imaging of intracellular $^1O_2$ during PDT. Unfortunately Si-DMA exhibits a limitation in this application because of its dim fluorescence before reacting to $^1O_2$. Prospective candidates of the new $^1O_2$ probe are required to exhibit a completely dark initial state, enough brightness (extinction coefficient >50000 $M^{-1}$ $cm^{-1}$; $\Phi_{fl} > 0.1$),[61] good cell permeability, and water solubility.

## References

(1) Ogilby, P. R. *Chem. Soc. Rev.* **2010**, *39*, 3181.
(2) *Advances in Photodynamic Therapy: Basic, Translational, and Clinical*; Hamblin, M. R., Mróz, P., Eds.; Artech House Engineering in Medicine & Biology Series; Artech House: Boston,

2008.
(3) Castano, A. P.; Mroz, P.; Hamblin, M. R. *Nat. Rev. Cancer* **2006**, *6*, 535.
(4) Kanofsky, J. R. *Chem.−Biol. Interact.* **1989**, *70*, 1.
(5) Winterbourn, C. C. *Nat. Chem. Biol*. **2008**, *4*, 278.
(6) Dixon, S. J.; Stockwell, B. R. *Nat. Chem. Biol.* **2014**, *10*, 9.
(7) Jarvi, M. T.; Niedre, M. J.; Patterson, M. S.; Wilson, B. C. *Photochem. Photobiol.* **2006**, *82*, 1198.
(8) Kanofsky, J. R.; Hoogland, H.; Wever, R.; Weiss, S. J. *J. Biol. Chem.* **1988**, *263*, 9692.
(9) Skovsen, E.; Snyder, J. W.; Lambert, J. D. C.; Ogilby, P. R. *J. Phys. Chem. B* **2005**, *109*, 8570.
(10) Celli, J. P.; Spring, B. Q.; Rizvi, I.; Evans, C. L.; Samkoe, K. S.; Verma, S.; Pogue, B. W.; Hasan, T. *Chem. Rev.* **2010**, *110*, 2795.
(11) Snyder, J. W.; Skovsen, E.; Lambert, J. D. C.; Poulsen, L.; Ogilby, P. R. *Phys. Chem. Chem. Phys.* **2006**, *8*, 4280.
(12) Tanaka, K.; Miura, T.; Umezawa, N.; Urano, Y.; Kikuchi, K.; Higuchi, T.; Nagano, T. *J. Am. Chem. Soc.* **2001**, *123*, 2530.
(13) Liu, Y.-J.; Wang, K.-Z. *Eur. J. Inorg. Chem.* **2008**, *2008*, 5214.
(14) Ruiz-González, R.; Zanocco, R.; Gidi, Y.; Zanocco, A. L.; Nonell, S.; Lemp, E. *Photochem. Photobiol.* **2013**, *89*, 1427.
(15) Pedersen, S. K.; Holmehave, J.; Blaikie, F. H.; Gollmer, A.; Breitenbach, T.; Jensen, H. H.; Ogilby, P. R. *J. Org. Chem.* **2014**, *79*, 3079.
(16) Song, B.; Wang, G.; Tan, M.; Yuan, J. *J. Am. Chem. Soc.* **2006**, *128*, 13442.
(17) Dai, Z.; Tian, L.; Xiao, Y.; Ye, Z.; Zhang, R.; Yuan, J. *J. Mater. Chem. B* **2013**, *1*, 924.
(18) Xu, K.; Wang, L.; Qiang, M.; Wang, L.; Li, P.; Tang, B. *Chem. Commun.* **2011**, *47*, 7386.
(19) Song, D.; Cho, S.; Han, Y.; You, Y.; Nam, W. *Org. Lett.* **2013**, *15*, 3582.
(20) Oliveira, M. S.; Severino, D.; Prado, F. M.; Angeli, J. P. F.; Motta, F. D.; Baptista, M. S.; Medeiros, M. H. G.; Di Mascio, P. *Photochem. Photobiol. Sci.* **2011**, *10*, 1546.
(21) Gollmer, A.; Arnbjerg, J.; Blaikie, F.; Pedersen, B.; Breitenbach, T.; Daasbjerg, K.; Glasius, M.; Ogilby, P. *Photochem. Photobiol.* **2011**, *87*, 671.
(22) Kim, S.; Fujitsuka, M.; Majima, T. *J. Phys. Chem. B* **2013**, *117*, 13985.
(23) Koide, Y.; Urano, Y.; Hanaoka, K.; Terai, T.; Nagano, T. *ACS Chem. Biol.* **2011**, *6*, 600.
(24) Koide, Y.; Urano, Y.; Hanaoka, K.; Piao, W.; Kusakabe, M.; Saito, N.; Terai, T.; Okabe, T.; Nagano, T. *J. Am. Chem. Soc.* **2012**, *134*, 5029.
(25) Egawa, T.; Hanaoka, K.; Koide, Y.; Ujita, S.; Takahashi, N.; Ikegaya, Y.; Matsuki, N.; Terai, T.; Ueno, T.; Komatsu, T.; Nagano, T. *J. Am. Chem. Soc.* **2011**, *133*, 14157.
(26) Piao, W.; Tsuda, S.; Tanaka, Y.; Maeda, S.; Liu, F.; Takahashi, S.; Kushida, Y.; Komatsu, T.; Ueno, T.; Terai, T.; Nakazawa, T.; Uchiyama, M.; Morokuma, K.; Nagano, T.; Hanaoka, K. *Angew. Chem., Int. Ed.* **2013**, *52*, 13028.
(27) Lukinavičius, G.; Umezawa, K.; Olivier, N.; Honigmann, A.; Yang, G.; Plass, T.; Mueller, V.; Reymond, L.; Corrêa, I. R.; Luo, Z. G.; Schultz, C.; Lemke, E. A.; Heppenstall, P.; Eggeling, C.; Manley, S.; Johnsson, K. *Nat. Chem.* **2013**, *5*, 132.

(28) Miura, T.; Urano, Y.; Tanaka, K.; Nagano, T.; Ohkubo, K.; Fukuzumi, S. *J. Am. Chem. Soc.* **2003**, *125*, 8666.
(29) Fudickar, W.; Linker, T. *J. Am. Chem. Soc.* **2012**, *134*, 15071.
(30) Martinez, V.; Arbeloa, F.; Prieto, J.; Lopez, T.; Arbeloa, I. *J. Phys. Chem. B* **2004**, *108*, 20030.
(31) Nasr, C.; Liu, D.; Hotchandani, S.; Kamat, P. V. *J. Phys. Chem.* **1996**, *100*, 11054.
(32) McCann, T. E.; Kosaka, N.; Koide, Y.; Mitsunaga, M.; Choyke, P. L.; Nagano, T.; Urano, Y.; Kobayashi, H. *Bioconjugate Chem.* **2011**, *22*, 2531.
(33) Ragas, X.; Jimenez-Banzo, A.; Sanchez-Garcia, D.; Batllori, X.; Nonell, S. *Chem. Commun.* **2009**, 2920.
(34) Redmond, R. W.; Gamlin, J. N. *Photochem. Photobiol.* **1999**, *70*, 391.
(35) Johnson, L. V.; Walsh, M. L.; Chen, L. B. *Proc. Natl. Acad. Sci. U.S.A.* **1980**, *77*, 990.
(36) Galluzzi, L.; Zamzami, N.; de la Motte Rouge, T.; Lemaire, C.; Brenner, C.; Kroemer, G. *Apoptosis* **2007**, *12*, 803.
(37) Smiley, S. T.; Reers, M.; Mottola-Hartshorn, C.; Lin, M.; Chen, A.; Smith, T. W.; Steele, G. D.; Chen, L. B. *Proc. Natl. Acad. Sci. U.S.A.* **1991**, *88*, 3671.
(38) Salvioli, S.; Ardizzoni, A.; Franceschi, C.; Cossarizza, A. *FEBS Lett.* **1997**, *411*, 77.
(39) Skulachev, V. P. *Trends Biochem. Sci.* **2001**, *26*, 23.
(40) Schmidt, R.; Wurm, C. A.; Punge, A.; Egner, A.; Jakobs, S.; Hell, S. W. *Nano Lett.* **2009**, *9*, 2508.
(41) Kroemer, G.; Dallaporta, B.; Resche-Rigon, M. *Annu. Rev. Physiol.* **1998**, *60*, 619.
(42) Steinbach, P.; Wedmgandt, H.; Baumgartner, R.; Kriegmair, M.; Hofstädter, F.; Knüchel, R. *Photochem. Photobiol.* **1995**, *62*, 887.
(43) Castano, A. P.; Demidova, T. N.; Hamblin, M. R. *Photodiagn. Photodyn. Ther.* **2004**, *1*, 279.
(44) Mik, E.; Stap, J.; Sinaasappel, M.; Beek, J.; Aten, J.; van Leeuwen, T.; Ince, C. *Nat. Methods* **2006**, *3*, 939.
(45) Atif, M.; Firdous, S.; Khurshid, A.; Noreen, L.; Zaidi, S. S. Z.; Ikram, M. *Laser Phys. Lett.* **2009**, *6*, 886.
(46) Peng, Q.; Berg, K.; Moan, J.; Kongshaug, M.; Nesland, J. M. *Photochem. Photobiol.* **1997**, *65*, 235.
(47) Gaullier, J.-M.; Gèze, M.; Santus, R.; Melo, T. S. E.; Mazière, J.-C.; Bazin, M.; Morlière, P.; Dubertret, L. *Photochem. Photobiol.* **1995**, *62*, 114.
(48) Gollmer, A.; Besostri, F.; Breitenbach, T.; Ogilby, P. R. *Free Radical Res.* **2013**, *47*, 718.
(49) Shieh, Y.-A.; Yang, S.-J.; Wei, M.-F.; Shieh, M.-J. *ACS Nano* **2010**, *4*, 1433.
(50) Yuan, Q.; Wu, Y.; Wang, J.; Lu, D.; Zhao, Z.; Liu, T.; Zhang, X.; Tan, W. *Angew. Chem., Int. Ed.* **2013**, *52*, 13965.
(51) Yin, M.; Li, Z.; Liu, Z.; Ren, J.; Yang, X.; Qu, X. *Chem. Commun.* **2012**, *48*, 6556.
(52) da Silva, E. F. F.; Pedersen, B. W.; Breitenbach, T.; Toftegaard, R.; Kuimova, M. K.; Arnaut, L. G.; Ogilby, P. R. *J. Phys. Chem. B* **2011**, *116*, 445.
(53) Kalyanasundaram, K. *Inorg. Chem.* **1984**, *23*, 2453.

(54) Bulina, M. E.; Lukyanov, K. A.; Britanova, O. V.; Onichtchouk, D.; Lukyanov, S.; Chudakov, D. M. *Nat. Protoc.* **2006**, *1*, 947.
(55) Carpentier, P.; Violot, S.; Blanchoin, L.; Bourgeois, D. *FEBS Lett.* **2009**, *583*, 2839.
(56) Pletnev, S.; Gurskaya, N. G.; Pletneva, N. V.; Lukyanov, K. A.; Chudakov, D. M.; Martynov, V. I.; Popov, V. O.; Kovalchuk, M. V.; Wlodawer, A.; Dauter, Z.; Pletnev, V. *J. Biol. Chem.* **2009**, *284*, 32028.
(57) Vegh, R. B.; Solntsev, K. M.; Kuimova, M. K.; Cho, S.; Liang, Y.; Loo, B. L. W.; Tolbert, L. M.; Bommarius, A. S. *Chem. Commun.* **2011**, *47*, 4887.
(58) Finikova, O. S.; Lebedev, A. Y.; Aprelev, A.; Troxler, T.; Gao, F.; Garnacho, C.; Muro, S.; Hochstrasser, R. M.; Vinogradov, S. A. *ChemPhysChem* **2008**, *9*, 1673.
(59) Serebrovskaya, E. O.; Edelweiss, E. F.; Stremovskiy, O. A.; Lukyanov, K. A.; Chudakov, D. M.; Deyev, S. M. *Proc. Natl. Acad. Sci. U.S.A.* **2009**, *106*, 9221.
(60) Kuimova, M.; Botchway, S.; Parker, A.; Balaz, M.; Collins, H.; Anderson, H.; Suhling, K.; Ogilby, P. *Nat. Chem.* **2009**, *1*, 69.
(61) Roy, R.; Hohng, S.; Ha, T. *Nat. Methods* **2008**, *5*, 507.

**Supporting Figure.** Synthesis of Si-DMA

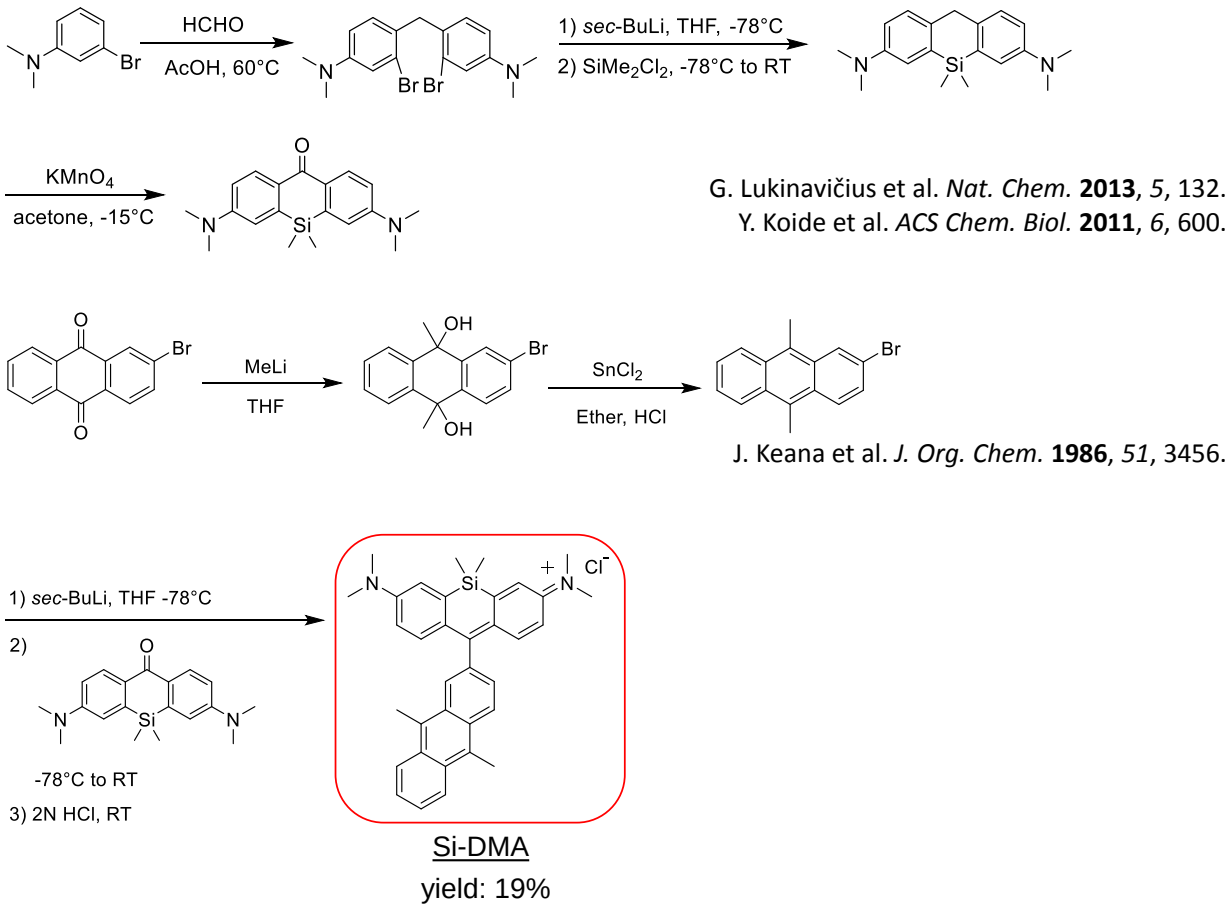

# General Conclusion

Throughout this thesis, the potential and versatility of fluorescence detection of biological phenomena ex vitro and in vitro have been thoroughly examined.

In Chapter 1, the conformational heterogeneities of i-motif DNA have been investigated using single-molecule fluorescence spectroscopy. The presence of a partially-folded form of the C-rich 21-mer infers a possibility of the formation of i-motif tetraplex at the physiological pH under the molecular crowding condition.

In Chapter 2, the conformational heterogeneities of A-motif DNA have been investigated using single-molecule fluorescence spectroscopy. A finding of the shrunken form of A-rich DNA tentatively indicates the existence of the intramolecular duplex region in poly(A) tail in vivo. Those non-B forms of DNA can influence cellular metabolism and pathological progress in living matter.

In Chapter 3, photochemistry of SOSG, a dyad of fluorescein and anthracene derivatives and a commercialized fluorescence probe for $^1O_2$ detection, has been carefully scrutinized using various time-resolved spectroscopic techniques. Upon 355-nm excitation, one-electron oxidized fluorescein of SOSG generated via two-photon photoionization, which is responsible for the irreversible photobleaching. Meanwhile, the excitation at 532 nm resulted in the formation of $^3$Fl* that subsequently generates $^1O_2$ ($\Phi_\Delta < 0.06$) and endoperoxidized SOSG, which is fluorescent. Obtained results in this study make a caution to choose fluorescein as a fluorescence probe concerning $^1O_2$ generation and photodecomposition under the prolonged photoirradiation.

In Chapter 4, a dyad of Si-rhodamine and 9-phenylanthracene, Si-An, has been synthesized, and its unprecedented aggregation has been characterized using X-ray crystallography and time-resolved spectroscopy. This study finally proposes the substitution of 9-phenylanthracene may induce J-aggregate of other fluorophores, such as fluorescein and rhodamine derivatives, in the presence of adequate counterions. Furthermore, considering changes in absorption spectra and fluorescence increase of Si-An J-aggregate upon $^1O_2$ reaction, a more sophisticated design of a fluorophore and 9-phenylanthracene dyad will suggest a new paradigm of $^1O_2$ detection, for instance, a promising intracellular fluorescence probe with high S/N ratio by complete

fluorescence quenching via intermolecular PET.

In Chapter 5, a dyad of Si-rhodamine and 9,10-dimethylanthracene, Si-DMA, has been synthesized, characterized, and applied to visualize intracellular $^1O_2$ generation during PDT. In the cell experiment, fluorescence of Si-DMA increased only by photoirradiation of the colocalized and type-II Sens, 5-ALA-derived PpIX. On the other hand, type-II Sens with the non-mitochondrial localization, mitochondrial type-I Sens, and an oxidative burst (i.e. drug-induced generation of ROS from the mitochondria) of the macrophage have failed to increase fluorescence of Si-DMA. This result accords with a short diffusion distance of $^1O_2$ (~300 nm) and substantial generation of $^1O_2$ by type-II Sens ($\Phi_\Delta$ of PpIX = 0.54) as compared to type-I Sens protein. This is the first report of a $^1O_2$ fluorescence probe to show a clear image of $^1O_2$ formation during PDT at the subcellular level.

In short, heterogenieties of biological phenomena, non-B DNA conformation and intracellular $^1O_2$ generation, were investigated by single-molecule fluorescence spectroscopy and a rationally designed fluorescence probe, Si-DMA, respectively. For the future design of $^1O_2$ probe, one should aim at visualizing a single event of $^1O_2$ formation, the most direct indicator related to cell-killing mechanisms of PDT. Using Si-DMA, however, single-molecule detection of intracellular $^1O_2$ was not successful since fluorescence quenching of intracellular Si-DMA was insufficient to tell whether the detected signal was from Si-DMA or Si-DMEP. The same problem arised in the case of SOSG. In light of Chapters 1 and 2, therefore, a fluorescence probe based on FRET rather than PET seems to be a promising solution for single-molecule fluorescence detection because (1) FRET is not influenced by environmental factors and (2) measuring intrinsic properties, which are not dependent on the concentration, provides more accurate information than extrinsic properties, such as fluorescence intensity.

To conclude, this thesis clearly indicates that a smart and appropriate design of a fluorescence probe for the specific purpose as well as methodological improvements are required simultaneously to advance currently available temporal and spatial resolutions of fluorescence microscopy techniques. Fluorescence detection in vivo with far improved temporal and ‘single-molecule’ spatial resolutions will ultimately realize the visualization of a single intermolecular interaction inside of a cell that will deepen our understanding of the life.

# List of Publications

1. pH-Induced Intramolecular Folding Dynamics of i-Motif DNA
   Jungkweon Choi, Sooyeon Kim, Takashi Tachikawa, Mamoru Fujitsuka, and Tetsuro Majima.
   *J. Am. Soc. Chem.* **2011**, *133*(40), 16146-16153.

2 Self-Assembly of Polydeoxyadenylic Acid Studied at the Single-Molecule Level
   Sooyeon Kim, Jungkweon Choi, and Tetsuro Majima.
   *J. Phys. Chem. B* **2011**, *115*(51), 15399-15405.

3. Photochemistry of Singlet Oxygen Sensor Green
   Sooyeon Kim, Mamoru Fujitsuka, and Tetsuro Majima.
   *J. Phys. Chem. B* **2013**, *117*(45), 13985-13992.

4. Far-red Fluorescence Probe for Monitoring Singlet Oxygen during Photodynamic Therapy
   Sooyeon Kim, Takashi Tachikawa, Mamoru Fujitsuka, and Tetsuro Majima.
   *J. Am. Chem. Soc.* **2014**, *136*(33), 11707–11715.

5. Unprecedented J-Aggregate Formation of Si-Rhodamine and Phenylanthracene Dyad Studied by Crystal Structural Analysis and Transient Absorption Measurements
   Sooyeon Kim, Mamoru Fujitsuka, Norimitsu Tohnai, Takashi Tachikawa, Ichiro Hisaki, Mikiji Miyata, and Tetsuro Majima.
   *Submitted.*

**Other publication**

1. Unfolding Dynamics of Cytochrome *c* Revealed by Single-Molecule and Ensemble-Averaged Spectroscopy
   Jungkweon Choi, Sooyeon Kim, Takashi Tachikawa, Mamoru Fujitsuka, and Tetsuro Majima.
   *Phys. Chem. Chem. Phys.* **2011**, *13*(13), 5651-5658.

**Review**

1. Developing a New Fluorescence Probe of Singlet Oxygen during Photodynamic Therapy
   Sooyeon Kim, Mamoru Fujitsuka, and Tetsuro Majima.
   *EPA News Lett.* **2014**, *86*(3) in press.

# Acknowledgements

The author wishes to express her sincerest gratitude to Professor Tetsuro Majima, the Institute of Science and Industrial Research (SANKEN), Osaka University, for his thoughtful supervision, guidance, and advice throughout the doctoral course.

The author appreciates Associate Professor Mamoru Fujitsuka, Assistant Professor Takashi Tachikawa (currently, Associate Professor in Kobe University), Specially Appointed Professor Akira Sugimoto, Specially Appointed Assistant Professor Jungkweon Choi (currently, Reseach Fellow in Institute for Basic Science, Daejeon, Korea), and Specially Appointed Professor Mikiji Miyata for their helpful advices, discussions, and guidance of research activities throughout the doctoral course. The author is also indebted to Associate Professor Kiyohiko Kawai, Assistant Professor Yasuko Osakada, and Assistant Professor Sachiko Tojo for their kind helps and advice.

The author is also deeply grateful to Professor Yoshihisa Inoue and Professor Shuhei Seki for their fruitful comments on this dissertation.

The author would like to thank collaborators and advisers during this research: Professor W. E. Moerner in Stanford University, Associate Professor Norimitsu Tohnai and Assistant Professor Ichiro Hisaki in Graduate School of Engineering, Osaka University, Professor Taroh Kinoshita and Associate Professor Yasuke Maeda in BIKEN, Osaka University, and Associate Professor Tsuyoshi Nishi in SANKEN, Osaka University. Furthermore, the author appreciates Professor Sung Sik Kim in Chonbuk National University, Professor Seog K. Kim in Yeungnam University, and Research Professor Dae Won Cho in Korea University for warm-hearted encouragements, and Professor Jong-Man Kim and Associate Professor Ho Bum Park in Hanyang University who provided me the initial motivation towards research and kind advice from the undergraduate time.

The author also hopes to thank for all the members of Professor Majima's research group, including Dr. Zhenfeng Bian, Dr. Jun Rye Choi, Dr. Man Jae Park, Dr. Shi-Cong Cui, Dr. Nan Wang, Dr. Lingli Cheng, Dr. Zhaoke Zheng, Dr. Wooyul Kim, Mr. Peng Zhang, Mr. Shih-Hsun Lin, Mr. Chao Lu, Mr. Atsushi Tanaka, Mr. Ossama Elbanna, Mr. Peerathat Pinpithak, Mr. Soichiro Yamashita, Mrs. Eri Matsutani, Mr. Mitsuo Hayashi, Mr. Tomoyuki Yonezawa, Miss

Mayuka Ishikawa, Mr. Tatsuya Ohsaka, Mr. Takeshi Koshimo, Mr. Yui Tei, Mr. Jongjin Park, Mr. Shunsuke Ano, Mr. Kenshi Nakao, Miss Ayaka Kuroda, Mr. Kota Nomura, Mr. Yang Zhou, and Miss Sanae Tominaga. The author makes special acknowledgements to Jieun Jung, Dr. Jiyun Park, Hyunhee Shim, and Dr. Jihyoun Seong, who have encouraged me with their warm-hearted helps from research discussions to daily lives in Japan.

The author acknowledges financial supports from Japan Tabacco Asian Scholarship Program and Research Fellowship for Young Scientists Program of Japan Society for the Promotion of Science during the doctoral course.

Finally, the author is truly grateful to her family, Jeomsik Kim, Jinjam Choi, and Dongchan Kim, for their endless supports, encouragements and love.

Sooyeon Kim

2015